IMPROVEMENT OF SEISMIC BEHAVIOR OF SOFT CLAY FOUNDATIONS UNDER EMBANKMENTS BY GEOSYNTHETIC ENCASED COLUMNS: AN EXPERIMENTAL AND NUMERICAL APPROACH

by

Cihan Cengiz

B.S., Civil Engineering, Koceli University, 2009

M.S. Civil Engineering, Boğaziçi University, 2012

Submitted to the Institute for Graduate Studies in
Science and Engineering in partial fulfillment of
the requirements for the degree of
Doctor of Philosophy

Graduate Program in Civil Engineering

Boğaziçi University

2018

IMPROVEMENT OF SEISMIC BEHAVIOR OF SOFT CLAY FOUNDATIONS UNDER EMBANKMENTS BY GEOSYNTHETIC ENCASED COLUMNS: AN EXPERIMENTAL AND NUMERICAL APPROACH

APPROVED BY:

Prof. Erol Güler (Thesis Supervisor)	.....
Assoc. Prof. İsmail Hakkı Aksoy	.....
Assoc. Prof. Özer Çinicioğlu	.....
Prof. Feyza Çinicioğlu	.....
Prof. Hilmi Luş	.....

DATE OF APPROVAL: 15.01.2018

ACKNOWLEDGEMENTS

At times, it was impossible to move forward with this dissertation work. "Obstacles" made it painfully hard to conduct the studies. I am also glad that obstacles in many forms presented themselves. Through hardships, I have realized my own will to do what I love which is research, to learn, and to become a better engineer and scholar. First and foremost I would like to thank my mom. She inspires me with her everlasting fortitude and strength and I am glad to be her son. Her constant support and love made me and everything I achieved or will achieve possible. Secondly I would like to thank my soul mate, Jana Stolarikova Cengiz. I do owe her an apology for not naming her openly in my master's thesis.

I would like to thank İ. Emrah Kılıç who is a brother from another mother. I would also like to thank Anıl Yıldız, although we had to be separated during our studies, we were together in our hearts. A. Ufuk Şahin has constantly supported me and guided me, I cannot thank him enough.

Prof. Hilmi Luş has also been an immensely important academic figure in my studies. He has mentored me and patiently answered my questions. With his support and the classes he thought I believe I am more of a complete Geotechnical Engineer.

Lastly, and most importantly, I wish to express my heart felt gratitude to my supervisor, Prof. Erol Güler. The best way I can define how I feel and think about the contributions of my thesis supervisor to me as a person and an engineer is by calling him my academic father. This study would not have been possible without his constant support, expert guidance, and everlasting patience. It is my ambition to become more like him as I learn and grow as an engineer and as a person. I should also thank TUBITAK (Grant no: 213M359), HUESKER GmbH, and BAP for their financial support. This thesis is dedicated to Emilia Duru Cengiz, our daughter; I cannot wait to meet her.

ABSTRACT

IMPROVEMENT OF SEISMIC BEHAVIOR OF SOFT CLAY FOUNDATIONS UNDER EMBANKMENTS BY GEOSYNTHETIC ENCASED COLUMNS: AN EXPERIMENTAL AND NUMERICAL APPROACH

This study is concerned with understanding the behavior and performance of ordinary and geosynthetic encased stone columns embedded in soft soils that are subjected to dynamic loads. There are almost no studies in the currently available literature on the dynamic load bearing characteristics of ordinary and geosynthetic encased columns. The study also aims to shed light into the prospect of supporting embankments founded on soft soils with geosynthetic encased columns. Growing demand of infrastructure embankments in soft soils that are located in areas of high seismicity potential necessitates such a study to be conducted. Within the scope of this study large scale test setups have been designed, developed, manufactured and experimented with. A rigid box and a novel large scale laminar box assembly is utilized for 1-g shaking table experiments. While the rigid box assembly is intended to be physical analogy of a group of geosynthetic encased columns that are laterally restrained with bridge abutments, retaining walls, and sheet piles; the laminar box is an analogy for the columns which are subjected to free-field conditions. The response and performance of the individual column and the column enhanced soft soil body are investigated. Major findings in the behavior of geosynthetic encased columns have been made with this dissertation study. A correlation between the Arias Intensity and dynamic reinforcement strain is observed. The beneficial effects of geosynthetic encased column inclusion have also been noted. The shear modulus of the soft soil is increased by almost an order of magnitude with an area replacement ratio of about 7%.

ÖZET

GEOSENTETİK DONATILI TAŞ KOLONLAR İLE YUMUŞAK TEMEL ÜZERİNE İNŞA EDİLEN TOPRAK SEDDELERİN SİSMİK DAVRANIŞININ İYİLEŞTİRİLMESİ İLE İLGİLİ DENEYSEL VE NÜMERİK BİR ÇALIŞMA

Bu çalışmanın amacı, yumuşak zeminlere uygulanmış olan donatısız ve geosentetik donatılı taş kolonların dinamik yükler altındaki performas ve davranışının belirlenmesidir. Literatürde taş kolonların ve geosentetik donatılı taş kolonların dinamik yükler etkisi altındaki taşıma güçlerine ilişkin çalışma bulunmamaktadır. Yapılan doktora çalışması, tekil kolonların davranışı ve performansını araştırmanın yanı sıra kolonlarla desteklenecek olan altyapı seddelerinin deprem yüklerine karşı fizibiletisini araştırır. Alt yapı projelerine olan talepteki artış, projenin alanının elverişli zemin koşullarında olmasını zorlaştırmıştır. Saha koşullarının yumuşak ve taşıma kapasitesinin düşük zeminlerden oluştuğu durumlarda ve sismik riskin yüksek olduğu bölgelerde, seddeyi kolonlarla taşıtmak olası bir mühendislik çözümüdür. Bu çalışma kapsamında bahsedilen saha durumlarını ve deprem etkilerini araştırmak için iki adet büyük boylu deney düzeneği hazırlanmıştır. Deney düzenekleri proje ekibi tarafından tasarlanmış, geliştirilmiş, ürettirilmiş ve deneylerde kullanılmıştır. 1-g sarma masası deneyleri için bir adet rijit kutu ve bir adet de laminer kutu kullanılmıştır. Rijit kutu deneyleri ile saha koşullarında köprü ayağı, istinat duvarı ve palplaj perdesi gibi elemanlarca yanal olarak kısıtlanmış olan kolonların davranışı modellenmiştir. Laminer kutu deneyleri ise serbest saha koşullarına maruz kalan kolonlar modellenmiştir.

TABLE OF CONTENTS

ACKNOWLEDGEMENTS iii
ABSTRACT iv
ÖZET v
LIST OF FIGURES viii
LIST OF TABLES xvii
LIST OF SYMBOLS xix
LIST OF ACRONYMS/ABBREVIATIONS xx
1. INTRODUCTION 1
1.1. Background and Motivation 1
1.2. Research Objectives 5
1.3. Dissertation Organization 5
2. LITERATURE REVIEW 7
2.1. Literature on Geosynthetic Encased Columns and Ordinary Stone Columns 7
2.1.1. Design Methods for Encased Stone Columns 16
2.1.2. Engineering Behavior of Ordinary and Encased Stone Columns . 22
2.2. Literature on Large Scale Dynamic Testing 28
3. MATERIALS 33
3.1. Clay 33
3.2. Sand and Gravel 35
3.3. Geosynthetic Reinforcements 36
3.3.1. General Properties 36
3.3.2. Calibration of Strain Measurements 37
4. EXPERIMENTAL METHODOLOGY 39
4.1. Rigid Box 39
4.1.1. Properties of the Rigid Box 39
4.1.2. Sample Preparation Technique for the Rigid Box 40
4.2. Laminar Box 43
4.2.1. Properties of the Laminar Box 44
4.2.2. Sensor Placement on the Laminar Box 49

4.3. Sample Preparation Technique for the Laminar Box 51
4.3.1. Clay Slurry Preparation, Placement, and Consolidation 51
4.3.2. Column Installation 52
4.4. Calibration and Implementation of the Sensors and the Data Logger System 54
4.4.1. Calibration and Implementation of Strain Rosettes 54
4.4.2. Sensor Calibration and Data Logger System 61
5. SHAKING TABLE TESTING PROGRAM 65
5.1. Rigid Box Experiments 65
5.2. Laminar Box Experiments 68
6. RIGID BOX RESULTS 74
6.1. Settlement of the Unit Cells under Seismic Loading 75
6.2. Strains Occurring on Geosynthetic Encasements during Seismic Loading 80
6.3. Interplay between Arias Intensity and Seismic Reinforcement Strains of Type A and B 87
6.4. Ramifications for Prototype Columns 92
6.5. Vertical Load Tests on Columns 93
6.5.1. Conclusions 102
6.5.2. Discussion 103
7. LAMINAR BOX RESULTS 105
7.1. Displacement of the Soil Profile 106
7.2. Reinforcement Strains 117
7.3. Soil Amplification 126
7.4. Shear Modulus and Damping Ratio of the Models 132
7.5. Vertical Load Capacities of Columns 139
7.6. Conclusions 140
8. CONCLUSIONS AND RECOMMENDATIONS FOR FUTURE STUDIES . 144
REFERENCES 146

LIST OF FIGURES

Figure 1.1. (a) A typical cross-section depicting the use of GECs, (b) pressure distribution in a Unit Cell. 2

Figure 2.1. Limiting axial capacity curves proposed by Ambily and Gandhi (2007). 16

Figure 2.2. The calculation model "geotextile coated sand column" (Raithel and Kempfert, 2000). 17

Figure 2.3. Cross-section of the GEC subjected to lateral internal pressure. . . 19

Figure 2.4. Failure modes of GECs as defined by Mohapatra *et al.*, (2016). . . 25

Figure 2.5. Columns failed in bending (Chen *et al.*, 2015). 26

Figure 3.1. Unconfined compressive strengths of clay specimens for various consolidation pressures. 34

Figure 3.2. Variation of unconfined compressive strength by the water content of the clay sample. 35

Figure 3.3. Grain size distribution curves pertaining to granular material used. 36

Figure 4.1. The rigid box assembly used by Kilic (2014). 40

Figure 4.2. a) Top view of the pneumatic pistons, b) surcharge plates and their connection to piston rods, c) surcharge plates from bottom. 40

Figure 4.3. a) Clay slurry infill from the drum, b) Top view of clay slurry infill process, c) consolidated clay bed. 41

Figure 4.4. Casing pipe driving unit. 42

Figure 4.5. Instrumentation and see-through image of the rigid box assembly. 43

Figure 4.6. Tension cables used by Bethapudi (2008) to prevent toppling of the laminar box. 45

Figure 4.7. General features of the laminar box. 46

Figure 4.8. Two of the surcharge plates. 47

Figure 4.9. The surcharge unit suspended in the air. 48

Figure 4.10. Components of the casing pipe driving unit. 48

Figure 4.11. Laser displacement sensors and accelerometers attached on the laminar box. 50

Figure 4.12. Disposition of sensors in a test where GECs are tested. 50

Figure 4.13. Photograph depicting the inside of the driven casing pipe illumined with a suspended torch. 53

Figure 4.14. Strain gauge calibration test setups for the geotextiles used. 55

Figure 4.15. Transfer function for the vertical component of GT1. 57

Figure 4.16. Strain values of GT1, transfer function applied. 57

Figure 4.17. Measured strain values and fitted actual strain line for GT2. . . . 58

Figure 4.18. Transfer function for the vertical component of GT3. 58

Figure 4.19. Response of strain gauges in all directions for GT3. 59

Figure 4.20. Attached Strain Gauges to GT1. 60

Figure 4.21. Instrumented reinforcements made up of GT2 and GT3. 61

Figure 4.22. Soil pressure gauge calibration setup. 62

Figure 4.23. Load cell and pneumatic piston calibration setup. 63

Figure 5.1. 100% amplitude El-Centro accelerogram. 66

Figure 5.2. 100% Amplitude Kobe accelerogram. 67

Figure 5.3. Sine sweep signal. 71

Figure 5.4. Acceleration time history for 0.5 Hz load case. 71

Figure 5.5. Acceleration time history for 2 Hz load case. 72

Figure 5.6. Acceleration time history for 5 Hz load case. 72

Figure 5.7. Gaussian White Noise signal's acceleration time history plot. . . . 73

Figure 6.1. Rigid box assembly mounted on the shaking table. 75

Figure 6.2. (a) Settlement response of the unit cells subjected to 100% Kobe accelerogram and (b) significant duration window of the accelerogram shown on a Husid plot. 77

Figure 6.3. Cumulative settlement plots for Setup 1. 78

Figure 6.4. Cumulative settlement plots for Setup 2. 79

Figure 6.5. Cumulative settlement plots for Setup 3. 79

Figure 6.6. Type A, B, and C strains occurring on GEC-2-g^3 during 100% Kobe excitation. 81

Figure 6.7. Strain response of the GT2 material that encased GEC-2-s^3 at a depth of 560 mm. 82

Figure 6.8. Maximum strains measured on GEC-1-g^1 under different excitations. 83

Figure 6.9. Maximum strains measured on GEC-1-g^1 under different excitations. 84

Figure 6.10. Maximum strains measured on GEC-2-s^3. 85

Figure 6.11. Maximum strains measured on GEC-2-g^3. 85

Figure 6.12. Maximum strains measured on GEC-3-g^3. 86

Figure 6.13. a) 100% amplitude El-Centro accelerogram, b) Husid plot for 100% amplitude El-Centro accelerogram, c) strain on GEC-1-s^2 at 280 mm, d) strain versus IA. 88

Figure 6.14. 100% amplitude Kobe accelerogram, b) Husid plot for 100% amplitude Kobe accelerogram, c) strain on GEC-2-s^3 at 880 mm, d) strain versus IA. 89

Figure 6.15. a) Horizontal strain on GEC-2-s^3 at 720 mm throughout seismic excitations, b) cumulative Husid plot for seismic excitations, c) strain versus IA, d) normalized strain and IA in time domain. . . 90

Figure 6.16. Linear approximation for IA and reinforcement strain for GEC-3-g^3 at 1200 mm throughout seismic excitations. 90

Figure 6.17. Maximum and average reinforcement strains in PGA domain. . . . 91

Figure 6.18. Various photographs pertaining to the surcharge loading and laser displacement sensors, and column load test setup. 94

Figure 6.19. Various photographs pertaining to the exhumed columns. 95

Figure 6.20. Horizontal strain response of GEC-2-s^3 during column load tests. . 95

Figure 6.21. Vertical strain response of GEC-2-s^3 during column load tests. . . 96

Figure 6.22. Horizontal strain response of GEC-2-g^3 during column load tests. . 97

Figure 6.23. Vertical strain response of GEC-2-g^3 during column load tests. . . 98

Figure 6.24. Horizontal strain response of GEC-2-g^3 during column load tests. . 98

Figure 6.25. Vertical strain response of GEC-3-g^3 during column load tests. . . 99

Figure 6.26. Maximum lateral strain response of the columns tested in Setup 3 under static vertical loads. 100

Figure 6.27. Settlement vs. time plots for the columns tested in Setup 3. 101

Figure 6.28. Results of stress controlled column tests 102

Figure 7.1. Displacement responses of the laminates under 0.5 Hz load case. . 107

Figure 7.2. The positions of the laminates at the onset of 0.5 Hz load case. . . 107

Figure 7.3. Maximum recorded displacements of the laminates for Sweep-1, 0.5 Hz, and 1 Hz load cases. 109

Figure 7.4. Maximum recorded displacements of the laminates for 1.5, 2, and 3 Hz load cases. 110

Figure 7.5. Maximum recorded displacements of the laminates for 4 Hz, 5 Hz, and Sweep-2 load cases. 110

Figure 7.6. Base drift for the models as a function of the loading frequency. . 111

Figure 7.7. (a) The average and (b) maximum laminate displacements under the action of sinusoidal loads with varying frequencies. 112

Figure 7.8. Peak displacement plots for (a) 25% , (b) 50% , and (c) 100% El-Centro load case. 113

Figure 7.9. Peak displacement plots for (a) 50% and (b) 100% Kobe load case. 114

Figure 7.10. Top laminate displacement values for various PGAs recorded in Earthquake Excitation Scheme. 114

Figure 7.11. Maximum displacement (base drift) of the model soil profiles tested in Earthquake Excitation Scheme. 115

Figure 7.12. Top laminate displacement values for various PGAs recorded in Sinusoidal Excitation Scheme. 116

Figure 7.13. Maximum shear strain values for various PGAs. 117

Figure 7.14. Strain response of the GEC embedded in model 4 during 4 Hz load case, at the elevation of 13th laminate (a) acceleration vs. displacement loops, (b) vertical and horizontal strain plots in time domain. 119

Figure 7.15. Strain response of the GEC embedded in model 4 during 4 Hz load case, at the elevation of 13th laminate (a) displacement vs. strain loops, (b) vertical and horizontal strain plotted against each other. 119

Figure 7.16. Strain response of the GEC-J1000-EQ under 100% El-Centro loading at a depth of 100 mm from column head plane. 120

Figure 7.17. Maximum reinforcement strains in model 3 (a) vertical strains, (b) horizontal strains. 121

Figure 7.18. Maximum reinforcement strains in model 4 (a) vertical strains, (b) horizontal strains. 122

Figure 7.19. Maximum and average tensile strains on reinforcements as a function of (a) load frequency, (b) amplitude. 123

Figure 7.20. Maximum reinforcement strains in model 7 (a) vertical strains, (b) horizontal strains. 124

Figure 7.21. Maximum reinforcement strains in model 8 (a) vertical strains, (b) horizontal strains. 125

Figure 7.22. Maximum and average tensile strains as a function of PGA. 126

Figure 7.23. Plots of amplification values for Sinusoidal Excitation Scheme for 0.5 and 1 Hz. 128

Figure 7.24. Plots of amplification values for Sinusoidal Excitation Scheme for 1.5 and 2 Hz. 128

Figure 7.25. Plots of amplification values for Sinusoidal Excitation Scheme for 3 and 4 Hz. 129

Figure 7.26. Plots of amplification values for Sinusoidal Excitation Scheme for 5 Hz load case. 129

Figure 7.27. Plots of amplification values for Earthquake Excitation Scheme for 25 and 50% El-Centro load case. 130

Figure 7.28. Plots of amplification values for Earthquake Excitation Scheme for 100% El-Centro load case. 130

Figure 7.29. Plots of amplification values for Earthquake Excitation Scheme for 50 and 100% Kobe load case. 131

Figure 7.30. Soil amplification values for the top laminate level (a) Sinusoidal (b) Earthquake Excitation Scheme. 132

Figure 7.31. Acceleration response to pulse loading for (a) OSC-S and (b) GEC-J1000-S. 134

Figure 7.32. Fitted and rough hysteresis loops for the 8^{th} laminate level for (a) OSC-S and (b) GEC-J1000-s during 0.5 Hz load case. 136

Figure 7.33. 10^{th} cycle hysteresis loops for models 1, 2, 3, and 4. 137

Figure 7.34. Hysteresis loops for laminate level 8 for test section 4 (a) at 3 Hz load case, (b) 4 Hz load case. 138

Figure 7.35. Hysteresis loops for OSC-S for (a) 4 and (b) 5 Hz. 138

Figure 7.36. Load-settlement curves for intact and seismically tested columns. . 140

LIST OF TABLES

Table 2.1. Works on GECs and OSCs in the literature. 8

Table 2.2. Details pertaining to studies tabulated in Table 1. 10

Table 2.3. Rigid box assemblies reported in the literature. 29

Table 2.4. Rigid container with absorbing (flexible) boundaries in the literature. 29

Table 2.5. Equivalent shear beam containers reported in the literature. 31

Table 2.6. Summary of laminar box designs in the literature 32

Table 3.1. Chemical composition of the kaolinite clay. 33

Table 3.2. Engineering properties of the sand and the gravel used 36

Table 3.3. Tensile stiffness parameters of the geotextiles used. 37

Table 4.1. List of the sensors used in the experiments. 64

Table 5.1. Experimental program pertaining to Rigid box experiments. 66

Table 5.2. Details of the columns in each Setup tested in Rigid Box experiments. 68

Table 5.3. Detains of the testing program for Sinusoidal Excitation Scheme. . 69

Table 5.4. Detains of the testing program for Earthquake Excitation Scheme. 69

Table 5.5. Details of the models tested with the Laminar Box apparatus. . . . 70

Table 6.1. Cumulative settlement values for the experimental program and calculated settlement reduction factors. 80

Table 6.2. Calculations of additional tensile forces on prototype columns' encasements 93

Table 7.1. Shear modulus in kPa. 136

Table 7.2. Damping ratio calculated from hysteresis loops in%. 139

LIST OF SYMBOLS

a_r	Area replacement ratio
c	Undrained shear strength
E	Modulus of elasticity
K_a	Active earth pressure coefficient
K_o	At rest earth pressure coefficient
K_p	Passive earth pressure coefficient
L	Length of the column
u	Pore water pressure
ε_a	Hoop strain on the geotextile reinforcement
γ	Unit weight of the material
ϕ	Intenral angle of friction
σ	Normal Stress
τ	Shear Stress

LIST OF ACRONYMS/ABBREVIATIONS

GEC	Geosynthetic Encased Column
OSC	Ordinary Stone Column
GT1	Tencate Polyfelt TS 10 geotextile reinforcement
GT2	HUESKER Sefitec PP 50 geotextile reinforcement
GT3	HUESKER Stabilenka 100 geotextile reinforcement
IA	Arias Intensity
PGA	Peak Ground Acceleration

1. INTRODUCTION

1.1. Background and Motivation

In many parts of the world, increasing demand for urbanization necessitates the use of land underlain by soft soils for infrastructure projects. Under such conditions, conventional deep foundations are commonly used to provide support for the superstructure. Although deep foundations such as bored piles have proven their reliability, there are inherent shortcomings associated with conventional deep foundations. These shortcomings include but is not limited to; the cost effectiveness, construction time required, and carbon footprint of the project.

Ground modification techniques are increasingly used instead of conventional deep foundations. Improvement of soft ground conditions with granular columns are probably the one of the most versatile technique among various ground modification alternatives. Once installed, granular columns serve a wide spectrum of important geotechnical functions, namely densification of the soil strata, reinforcement, and drainage of the excess interstitial water. Granular columns are economically viable and environmental impact due to column installation is minimal in comparison to conventional deep foundation methods. One of the significant drawbacks of the granular columns is the load capacity of the granular column.

When ordinary stone or sand columns are installed in soft soils columns typically fail in bulging. The bulging failure occurs due to lack of lateral confinement that is provided by the soft soil. In order to overcome the bulging failure, a tubular geosynthetic reinforcement is used to confine the granular column constituents. The term coined for this type of reinforced granular column is Geosynthetic Encased Column (GEC). The benefits of GECs are: (i) reduction in the absolute and differential settlements, (ii) system is fully loadable immediately after installation, (iii) rapid construction of embankments with large overburden pressures without the risk of bearing failure, (iv) accelerated settlement and excess pore water pressure dissipation, (v) load redistri-

bution among neighboring columns. A sketch of a typical embankment cross-section supported by GECs is given in Figure 1 (a). In Figure 1 (b), the pressure distribution between the soft soil and GEC is illustrated.

The embankment in Figure 1.1(a) is underlain by a weak clay deposit which lacks the necessary bearing capacity characteristics to support the embankment under service loads. The GECs are installed to transfer the vertical loads the firm strata lying beneath the soft clay layer. In Figure 1.1(b), the distribution of the vertical pressures in a Unit Cell is illustrated. In the commonly used German standard, EBGEO (Recommendations for Design and Analysis of Earth Structures Using Geosynthetic Reinforcements; EBGEO, 2011) the unit cell concept is explained as follows: Generally, the deformation forecast based on the axis-symmetrical model of the unit cell (section of an assumed infinite field of columns) may be regarded as adequate to estimate the maximum anticipated settlement. This is to say that the entirety of an column reinforced area may be analyzed by verify that the bearing capacity of a singular cylindrical volume of the host soil with a column in the center. Unit cell idealization has found wide-spread acceptance due to the ease in the design of the apparatus needed to test the group columns. The engineering behavior of a group of columns installed to support a uniformly loaded area was simplified to a single column installed at the center of a cylinder of clay resenting the column's zone of influence (Gniel and Bouazza, 2009).

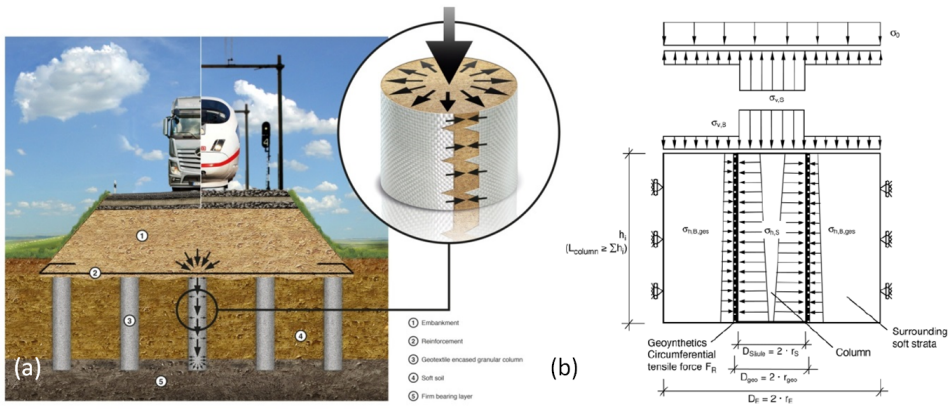

Figure 1.1. (a) A typical cross-section depicting the use of GECs, (b) pressure distribution in a Unit Cell.

When a single Unit Cell is thusly considered, the pressure distribution on the soft soil and the GEC in the geometrical center will be related to their relative stiffnesses. Accordingly, the GEC takes more loads upon itself and there is a certain amount of pressure relief on the part of the soft soil. EBGEO (2011) recommends the use of GECs in very soft soil conditions with the following statement: Geosynthetic-encased columns may be employed as a foundation system for transferring static and variable loads in soft soils (soft strata). One special application and an advantage compared to non-encased columns is based on the support effect of the geosynthetic tube in very soft soils (c_u 15 kN/m^2), e.g. in peat or in very soft silts/clays, such as mud and ooze.

In recent years, geosynthetic encased columns (GECs) have been implemented in various projects to mitigate the problems associated with soft foundation soils. Some of the major projects where GECs have been installed include the following major projects (Alexiew and Raithel, 2015):

- A heavy loaded railroad embankment in Hamburg, Germany (1995),
- Extension of Airbus site Hamburg, Germany (2002),
- Railroad embankment Bothnia Line, Botniabanan, Sweden (2001-2002),
- High speed rail link, Breda, Netherlands (2002),
- Bastions settlement solution, Houten-Zuid, Netherlands (2005),
- Thyssenkrupp CSA steel plant, Rio de Janeiro, Brasil (2006-2010),
- A2 Motorway embankment, Poland 2010-2011.

All of the above specified projects had very stringent settlement requirements and GECs used were supporting rather important infrastructure elements such as rail ways and aviation hangars. The benefits and versatility of GECs to mitigate problems associated with soft soils is well established. Although GECs have proven their viability in many design scenarios, in the currently available design methodologies and literature the use of GECs rarely extends beyond cases where GECs are subjected to static vertical loads. Forthcoming study aims to investigate the potential of GECs to be used as a countermeasure against dynamic loading. In the dissertation study it is aimed to probe into the seismic behavior and performance of the individual GEC as well as

the global seismic behavior and performance of the GEC enhanced embankment and subsoil. For this purpose, various large scale experimental setups have been designed and built. Heavily instrumented GECs and soil containers have been experimented with under 1-g conditions. A large scale shaking table located at Kandilli Observatory and Earthquake Research Institute has been employed in inducing the dynamic base motions to the experimental apparatuses.

A rigid box type apparatus is utilized to study the behavior of GECs that are not subject to free-field conditions. The Rigid Box experiments are run to mimic the field conditions of GECs that are constrained by or closely spaced to relatively rigid foundation elements such as bridge abutments, retaining walls, and sheet piles. In such a design scenario, the free-field boundary conditions of not apply and some reflection of the seismic waves from the nearby rigid foundation elements is expected. It is also anticipated that the deformation of the soft ground will be limited due to the presence of rigid inclusions. A recent study by Schnaid *et al.* (2017) has shown that GECs act as pressure relief systems for bridge abutments by reducing the horizontal earth pressure demand. The GECs are laterally constricted by the presence of the bridge abutment and therefore the GECs and the surrounding soil are not subject to free-field conditions.

Although GECs constricted by rigid foundation elements (GECs installed in close proximity of retaining walls per say) is a design scenario that can be encountered in practice, in most cases GECs will be subjected to free-field conditions. The free-field responses of the GECs and the GEC enhanced soft soil body are studied through laminar box experiments. A novel laminar box is designed and produced for this purpose. The laminar box assembly is heavily instrumented to study the displacement and acceleration of the various bands of the soil body. The displacement and acceleration measurements are used to come up with the shear strains and shear stresses occurring in the soft soil. The soil amplification values are also studied. The strains developing of the reinforcement that is confining the granular material in the columns are also studied in depth to come up with correlations between the seismic input energy and reinforcement's strain response. The differences in behavior of benchmark (untreated)

clay beds and OSC and GEC enhanced clay beds are also considered.

1.2. Research Objectives

With this research it is indented to shed light into:

(i) Modify the existing rigid box assembly to accommodate soft clay samples to accurately model the field conditions of the constrained OSC and GECs,
(ii) Design and construct a laminar box assembly to study the behavior of OSCs and GECs that are subjected to free-field conditions,
(iii) Conduct shaking table tests with the above mentioned rigid box and the laminar box,
(iv) Investigate the behavior of OSCs and GECs under dynamic base excitations such as scaled earthquake accelerograms and sinusoidal motions.
(v) Investigate the behavior of the entirety of the GEC and OSC modified soft soil embankment system,
(vi) Understand the deformation, soil amplification, shear stresses and strains, and damping occurring inside the benchmark and treated soft soil body,
(vii) Draw comparisons between performance of GECs that are reinforced with geotextiles of varying stiffness.

1.3. Dissertation Organization

This dissertation is prepared as a paper-based dissertation where the results pertaining to certain experimental setups are divided inside the chapters of the dissertation and presented. While some of the chapters rely on the excerpts published in the published international peer reviewed journals, some others are based on journal articles that are currently under review. The dissertation is organized as follows:

- Chapter 1 presents the introduction to the study where the back ground and motivation is elaborated. The research objectives and the dissertation organization is also covered within this chapter.

- Chapter 2 gives a clear account of the available literature on the granular columns and the shake table tests conducted with rigid and laminar box type apparatuses.
- Chapter 3 presents materials and used in the experimental study.
- Chapter 4 elaborates the experimental setups used and explains the sample preparation techniques employed.
- Chapter 5 gives a brief description of the shaking table program.
- Chapter 6 presents the results and findings that are gathered from the rigid box apparatus.
- Chapter 7 presents the results of the shaking table tests that are run with the laminar box.
- Chapter 8 presents the Finite Elements analysis undertaken.
- Chapter 9 gives the results and conclusions of the dissertation study. Also included in Chapter 9 are the recommendations for future research.

2. LITERATURE REVIEW

Since there no previous experimental studies on the response of GECs to dynamic loads conducted by making use of a laminar box type apparatus, this chapter of the dissertation is subdivided into two major headings. Firstly the literature on OSCs and GECs is presented in regards to knowhow generated through the analytical design methods, small and large scale laboratory work, and field experiments. In the second part of the literature review, studies conducted with large scale geotechnical dynamic test setups will be evaluated.

2.1. Literature on Geosynthetic Encased Columns and Ordinary Stone Columns

Available literature on enhancement of soil properties via implementation of granular columns is consisted of analytical models, small and large scale laboratory tests, field tests, and finite elements or finite difference models. In this section of the thesis the above mentioned approaches to understand the behavior of granular columns installed in soft soil conditions will be discussed with special attention and detail given towards geosynthetic encased columns (GECs). Table 2.1 and Table 2.2 are expanded versions of the tables provided by Najjar (2013) which include the list of relevant studies that deal with the ordinary and geosynthetic encased columns implemented in soft soils. Table 1 classifies the studies according to the type of the study conducted. The experimental studies are further explained by specifying the type of the study (i.e. field experiments, small scale triaxial testing, centrifuge tests, tests conducted in large scale rigid tanks, etc.). The loading conditions and the column dimensions of the experimental work are also specified. Among other relevant parameters pertaining to the studies, Table 2.1. accounts for the area replacement ratio used, presence and type of encasement, and soil type used in the experiments.

Table 2.1. Works on GECs and OSCs in the literature.

Reference		General	Design / Analysis	Experiment	Type of Experiment (S=single, G=Group)	Type of Loading	Foundation Size (cm)	Test Sample Size (cm x cm x cm)	Column Dimensions (cm)
Greenwood	1970	+	-	-	-	-	-	-	-
Bauman and Bauer	1974	-	+	+	Field (G)	F	135	-	D=100, L=550
Hughes and Withers	1974	-	+	+	1-g (S)	C	-	22.5x16x15	D=1.25-3.8
Hughes *et al.*,	1975	-	-	+	Field (S)	C	66	-	D=73, L=700
Greenwood	1975	-	-	+	Field (S)	F	91	-	D=58, L=290
Brauns	1978	-	+	-	-	-	-	-	-
Mitchell	1981	-	+	-	-	-	-	-	-
Charles and Watts	1983	-	-	+	1-g (S)	A	-	D=100, H=60	D=4.5, 35, 45.5, 50, 57.2
Barksdale and Bachus	1983	-	+	-	-	-	-	-	-
Bachus and Barksdale	1984	-	-	+	1-g (S/G)	A	-	D=10.8, H=30.5	D=2.93, 5.33 L=30.5
Bergado *et al.*,	1987	-	-	+	Field (S)	C + F	30-120	-	D=30, L=800
Bergado and Lam	1987	-	-	+	Field (S)	C	-	-	D=30, L=800
Juran and Guermazi	1988	-	-	+	TX (S)	A	-	D=10, H=20	D=2, 4 L=800
Han and Ye	1991	-	-	+	1-g (S)	F	1.5D	100x80x100	D=2.5, 5, 7.5
Narasimha Rao *et al.*,	1992	-	-	+	Field (S)	C + F	125	-	D=85, L=1200
Priebe	1995	-	+	-	-	-	-	-	-
Rajagopal *et al.*,	1999	-	+	+	TX (S/G)	C	-	Sand only	D=100
Watts *et al.*,	2000	-	+	+	Field (S)	F	75	-	D=60, L=300-400
Raithel and Kempfert	2000	-	+	-	-	-	-	-	-
Muir Wood *et al.*,	2000	-	-	+	1-g (G)	F	10	D=30	D=1.1, 1.75, L=30
Malarvizhi and Ilamparuthi	2004	-	-	+	1-g (S)	F	7	D=30, H=28	D=3, L/D=5-9.33
Sivakumar *et al.*,	2004	-	-	+	TX (S)	A + F	4	D=10, H=20	D=3.2, L/D=8, 12, 16, 20
Lillis *et al.*,	2004	-	-	+	Field (S)	C	-	-	D=31, L=300
McKelvey *et al.*,	2004	-	-	+	1-g (G)	F	9 x 9	D=41.3, H=50	D=2.5, L/D=6, 10
Ayadat and Hanna	2005	-	+	+	Chamber (S)	F	4	D=39, H=52	D=23, L/D=10.9, 13, 17.8
Kim and Lee	2005	-	-	+	Centrifuge (G)	F	10 x 6	25x10x25	D=2.2, L/D=6.8
Murugesan and Rajagopal	2006	+	-	-	FEM	-	-	-	-
Black *et al.*,	2006	-	-	+	Ko -TX (S)	F	6	D=30, H=40	D=2.5, L/D=6, 10
White *et al.*,	2007	-	-	+	Field (S/G)	C + F	229	-	D=76, L=279, 510
Black *et al.*,	2007	-	-	+	TX (S/G)	-	-	D=10, H=20	D=3.2
Ambily and Gandhi	2007	-	+	+	1-g (S/G)	A + C	-	D=21, 42, 83	D=10, L/D=4.5
Murugesan and Rajagopal	2008	-	+	+	1-g (S)	C	-	D=21, H=50	D=5, 7.5, 10
Andreou *et al.*,	2008	-	-	+	TX (S/G)	-	-	D=10, H=20	D=2, L/D=10

Table 2.1. Works on GECs and OSCs in the literature (cont.).

Reference		General	Design / Analysis	Experiment	Type of Experiment (S=single, G=Group)	Type of Loading	Foundation Size (cm)	Test Sample Size (cm x cm x cm)	Column Dimensions (cm)
Elshazly *et al.*,	2008a	+	-	+	FEM/Field (S)	F	200	-	D=100, L=1100
Elshazly *et al.*,	2008b				FEM	-	-	-	-
Chen *et al.*,	2009	+	-	-	FEM/Field (S)	C	-	-	D=84, L=505
Wu and Hong	2009	-	+	+	TX (S)	C	-	Sand only	D=7, L/D=2
Gniel and Bouazza	2009	-	-	+	1-g (S)	A + C	-	D=15.5, H=31	D=5.1, L/D=6
Lo *et al.*	2010	+	-	-	FEM	-	-	-	-
Murugesan and Rajagopal	2010	-	+	+	1-g (S/G)	F	2.0D	120x120x0.60	D=5, 7.5, 10
Najjar *et al.*,	2010	-	-	+	TX (S)	A	-	D=7.09, H=14.1	D=2, 3, L=7, 10, 14
Pulko *et al.*,	2011	-	+	-	-	-	-	-	-
Castro and Sagaseta	2011	-	+	-	-	-	-	-	-
Black *et al.*,	2011	-	-	+	Ko -TX (S/G)	F	6	D=30, H=40	D=2.5, 3.2, 3.8, L=12.5, 25, 40
Sivakumar *et al.*,	2011	-	-	+	TX (S)	F	6	D=30, H=40	D=4, 5, 6, L=40
Cimentada *et al.*,	2011	-	-	+	1-D Cons (S/G)	A	-	D=24.5, H14.6	D=6.35, 8.47
Shahu and Reddy	2011	-	-	+	1-g (G)	F	10	D=30, H=30	D=1.3, 2.5, L=10, 15
Fattah *et al.*,	2011	-	-	+	1-g (S/G)	F	22	110x100x40	D=50, L/D=6, 8
Stuedlein and Holtz	2012	-	-	+	1-g (S/G)	C + F	2.74 m	-	D=76, L=305, 457

Table 2.2. Details pertaining to studies tabulated in Table 1.

Reference	Year	Area Replacement ratio (%)	Encased/ Ordinary	Type of Encasement	Soil Type	Column Type	Clay cu (kPA)
Greenwood	1970	-	-	-	-	-	-
Bauman and Bauer	1974	47	O	-	Silty clay	Aggregates	8-16
Hughes and Withers	1974	-	O	-	Kaolin	Leighton buzzard	19
Hughes et al.,	1975	-	O	-	Grey silty	River gravel	22
Greenwood	1975	40.6	O	-	Boulder	Gravel	4.4
Brauns	1978	-	-	-	-	-	-
Mitchell	1981	-	-	-	-	-	-
Charles and Watts	1983	0.2, 12, 21, 25, 33	O	-	Boulder	Uniform gravel	30
Barksdale and Bachus	1983	-	-	-	-	-	-
Bachhus and Barksdale	1984	7 and 25	O	-	Kaolin	Quartz	14.4-19.1
Bauman and Bauer	1987	6-100	O	-	Bangkok	Crushed limestone	20-45
Bergado and Lam	1987	-	O	-	Bangkok	Sand/gravel	20-45
Juran and Guermazi	1988	4 and 16	O	-	Silt	River sand	$\varphi = 32$
Han and Ye	1991	44.4	O	-	Marine clay	Granite chips	Soft/M.Stiff
Narasimha Rao et al.,	1992	36 and 100	O	-	Silty clay	Crushed gravel	15
Priebe	1995	-	-	-	-	-	-
Rajagopal *et al.*,	1999	-	E	geocells	No clay	River sand	-
Watts et al.	2000	-	O	-	Ash/Clay	Stones	$\varphi = 36$, $c_u = 40$
Raithel and Kempfert	2000	-	-	-	-	-	-
Muir Wood *et al.*,	2000	10-30	O	-	Kaolin	Quartz	12
Malarvizhi and Ilamparuthi	2004	-	E	Geogrid	Marine	Granite chips	6
Sivakumar et al.,	2004	10.2	E	Geogrid	Kaolin	-	28
Lillis *et al.*,	2004	-	O	-	Clay	-	SPT 5-20
McKelvey et al.,	2004	24	O	-	Kaolin	-	32
Ayadat and Hanna	2005	-	E	Fabric	Sand/kaolin	Coarse	$\varphi = 30$, c_u 0 = 35
Kim and Lee	2005	30, 40, 50	O	-	CH	Sand/gravel	12
Murugesan and Rajagopal	2006	17	O	-	Kaolin	Crushed basalt	35
Black *et al.*,	2006	-	E	-	-	-	-
White *et al.*,	2007	35	O	-	CL clay	Crushed limestone	30
Black *et al.*,	2007	10 and 12	O	-	Kaolin	Medium	28
Ambily and Gandhi	2007	5.7, 10.1, 22.7	O	-	CH	Stones	7, 14, 30
Murugesan and Rajagopal	2008	-	E	Geot/grid	Lake	Granite chips	2.5

Table 2.2. Details pertaining to studies tabulated in Table 1 (cont.).

Reference	Year	Area Replacement ratio (%)	Encased/ Ordinary	Type of Encasement	Soil Type	Column Type	Clay cu (kPA)
Andreou et al.,	2008	4		-	Kaolin	sand/gravel	$c_u/\sigma' = 0.25$
Elshazly *et al.*,	2008a	21, 26.7, 40.2	8	-	Clay/sand	Gravel	-
Elshazly et al.,	2008b	-	-	-	-	-	-
Chen et al.,	2009	-	O	-	Alluvial	Aggregate	-
Wu and Hong	2009	-	E	Geot.	No clay	Quartz	-
Gniel and Bouazza	2009	11	E	Geogrid	Kaolin	Poorly graded	5
Lo et al.,	2010	-	E	-	-	-	-
Murugesan and Rajagopal	2010	20, 23	E	Geot/grid	Lake	Granite chips	2.5
Najjar et al.,	2010	7.9, 17.8	E		Kaolin	Quartz	$c_u/\sigma' = 0.30$
Pulko *et al.*,	2011	-	E	Geot. -	-	-	-
Castro and Sagaseta	2011	-	E	-	-	-	-
Black et al.,	2011	17, 28, 40	O	-	Kaolin	Crushed basalt	35
Sivakumar et al.,	2011	44.4, 69.4, 100	O	-	Kaolin	Crushed basalt	35
Cimentada et al.,	2011	6.25, 11.11	O	-	Kaolin	Gravel	c_u/σ'=0.30
Shahu and Reddy	2011	10, 20, 30	O	-	Kaolin	Barbadur sand	7-9
Fattah et al.,	2011	5.1, 10.2, 15.3, 20.4	O	-	CL	Crushed stones	6, 9, 12
Stuedlein and Holtz	2012	30 and 100	O	-	Beaumont	GP and GW-GM	44-70

Further define the bulging failure criteria of a vertically loaded stone column by defining a critical state of stress at the top portion of the column with the following expression:

$$q_{ult} = \frac{1 + sin\phi'}{1 - sin\phi'} (\sigma_{ro} - u - 4c) \tag{2.1}$$

where c and u are the undrained shear strength and pore water pressure and ϕ is the angle of friction of the aggregate constituting the column. Hughes and Withers (1974) also define a column diameter to depth ratio of 6.3 beyond which increase in length of the column will not increase the vertical load capacity of the column. Bauman and Bauer (1974) came up with a calculation model that differentiates between the immediate settlement and the consolidation settlement of the soft soil enhanced with the stone columns.

Brauns (1978) approach to define the bulging failure was to assume that the failure with in the stone column would take place in the top portion of the column with the failure occurring at a height of $h_y = d_p \tan\delta_p$ where d_p is the diameter of the stone column. Brauns (1978) came to this conclusion by assuming that the behavior of the column will be similar to the behavior of a granular material specimen tested at a triaxial apparatus. It follows that the shear planes will be oriented at an angle that is 45 degrees more than the critical effective internal angle of friction of the material. Brauns (1978) further assumes that the material surrounding the column has an internal angle of friction of zero in which case the lateral support provided by the soft soil is independent of depth. With all these assumptions and simplifications Brauns (1978) proposed the following equation to characterize the maximum vertical stress that can be supported by a stone column under surcharge loading:

$$q_{ult} = \left(q + \frac{2c}{sin2\delta_p}\right) \left(1 + \frac{tan\delta_p}{tan\delta}\right) \tan^2\delta_p \tag{2.2}$$

After reviewing the available literature at the time, Mitchell (1981) proposed an empirical relationship to estimate the ultimate load capacity of a singular granular column.

The proposed empirical formula was: $q_{ult} = \mathrm{cN}_p$. The bearing capacity factor according to Mitchell (1981) was equal to 25. Later, the proposed bearing capacity factor was modified by Barksdale and Bachus (1983) to be in between 18 to 22 for columns implemented with vibration depending on the strength parameters of the soft soil. Barksdale and Bachus (1983) stated that the unit cell concept can be used to determine the capacity of a group of granular piles. Barksdale and Bachus (1983) calculated the averaged strength parameters of the column enhanced soil as a whole by adding the contribution of the columns to the ordinary strength parameters of the soil. The average interal angle of friction and cohesion of the soil becomes:

$$\phi_{avg} = \tan^{-1}\left(na_r \times tan\phi'\right) \tag{2.3}$$

$$c_{avg} = \left(1 - a_r\right)c \tag{2.4}$$

where n is the stress concentration factor and a_r is the area replacement ratio which is defined as the area of the stone columns to area of the entire soft soil in plan. To calculate the ultimate capacity for a group, firstly the ultimate lateral pressure needs to be determined. For an infinitely long footing from classical earth pressure theory for a saturated clay having only cohesion is (Barksdale and Bachus, 1983):

$$\sigma_3 = 0.5\gamma_c B tan\left(45 + \frac{\phi_{avg}}{2}\right) + 2c \tag{2.5}$$

where: $sigma_3$ average lateral confining pressure; γ_c saturated or wet unit weight of the cohesive soil; B foundation width; c undrained shear strength within the unreinforced cohesive soil.

The lateral confining pressure for a square foundation can be determined using the cavity expansion theory of Vesic. The Vesic cylindrical expansion theory gives the ultimate stress that can be exerted on the failure block by the surrounding soil. The three-dimensional failure on a cylindrical surface should give a satisfactory approxima-

tion of the three dimensional failure of a square foundation (Barksdale and Bachus, 1983). The bearing capacity of a group of OSCs can be calculated with the following formula:

$$q_{ult,group} = \sigma_3 \tan^2\left(45 + \frac{\phi_{avg}}{2}\right) + 2c_{avg}\tan\left(45 + \frac{\phi_{avg}}{2}\right) \tag{2.6}$$

An improvement factor in the mechanical properties of soft clay due to column installation by vibro-replacement technique was defined by Priebe (1995). Priebe (1995) assumes that (i) the column is based on a rigid layer (ii) the column material is uncompressible (iii) the bulk density of the column and soil is neglected. The improvement of a soil achieved at these conditions by the existence of stone columns is evaluated on the assumption that the column material shears from the beginning whilst the surrounding soil reacts elastically. Furthermore, the soil is assumed to be displaced already during the column installation to such an extent that its initial resistance corresponds to the liquid state: i.e. the coefficient of earth pressure amounts to K=1.The result of the evaluation is expressed as basic improvement factor n_o.

$$n_o = 1 + \frac{A_c}{A}\left[\frac{\left(5 - \frac{A_c}{A}\right)}{4K_{ac}\left(1 - \frac{A_c}{A}\right)} - 1\right] \tag{2.7}$$

Watts *et al.* (2000) has carried out full scale instrumented load tests to study the installation and performance of vibro-stone columns supporting a strip foundation. The performance of the strip foundation in a benchmark test where the soft ground was not modified was also monitored. According to Watts *et al.* (2000) stone columns are designed on the assumption that they are acted upon by a triaxial stress system and are assumed to be in a state of shear yield at a critical depth h. Many authors have proposed approximations for the stress system. However, the approach given by Hughes and Withers (1974) for cohesive soils is often adopted. Their operating

equation can be rewritten as

$$\sigma'_{vc} = K_{pc} \left(K_o \left[\gamma_s h - u_{so} \right] + u_{so} - u_s + 4c_u \right) \tag{2.8}$$

where K_{pc} is the coefficient of the passive earth pressure for the column materials and K_o is the at rest earth pressure coefficient for the virgin soft soil. The initial and at yield pore water pressures at a depth of h are u_{so} and u_s, respectively.

Ambily and Gandhi (2007) undertook an experimental and finite elements study to probe into the behavior of single and grouped granular columns. Ambily and Gandhi (2007) state that the theories developed Greenwood (1970), Hughes and Withers (1974), and Hughes *et al.* (1976) predict the capacity of a single stone column in infinite soil mass, which does not consider the effect of spacing and surcharge. The calculation model developed by Ambily and Gandhi (2007) incorporates the effect of spacing between columns based on unit cell concept. When the surcharge load on the surrounding clay is also considered, there is a considerable increase in load carrying capacity. Based on the finite elements analysis Ambily and Gandhi (2007) proposed a series of curves for the limiting axial capacity of a group of stone columns. The proposed curves are illustrated in Figure 2.2. Further, an empirical expression that defines the limiting axial capacity that considers the effects of the surcharge load was also proposed:

$$\sigma_{suq} = \sigma_{su} + \left(0.0088\phi'^2 - 0.5069\phi' + 10.86q \right) \tag{2.9}$$

where σ_{suq} is the limiting axial stress with a surcharge (q) on the surrounding clay and ϕ' is the friction angle of the column.

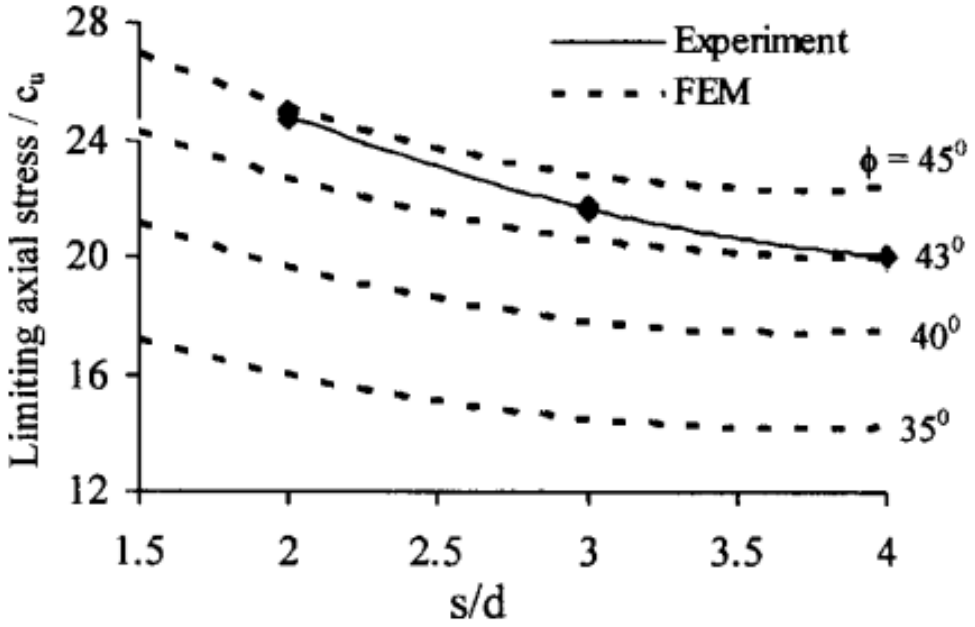

Figure 2.1. Limiting axial capacity curves proposed by Ambily and Gandhi (2007).

2.1.1. Design Methods for Encased Stone Columns

Raithel and Kempfert (2000) was probably the first group of researchers to come up with an iterative design tool on the vertical load carrying capacity of GECs. The analytical axisymmetric calculation model was based on the unit cell concept and the essential boundary conditions and stresses acting in a singular unit cell are depicted in Figure 2.1. Raithel and Kempfert (2000) assumed that the column head plane settles as a single horizontal line under the action of the applied overburden pressure. That is to say that in a given unit cell, the soft soil and the GEC settled by the same amount. Following assumptions were made (Raithel and Kempfert; 2000):

- The settlements occurring in the bearing strata under the GECs can be neglected.
- The granular infill material in the column is at a K_a (active earth pressure) state
- Depending on the method of column installation, the at rest earth pressure is calculated as $K_s = K_{o,s}$ = 1-sin$\emptyset$ for replacement columns or as for $K_s = K_{o,s*}$ displacement columns.

- The reinforcement geotextile is linear-elastic,
- For design of the foundation the drained (end) condition is decisive, because then the maximum settlements and ring tension forces are reached.

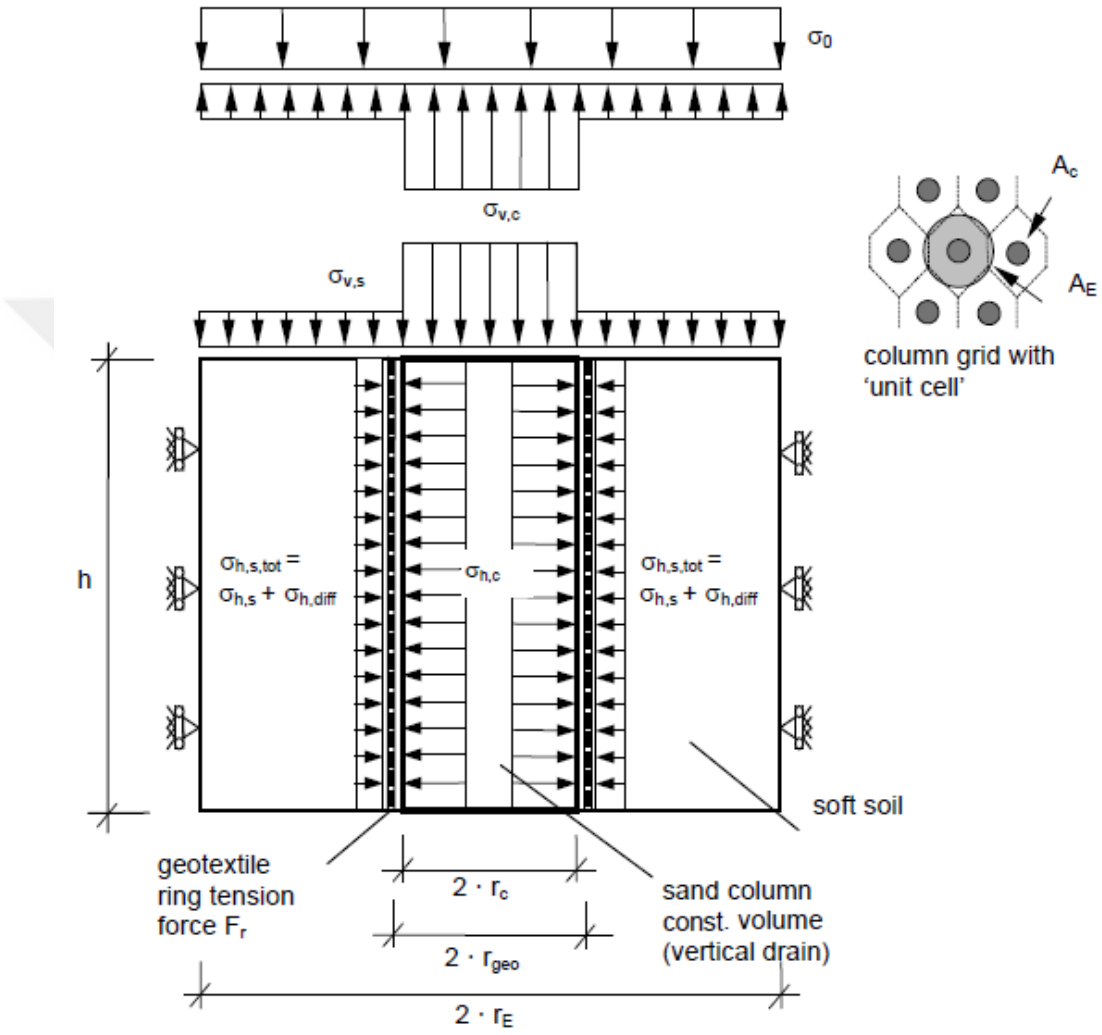

Figure 2.2. The calculation model "geotextile coated sand column" (Raithel and Kempfert, 2000).

Other than the above specified assumptions, the model proposed by (Raithel and Kempfert; 2000) inherently assumes that the column bulges throughout its entire height with a constant volume of the column constituents. The predicted column capacity and load settlement behavior is compared against PLAXIS models and it was seen that the model's predictions were within reasonable agreement with the finite elements models. The finite elements models incorporated Cam-Clay material model for the soft

clay and Duncan-Chang model for the stone column material.

Ayadat and Hanna (2005) undertook an experimental program to come up with a calculation method for GECs embedded in collapsible soils. The equation proposed by Ayadat and Hanna follows the form of the equation proposed by Briaud (1991) where the vertical stress acting on an ordinary stone column is given by

$$\sigma'_{vlim} = \tan^2\left(\frac{\pi}{4} + \frac{\phi'}{2}\right)\sigma'_{hmax} \tag{2.10}$$

where σ'_{vlim} is the maximum effective vertical stress acting on the ordinary stone column; ϕ' is the angle internal of shearing resistance of the infill material for the ordinary stone column; and σ'_{hmax} is the maximum effective lateral pressure that the soil and the geotextile reinforcement can provide which is in the form of

$$\sigma'_{hmax} = \sigma'_{hs} + \delta\sigma \tag{2.11}$$

where σ'_{hmax} is the maximum effective lateral pressure provided by the soil around the column, and $\delta\sigma$ is the additional pressure that contributes to the reinforcement of the column.

The maximum effective lateral pressure provided by the soil around the column can be calculated by the following equation (Hughes and Withers, 1974).

$$\sigma'_{hs} = \sigma'_{h0} + kc' \tag{2.12}$$

with σ'_{hs} being equal to

$$\sigma'_{h0} = k_o\left(q + \frac{\gamma L}{2}\right) \tag{2.13}$$

Here σ'_{h0} is the effective lateral stress of the soil before installing the column; c' is the drained cohesion of the collapsible soil; k_0 is the coefficient of earth pressure at rest; q is the surcharge applied on the ground surface; L is the length of the stone column; and k is a coefficient (k = 4; Hughes and Withers, 1974).

The additional lateral confinement offered by the reinforcing geotextile can be estimated by making use of the tensile strength of the material. Referring to Figure 2.3, the following equation can be writing for the force equilibrium:

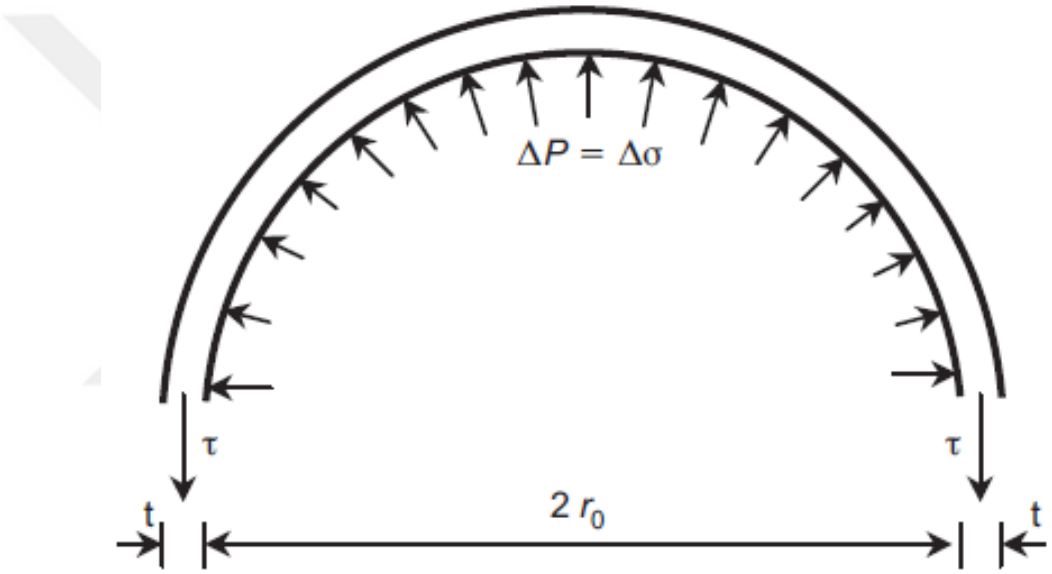

Figure 2.3. Cross-section of the GEC subjected to lateral internal pressure.

$$\delta\sigma \times 2r_o = 2\tau_a t \tag{2.14}$$

$$\delta\sigma = \frac{\tau_a t}{r_o} \tag{2.15}$$

where r_o is the initial radius of the column, and t is the thickness of the geotextile reinforcement. Substituting $\sigma_h s'$ and $\delta\sigma$ in equation (10), the ultimate load that can be carried by a geosynthetic encased stone column can be extrapolated by the following

equation:

$$\sigma'_{vlim} = \tan^2\left(\frac{\pi}{4} + \frac{\phi'}{2}\right)\left(\sigma'_{h0} + kc' + \frac{\tau_a t}{r_o}\right) \tag{2.16}$$

Based on Ayadat and Hanna's (2005) observations, the sand columns failed by bulging before the reinforcement geotextile failed in tension. Therefore a reduction term for the last part of the equation (16) was proposed to account for the premature failure of the column material. The reduction factor α, has a value between zero and unity.

$$\sigma'_{vlim} = \tan^2\left(\frac{\pi}{4} + \frac{\phi'}{2}\right)\left(\sigma'_{h0} + kc' + \alpha\frac{\tau_a t}{r_o}\right) \tag{2.17}$$

An empirical relationship to determine the value of α was also proposed by Ayadat and Hanna (2005) which is in the following form:

$$\alpha = 3.2 \times 10^5 E_p^{-1.37} \tag{2.18}$$

where E_p is the modulus of elasticity of the stone column.

Murugesan and Rajagopal (2010) run a series of laboratory experiments to come up with a design methodology for GECs. The researchers have also provided guidelines for the design of GECs that are embedded in soft soils where the undrained cohesion of the host soil is less than 20 kPa. The step by step design method is as follows:

(i) For the given pressure loading p_o from the structure, suitable spacing (s) and diameter (d) of the stone columns are chosen. A typical unit cell consisting of a stone column and the contributing surrounding soil is considered among the grid of stone columns. The load on the unit cell area is assumed to be carried fully by the stone column alone in the unit cell. Load on the stone column = applied pressure p_o x Area of the unit cell A. Area of the unit cell for a square pattern

of columns is A = π x $(0.525s)^2$ and for a triangular arrangement of columns; A = π x $(0.525s)^2$ where s is the spacing of the columns. Load on stone column = load on the unit cell = p_o x A. Therefore pressure on the stone column = load on the unit cell/area of the stone column A_c.

(ii) The limiting vertical pressure on the OSC is calculated by the equation below:

$$\sigma_v = (\sigma'_{ro} + 4c)\, K_{p,col} \tag{2.19}$$

where σ'_{ro} is the initial effective radial stress calculated at an average depth around twice the diameter of the column, c is the undrained cohesion of the soft clay and $K_{p,col}$ is the coefficient of passive earth pressure of the granular matter in the column.

(iii) The additional confinement that is to be provided by the geotextile reinforcement is calculated as follows:

$$p_c = \left(p_o - \frac{\sigma_v}{K_{p,col}}\right) \tag{2.20}$$

(iv) The corresponding hoop tension force in the encasement geotextile (T) can be estimated as T = p_cd/2 where d is the diameter of the stone column.

(v) The hoop strain ε_a in the encasement corresponding to the permissible settlement δ in the stone column is computed using the following equation:

$$\varepsilon_c = \frac{1 - \sqrt{1 - \varepsilon_a}}{\sqrt{1 - \varepsilon_a}} \tag{2.21}$$

in which ε_a is the axial strain in the stone column. This value can be evaluated from the surface settlement of the stone column treated ground, δ as $\varepsilon_a = \delta$ /4d.

(vi) A suitable geosynthetic that can develop the long term allowable design tensile strength, T within a strain level of ε_c can be chosen for the encasement.

Pulko *et al.* (2011) introduced a design method and a corresponding calculation model for GECs. The proposed closed-form analytical solution is based on the previously explained analytical models. The findings of the analytical model are checked against finite elements modeling of the problem. Parameters included in the calculation model are the stiffness ratio of the GEC to surrounding soft clay, internal angle of friction and dilation angle of the column infill material, Poisson's ratio, column spacing, reinforcement stiffness, initial stress state of the column material and the soft soil, and applied vertical pressure.

2.1.2. Engineering Behavior of Ordinary and Encased Stone Columns

While the most commonly acknowledged mode of failure for OSCs and GECs is the bulging failure mode, there are two other failure modes of interest for the design of OSCs and GECs which are the shear and bending failure modes. When the surrounding soil is composed of soft clayey material, OSCs typically fail in bulging. In order to mitigate bulging failure, the column constituents are often encased with a high modulus - low creep geotextile which gives rise to GECs.

The failure behavior of OSCs in bulging mode is closely related to the ratio of the diameter of the column to its height (L/D). McKelvey (2002) investigated the behavior of ordinary stone columns under pad and strip footings and postulated that short columns (L/D ratio lower than 6) failed in end bearing. The study has revealed that the long columns (L/D ratio higher than 6) failed by bulging. These findings were in agreement with the previous observations made by Hughes and Withers (1974), Wood *et al.* (2000), and Najjar *et al.* (2010). The end bearing failure mechanism for partially penetrating short columns can be explained by a punching-like mechanism where the bearing capacity of the soft soil at the base of the column is exhausted by the vertical load that is transferred by the column. Bulging failure depths for OSCs proposed in the literature typically ranges from D to 4D. Various researchers have stated the bulging depth as follows:

- Malarvizhi and Ilamparuthi (2007) have observed the bulging of the model scale stone columns to be at a depth of 4D. They have also observed an increase in the column capacity as the height of the stone column increased.
- Ghazavi and Afshar (2013) has stated that bulging failure mode governs single stone columns with the bulging failure typically occurring at a depth of D to 2D from the column head plane.
- Hong *et al.* (2016) has stated that for ordinary stone columns and for geosynthetic encased stone columns of low reinforcement stiffness the bulging depth is about 2.5 column diameters below the column head plane.

Bulging failure depths for GECs proposed in the literature typically ranges from D to 3D. Various researchers have stated the bulging depth as follows:

- Malarvizhi and Ilamparuthi (2007): Maximum hoop force in the geogrid reinforcement was observed at a depth of 1D for all applied vertical load levels. Consequently, researchers expected bulging failure to occur at this particular depth.
- Gniel and Bouazza (2009): Observed bulging depth for GECs embedded in kaolinite clay in small scale laboratory apparatus to be at a depth of 2D.
- Gu *et al.* (2016) have stated that bulging depth for GECs is within 3D and therefore this is the optimal depth to which the partially reinforced columns should be fitted with reinforcement sleeves.

A wide range of field and laboratory tests has been undertaken to study the behavior of GECs and OSCs. A vast majority of these tests were carried out by applying static and vertical loads on the model columns. The exceptions to this are the studies conducted by Murugesan and Rajagopal (2009) and Mohapatra *et al.* (2016) where model ordinary stone columns (OSCs) and GECs embedded in sand are sheared in large scale direct shear type apparatus. The shear mode of failure is identified in the works of the above mentioned researchers.

Murugesan and Rajagopal (2009) have investigated the behavior of ordinary stone columns and geosynthetic encased stone columns embedded in soft soils under shear

loads by making use of a large scale direct shear box (300 by 300 by 200 mm deep) and a large plane strain steel tank. The soft soil was clay acquired from a lake bed and it was consolidated in laboratory conditions under an overburden pressure of 10 kPa. A woven and nonwoven geosynthetic material with ultimate tensile strengths of 20 and 6.8 kN/m were used as reinforcements for the GECs. The study concluded that the measured shear load capacity of the ordinary stone column in large scale direct shear apparatus was found to be approximately half of the resistance calculated on the basis of the strength of individual materials. It was also seen that the performance of geosynthetic encased stone columns were superior to that of ordinary stone columns under shear loading. The geosynthetic encased stone columns were found to offer higher lateral resistance due to the confinement of the aggregate in the columns. The study emphasized that the encased stone columns were especially suitable for resisting the lateral loads at the toe of embankments and retaining walls due to their improved lateral load response.

Mohapatra *et al.* (2016) have also worked on the behavior of GECs and OSCs by means of a large scale direct shear apparatus having plan dimensions of 305 x 305 mm and a depth of 203 mm. The confining soft soil was selected as a dry sand. The researchers report that sand was used to prepare the soil bed in place of normally consolidated clay soil due to the ease of placement, ease of achieving consistency between the tests and similarity of strength behavior. The researchers also acknowledge that the use of dry sand in place of saturated soft clay does not allow the simulation of localized drainage effects around the stone columns, which can potentially increase the undrained shear strength of the surrounding clay (Mohapatra *et al.* 2016). The sand-OSC and sand-GEC composites are sheared under overburden pressures ranging from 15 to 75 kPa. Depending on the stiffness of the geosynthetic encasement, GECs exhibited two different types of shear failures. In the case of the GECs encased by high stiffness reinforcements, the encasement was completely sheared along with the granular column (Type 1 failure). When the GEC was reinforced with low stiffness reinforcement however, the reinforcement did not undergo rupture, instead the GEC deformed excessively in the shear plane and the reinforcement physically followed that pattern of deformation (Type 2 failure). The failure types defined by Mohapatra *et*

al. (2016) is illustrated in Figure 2.4. The findings of this study could be summarized as follows: (i) geosynthetic encasement increases the lateral load capacity of granular columns due to mobilization of tensile forces in the encasement layer, (ii) the resistance of GEC increases with increasing shear displacements until complete rupture of encasement material occurs, (iii) the encasement with higher modulus mobilizes higher lateral resistance forces at smaller displacements.

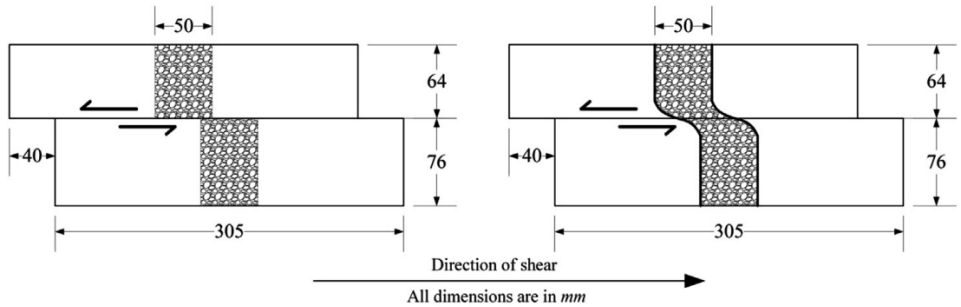

Figure 2.4. Failure modes of GECs as defined by Mohapatra *et al.*, (2016).

Chen *et al.* (2015) has identified a third and probably more destructive mode of failure for OSCs and GECs. The failure mode identified by Chen *et al.* (2015) is the bending failure that is most likely to be seen in the edges of a vertically loaded embankment (as depicted in Figure 2.5). The bending of the columns is caused by the lateral movement of the embankment and the subsoil below the embankments. The unbalanced lateral earth pressure also causes the bending of the columns. The conclusions drawn by Chen on the bending failure mode of GECs are as follows: (i) The predominant failure mode for columns supporting embankment loads is bending. Bending occurs due to the sliding of the embankment itself and the foundation soil. A net unbalanced lateral force acts on the columns. (ii) The column behaves as a long pile and at a given depth of capacity exhaustion a plastic hinge occurs. (iii) The largest bending demand is concentrated in the outermost column in the width of the embankment. Consequently, the researchers suggest that an additional row of columns to be implemented to mitigate the lateral spreading failure.

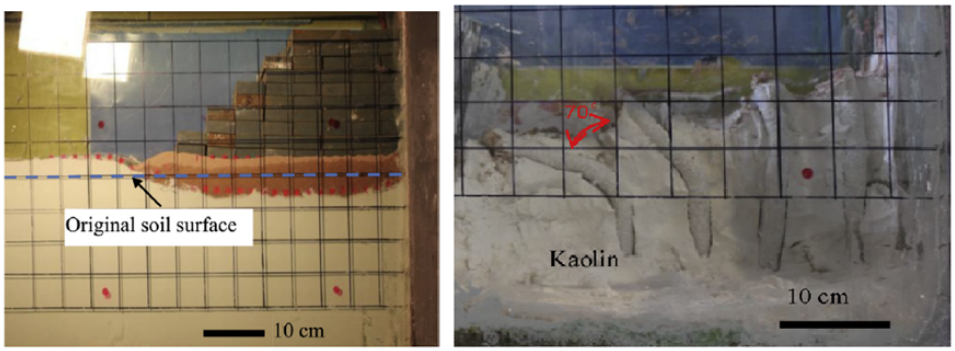

Figure 2.5. Columns failed in bending (Chen *et al.*, 2015).

A certain amount of lateral expansion of the column is required for the onset of the confinement that is provided by the reinforcement to occur. The term that is coined by Raithel and Kempfert (2000) for the process of lateral column expansion to trigger lateral confinement is activation widening. The lateral strains that are needed to achieve the confinement offered by the reinforcement are also incorporated in their analytical calculation model. Since the installation technique of the GECs do not allow for compaction of the granular material the design of GECs is increasingly undertaken with stiffer and more robust reinforcement geosynthetics (Gniel and Bouazza, 2009). When the settlement requirements are stringent, such as the case in the A2 Motorway Embankment constructed in Poland (2010-2011), preloading of the embankment is practiced (Alexiew *et al.*, 2005). When the settlement criteria is not strictly controlled or the settlement of the superstructure can be allowed, the settlements occurring under the self-weight of the embankment may be adequate to initiate the activation widening and subsequent confinement of the granular material in the columns.

Murugesan and Rajagopal (2007) have proposed that the presence of the geosynthetic reinforcement aided in preventing the penetration of the soft clay into the aggregates of the GEC. It is also proposed that the non-contamination of the column constituents would result in better performance of the GECs in long term because the frictional properties of the aggregate will not be altered. An experimental study on the improvement of soft soil bearing capacity with geogrid reinforced columns was undertaken by Gniel and Bouazza (2009). Upon completion of the tests, bisection of the

model columns revealed significant ingress of the clay material in between the aggregate in the model column which is suggestive of decreasing the column capacity and impairing the column's ability to act as a vertical drain.

Murugesan and Rajagopal (2007) state that the perforce of partially encased columns were very close to those of fully encased columns. They have also noted that beyond a certain vertical pressure strain-softening is observed in partially encased columns. Murugesan and Rajagopal (2007) have observed a reduction in the confinement offered by the reinforcement for the larger diameter GECs. An increase in the column capacity was noted for stiffer reinforcements in GECs. Encasing the column reduced the stress concentration of the weak clay thereby reducing the overall settlements of the model soil layer. Maximum hoop force in the geogrid reinforcement was observed at a depth of 1D for all applied vertical load levels. An increase in the diameter to height ratio of the column (L/D) reduced settlements until the ratio reached a value of 10. Beyond this value further increase of column height did not aid in settlement reduction. The shear resistance of the column material was not as effective as the encasement stiffness to reduce the settlements. Murugesan and Rajagopal (2007) state that the perforce of partially encased columns were very close to those of fully encased columns. They have also noted that beyond a certain vertical pressure strain-softening is observed in partially encased columns.

In addition, it is expected that the readily examined occurrence of radial column bulging may be used to help reduce the length of encasement required to reinforce a column. For isolated columns, radial bulging is typically confined to the upper section of the column and it is expected that encasement of only this bulge zone may adequately reinforce the column. For group columns, bulging behavior is not well understood. Muir-Wood *et al.* (2000) used results from small-scale group tests to show that confinement from adjacent columns significantly reduced column bulging. However, it is still expected that the lower lateral earth pressures and lower stiffness of near-surface soils will cause greater radial expansion in the upper section of full-scale group columns. As such, partial encasement of the upper section of model columns was incorporated into the testing program to investigate the impact on vertical and

radial column deformation (Gniel and Bouazza; 2009).

2.2. Literature on Large Scale Dynamic Testing

When dynamic testing is undertaken in field conditions, since the lateral boundaries are at an infinite extent the reflection of waves from the boundaries of the field is not possible. A vast majority of the dynamic soil testing however are conducted at laboratory scale with test setups of finite dimensions. The model boundaries at laboratory scale testing brings about potential pitfalls to accurate measurement of the soil properties. The waves generated by the test setup, for example a shaking table, typically induce shear waves to the model. This causes shear waves to propagate through the model soil medium. The soil particles that are close to the boundaries of the model may undergo cycles of compression and extension and this mechanism may cause pressure waves. Generated waves could also be reflected from the boundaries of the model. In the absence of large soil body covering the area of interest (or the model), the attenuation of the waves is not possible. This may cause an interaction between the P and S waves and create loading scenario where the intensity of the loading is much more severe than the loading that typically occur in field conditions (Bhattacharya *et al.*, 2012).

Various container types are employed to contain the model soil in dynamic testing. These containers are divided into the following categories:

(i) Rigid Container,
(ii) Rigid container with absorbing (flexible) boundaries,
(iii) Rigid container with hinged end-walls,
(iv) Equivalent Shear Beam (ESB) container,
(v) Laminar container (passive type),
(vi) Laminar container (active type).

A list of the rigid containers employed to study soil dynamics problems is given Table 2.3. The rigid containers are often provided with rough bases to transmit the

base shear into the contained soil specimen. The sidewalls of the rigid container are smoothened in order to reduce the shear stresses.

Table 2.3. Rigid box assemblies reported in the literature.

Reference	L-W-H (mm)	H/L	Testing	Side-walls
Adalier and Elgamal (2002)	597-270-150	0.25	Centrifuge	Teflon
Withman and Lambe (1986)	500-565-190	0.38	Centrifuge	No-details
Ng *et al.*, (2004)	712-432-440	0.62	Centrifuge	Smooth plastic membrane
Norton (2008)	1500-400-1000	0.66	Shaking Table	Prespex and wood plates
Dash (2010)	450-240-400	0.90	Shaking Table	Prespex
Panah *et al.*, (2015)	1820-800-1230	0.67	Shaking Table	Plexiglas
Cappa *et al.*, (2017)	1758-909-537	0.30	Centrifuge	Plexiglas

Table 2.4. Rigid container with absorbing (flexible) boundaries in the literature.

Reference	L-W-H	H/L	Testing	Sidewalls	End-walls
Fishman *et al.*, (1995)	4270-910-1220	0.28	Shaking table	Tempered plate-glass	Hinged
Dash (2010)	450-240-400	0.88	Shaking table	Perspex	Sponge
Ha *et al.*, (2011)	1920-440-600	0.31	Shaking table	Acrylic plate	Sponge
Ling et al., (2012)	4000-2000-3000	0.75	Shaking table	Nylon sheet	EPS block
Lombardi *et al.*, (2015)	450-200-400	0.88	Shaking table	Plexiglas	Duxseal

In Equivalent Shear Beam container design, the boundaries of the container are designed to have no significant effect on the response of the model soil that is contained

by the ESB container. This is achieved by designing and constructing the container to have a similar shear stiffness and fundamental frequency to that of the contained soil. Once the similitude in shear stiffness and fundamental frequency of the container and the soil established, it could be assumed that there is no decoupling between the box and the soil. This is a state where the response of the container has no bearing on the response of the soil.

Since the shear stiffness of the soils are strain dependent, the similitude of stiffness and fundamental frequency between the container and the soil cannot be accommodated through all strain ranges. Zeng and Schofield (1996) explain the boundary conditions criterion that is to be met by the ESB container as follows:

(i) The boundary must have the same dynamic stiffness as the adjacent soil to minimize energy reflection in the form of pressure waves.
(ii) The boundary must have the same friction as the adjacent soil to sustain complementary shear stresses.
(iii) The sidewalls should be frictionless to have plane strain condition.

Two main methods of ESB box design are followed. In the first design method (Zeng and Schofield, 1996) the stiffness compatibility between the box and the soil is maintained in a limited stiffness range. The second method is to arrange the stiffness of the container to be lower than that of the soil at lower strain levels. As for higher strain levels (0.01 to 1% strain range), the stiffness of the box and the soil are coupled (Dar, 1993). Thusly the soil does not oppose the free-field behavior of the soil at lower strain ranges and at high strain ranges the box and the soil are at a similar stiffness level which means the presence of the boundaries have minimal effect on the soil response. A list of the ESB containers found in the literature is given in Table 2.5.

Table 2.5. Equivalent shear beam containers reported in the literature.

Reference	L-W-H	H/L	Shaking	Shape
Dar (1993)	2000-750-1750	0.90	1-D	Rectangular
Fishman *et al.*, (1995)	1200-550-800	0.66	1-D	Rectangular
Crewe *et al.*, (1995)	4270-910-1220	0.28	1-D	Rectangular
Zheng and Schofield (1996)	4800-1000-1200	0.25	1-D	Rectangular
Madabushi *et al.*, (1998)	560-250-226	0.40	1-D	Rectangular
Carvalho *et al.*, (2010)	800-350-600	0.76	1-D	Rectangular

A soil layer under a level ground surface is usually in a Ko condition, while, during an earthquake, the soil at different depths may move differently in the horizontal plane following the upward shear wave propagation. To provide such flexible but unyielding side boundaries as in the field, laminar simple shear boxes composed of layers of frames are commonly used in the tests. For horizontal one-dimensional earthquake shaking, every layer of the frames should be able to move freely in every direction in a horizontal (X-Y) plane following the movement of the soil in the container (Ueng, 2010).

According to Whitman and Lambe (1986), a laminar box aimed at simulating the free-field (shear beam) conditions that the soil experiences during vertical wave propagation should have the following properties:

(i) Individual laminates of the laminar box should ideally be massless,
(ii) Laminate layers should behave as a perfectly flexible shear beam and the boundaries of the laminates should be unyielding,
(iii) The design should allow for the dissipation of energy,
(iv) The box should possess the necessary friction with the soil at the base to be able to transmit the shear waves and the confining walls need to provide vertical strength so that complimentary shear stresses can develop.

Table 2.6. Summary of laminar box designs in the literature

Reference	L-W-H	H/L	Shaking	Shape	Descriptiona
Van Laak *et al.* (1994)	457-254-254	0.55	N-G	Rectangle	1, 4, 7
Gibson (1997)	900-350-470	0.52	1-G	Rectangle	1, 4, 7
Meymand (1998)	2280-2130 (D-H)	0.93	1-G	Circular	3, 4, 7
Shen *et al.* (1998)	584-500 (D-H)	0.85	N-G	12-sided	1, 4, 7
Takahashi *et al.* (2001)	450-200-325	0.72	N-G	Rectangle	1, 4, 6
Prasad *et al.* (2004)	1000-500-1000	1.00	1-G	Rectangle	1, 4, 7
Pamuk *et al.* (2007)	710-355-355	0.50	N-G	Rectangle	1, 4, 7
Turan *et al.* (2009)	900-450-807	0.89	1-G	Rectangle	1, 5, 7
Ueng and Chen (2010)	1888-1888-1520	0.08	1-G	Rectangle	2, 4, 7
Araei and Towhata (2014)	1000-500-1000	1.00	1-G	Rectangle	1, 4, 7
Guoxing *et al.* (2015)	3500-2000-1700	0.48	1-G	Rectangle	1, 4, 7
Wang *et al.* (2015)	3500-2000-1700	0.48	1-G	Rectangle	1, 4, 7
Latha and Santhanakumar (2015)	700-500-600	0.85	1-G	Rectangle	1, 4, 7
Dihoru *et al.* (2016)	1200-500-800	0.66	1-G	Rectangle	1, 4, 7
Zhang *et al.* (2016)	500-285-310	0.62	N-G	Rectangle	1, 4, 7

Note: 1. A stack of laminae separated by bearings; 2. Laminae supported by a frame and move independently; 3. Container hanging on the top lamina supported by a frame; 4. Entire container placed on shaking table; 5. Container partially placed on shaking table; 6. Active; 7. Passive.

3. MATERIALS

3.1. Clay

In order to mimic the behavior of a soft clay bed in laboratory conditions, commercially available kaolinite clay is used. The kaolinite is purchased from Camiş Madencilik who mines the kaolinite from a mine located in Bozüyük region in Bilecik, Turkey. The chemical composition of the kaolinite used is given in Table 3.1. The kaolinite clay is delivered in "big bags" which typically contain 750 kg of powdered kaolinite clay. The particle size of the powdered kaolinite is smaller than 100 microns.

Table 3.1. Chemical composition of the kaolinite clay.

Composition	SiO_2	$Al2O_3$	$Fe2O_3$	CaO	MgO	Na_2O	K_2O	Cr_2O_3	SO_3
Percentage (%)	73.4	18.5	0.4	CaO+MgO=0.5		Na_2+K2O=0.2		0.03	0.4

The Atterberg Limit tests and other relevant geotechnical index tests are run at Karl Terzaghi Soil Mechanics Laboratory at Bogazici University. The specific gravity tests conducted on the kaolinite revealed that the G_s value of the clay was 2.62. The plastic and liquid limits of the kaolinite were 26 and 49%, respectively.

In the early laboratory investigations phase of this study, a suitable water content for the kaolinite clay was tried to be found. Ideally, the clay slurry had to be both viscous enough not to clog the pipes during clay slurry infill to the experimental setup and it had to have minimum amount of water so that the settlements necessary to form the clay bed or in other words the water that should be expelled would be minimized. In order to investigate the suitable water content, the minimum water content to fulfill the viscosity criteria was selected by several trials of visual inspection of clay slurry running through the pipes that will feed the experimental setup. Second criterion was that clay would have adequate undrained shear strength and workability upon completion of consolidation. A water content of 75% was selected for the clay slurry because (i) the water content was high enough to avoid lumps occurring inside the

slurry, (ii) the resulting slurry was viscous enough to flow into the experimental setup by gravity, (iii) the settlements necessitated to achieve a clay bed of undrained shear strength less than 15 kPa was within reasonable limits. Similar choice of water content for clay slurry has been reported by many studies (e.g., Murugesan and Rajagopal, 2010; Black *et al.*, 2011; Frikha *et al.*, 2013; Miranda *et al.*, 2017).

By using a clay slurry of 75% water content, a parametric laboratory investigation was made for various overburden pressures using small scale cylindrical consolidation molds with a diameter of 5 cm in order to find out the unconfined compressive stresses the samples were able to bear. The molds were designed to yield samples with a height/diameter ratio of roughly 2 so that upon completion of consolidation the samples were tested for their unconfined compressive strength. Water content of the samples were also determined. Figure 3.1 illustrates gives the resulting unconfined compressive strengths of the samples which are consolidated under various overburden pressures. Figure 3.2 gives the unconfined compressive strengths of these samples as a function of water content.

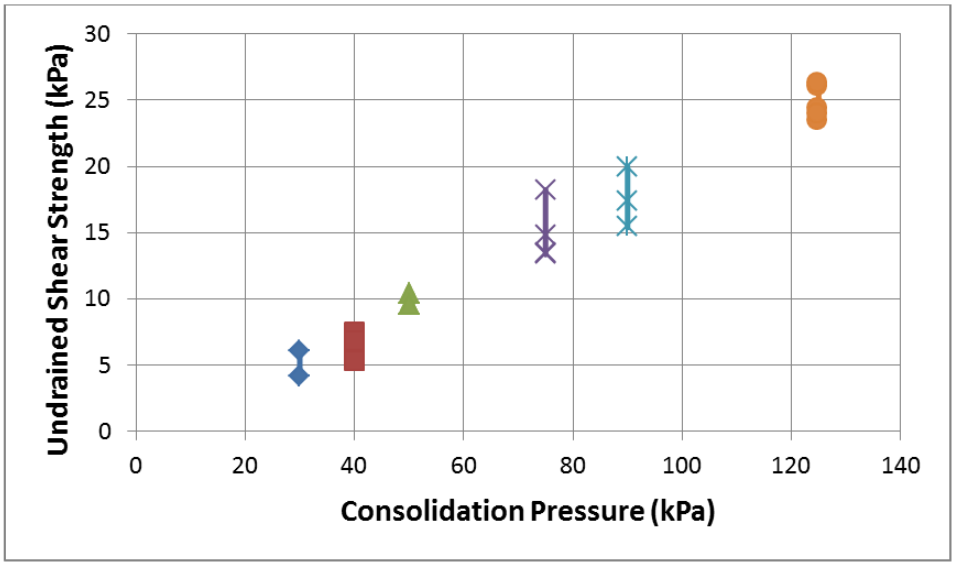

Figure 3.1. Unconfined compressive strengths of clay specimens for various consolidation pressures.

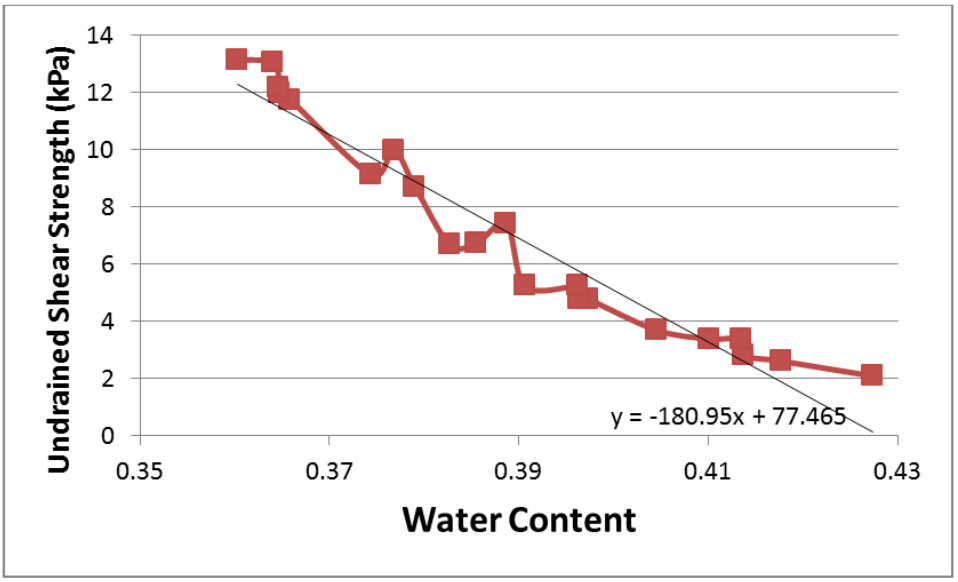

Figure 3.2. Variation of unconfined compressive strength by the water content of the clay sample.

3.2. Sand and Gravel

Granular material has been used while forming the GECs and OSCs and also in preparing bearing layers and model embankment fills. The sand used was also a poorly graded (SP according to Unified Soil Classification System, USCS) material with D_{10}, D_{30}, and D_{60} values of 0.47, 1.1, and 2 mm respectively. The gravel used was a poorly graded gravel (GP according to Unified Soil Classification System, USCS) was used with D_{10}, D_{30}, and D_{60} values of 5, 6.1, and 7.9 mm respectively. The gradation curve pertaining to the material is given in Figure 3.3. The internal angle of friction for the gravel was 44 degrees. The maximum and minimum void ratio of the gravel was 0.64 and 0.33, respectively. The engineering properties of the granular material used is given in Figure 3.3. The strength parameters of the granular material were determined in triaxial compression tests with cell pressures varying from 20 to 200 kPa. The triaxial apparatus used had a diameter of 100 mm and an average sample height of 200 mm.

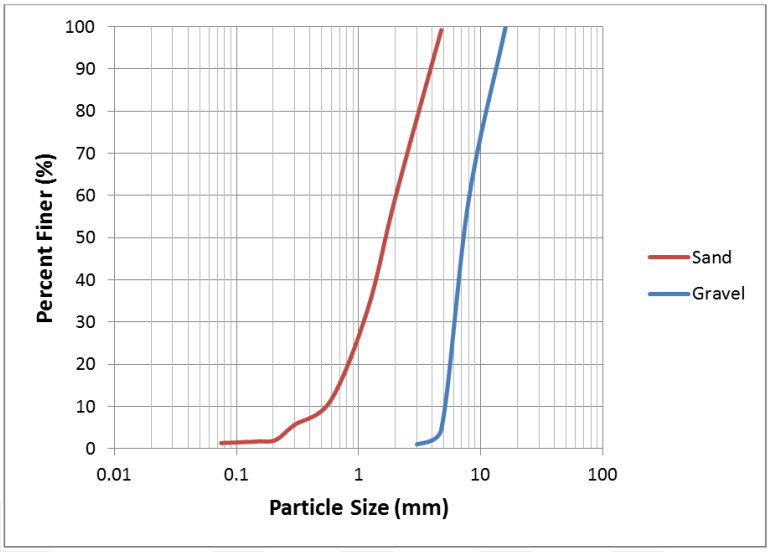

Figure 3.3. Grain size distribution curves pertaining to granular material used.

Table 3.2. Engineering properties of the sand and the gravel used

Property	D_{10} [mm]	D_{30} [mm]	D_{60} [mm]	c_u	e_{max}	e_{min}	ϕ_o
Sand	0.47	1.1	2	4.25	0.62	0.3	37
Gravel	5	6.1	7.9	1.58	0.94	0.43	44

3.3. Geosynthetic Reinforcements

3.3.1. General Properties

Within the scope of this study, three different geotextiles were used. The first geotextile is a commercially available spun-bonded non-woven geotextile namely, Tencate Polyfelt TS 10 (designated as GT1). The second and third geotextiles are Sefitec PP 50 and Stabilenka 100 which shall henceforth be designated as GT2 and GT3, respectively. The tensile strength tests of these samples are conducted on 200 mm wide samples in accordance with DIN EN ISO 10319 and relevant data is tabulated in Table 3.3. GT2 and GT3 have been provided by Huesker Synthetic GmbH in cylindrical form and GT1 is locally tailored with a longitudinal seam to achieve a cylindrical shape. All of the encasements had a diameter of 168 mm. The diameters of the model columns were selected so that the model columns will be representative of a field prototype

with a diameter of 400 mm, equating the scale ratio roughly to 1:2.5. Thus, the scaling factor (model/prototype) for the encasement tensile modulus has to be 6.25. Since the model reinforcement moduli (stiffnesses) for GT2 and GT3 are 400 and 1000 kN/m, the prototype equivalent of GT2 and GT3 are 2500 and 6000 kN/m. These values of reinforcement modulus fall well with the field practice.

GT1 is a non-woven geotextile with a very low tensile stiffness. GT1 served basically only as a bearing medium (carrier material) for the strain gauges rather than being a reinforcement. Gu *et al.* (2016) used a collar type sensor, namely, hoop displacement gauge for measurements of radial distortions of ordinary stone columns. In the absence of such equipment, a very low modulus geotextile was used to be able to observe ordinary stone columns' behavior under the action of seismic loads.

Table 3.3. Tensile stiffness parameters of the geotextiles used.

Strain	Tensile Force (kN/m)			Secant Modulus		
(%)	GT1	GT2	GT3	GT1	GT2	GT3
2	0.72	7.6	21.6	36	380	1050
3	0.9	12.2	31.5	30	400	1050
5	1.25	21	60	25	420	1200
10	1.8	44	115	18	440	1150

3.3.2. Calibration of Strain Measurements

Since GT1 is a low modulus material, the installation of strain rosettes by making use of an adhesive would introduce zones of high modulus. When loads are applied, these zones would not be strained as the virgin material would. The other geotextiles used namely, GT2 and GT3, have relatively higher stiffnesses than that of GT1 but the strain measurements coming from the encasements should be validated and checked under controlled conditions.

These concerns have led to development of an experimental setup where the encasements are strained at a strain rate of 2 mm/min. Although the encasements

provided by Huesker are professionally sewn, to ensure the tensile strength properties of the materials are not affected by stitching, the tests are run on stitched specimens. A strain rosette is placed in the center of the tested specimens to gather the strain data that the individual strain gauges yield under tension. The strain rosettes used have concentrically positioned strain gauges oriented at 0/45/90 degrees. Thusly, the extension of the material or the vertically oriented strain and accompanying lateral or horizontal strain can be measured. The skew strain which is inclined 45o with the horizontal can also be recorded. The strain rosettes were attached to the center of the specimens in the exact manner that was used for the reinforcements.

The strain measurements taken from the strain rosette was compared against the actual strain. Here the term actual strain refers to the strain measured by making use of a laser displacement sensor. The initial sample width is divided to the amount of displacement of the top portion of the testing assembly to yield actual strain. Once the measured and actual strain data is gathered a transfer function was developed for each geotextile to correctly interpret the measured strain values. The main assumption made here is that it is assumed that the strain is distributed over the width of the sample equally at all strain levels. This assumption may not be true for the increased strain levels where significant roping effect occurs on the tested geotextile. Pronounced roping effect towards the end of the wide width tensile tests was observed for GT1.

An MTS load frame powered by a servo-hydraulic loading unit was used for the tests. The load cell that is embedded to the MTS load frame was not used as the said load cell has a capacity of 10 tons which may not provide the necessary precision in low force amplitudes. The tensile force acting on the geotextile samples throughout the course of the tests were measured by a 500 kg capacity load cell. The load cell was attached to the MTS load frame by making use of a specially machined screw bit. The samples were positioned between two steel rods passing through the sample. Thusly the stitched material strength parameters were put to test. Figure 10 illustrates the test setup for all geotextiles used in this study.

4. EXPERIMENTAL METHODOLOGY

4.1. Rigid Box

4.1.1. Properties of the Rigid Box

The rigid box assembly that was used for the initial 1g shaking table tests had been used by various researchers at Bogazici University. The most recent dissertation that made use of the box is Kilic (2014). A photograph of the rigid box is shown inFigure 4.1. Originally, the rigid box was used for running 1g shaking table tests on scaled geosynthetic reinforced walls and therefore one of its side walls facing the direction of shaking was intentionally left empty. The inwards and outwards accelerations were thusly allowed and displacements of the facing blocks of the reduced scale model walls were monitored through the opening. For the present study the rigid box was modified and the opening in the side wall depicted in Figure 4.1 was closed off. The modified rigid box had a height of 2100 mm, depth and width of 2500 and 520 mm, respectively. Four equally spaced pneumatic pistons with inner diameters and stroke limits of 160 mm were placed on top of the rigid box. The force outputs from the pneumatic pistons were used for consolidating the clay slurry inside the box. The pneumatic pistons were also made use of for running stress controlled column load tests on the GECs and OSCs. The columns' centers were vertically aligned with the centers of the driving rods coming out of the pneumatic pistons. Steel plates (515 mm wide and 545 mm long) with perforations were attached to the ends of the driving rods extending from the pneumatic pistons and these plates were used to apply the surcharge loads during consolidation and shaking table tests. Figure 4.2 depicts some modified features of the rigid box assembly such as the added pneumatic pistons on the top of the box and the perforated surcharge plates.

Figure 4.1. The rigid box assembly used by Kilic (2014).

Figure 4.2. a) Top view of the pneumatic pistons, b) surcharge plates and their connection to piston rods, c) surcharge plates from bottom.

4.1.2. Sample Preparation Technique for the Rigid Box

The sample preparation commenced with placing a 250 mm thick compacted sand layer at the base of the rigid box. The sand used was identical to that of the column infill material used in this study. The side walls of the rigid box that were perpendicular to the direction of shaking were greased and covered with nylon sheets. The side walls were greased to reduce the friction between the rigid box boundaries and the model constituents during shaking. The greased surfaces were covered with nylon in order to prevent the clogging of the geotextile. It was important not to impair the transmissivity property of the geotextile as the material aided in consolidation by allowing the flow

of excess water through its thickness. The geotextile sack was tailored to fit the inner dimensions of 2000 x 520 x 2200 mm (height, width, and depth) as a rectangular prism and it was placed inside the rigid box assembly, atop the compacted sand layer. 150 mm thick EPS blocks with a height of 2000 mm were placed at both ends of the rigid box facing the direction of shaking. The reason for placing the EPS blocks was to prevent the seismic waves from traveling in a recurrent manner throughout the model. Ling *et al.* (2012) placed EPS blocks to minimize wave refraction from physical model boundaries. Lombardi *et al.* (2015) has also demonstrated that including EPS blocks in the boundaries of a rigid box created absorbing boundar

Clay slurry was prepared in 0.5 m3 drums. The drums were elevated by virtue of an indoor crane and the total weight of the drum was monitored with a crane scale accurate to 0.1 kg. The drums were lifted and the flow of the clay slurry was initiated by gravity. A photograph pertaining to the slurry infill operation is given in Figure 4.3. The clay slurry is placed in a non-woven geotextile (500g/m2) wrap and the top portion of the geotextile is folded onto itself and sealed by silicone in order to prevent clay slurry from leaking out in the early stages of consolidation. The overburden pressure was applied on top of the geotextile sack by the steel overburden plates. The clay slurry was consolidated to an overburden pressure of 25 kPa. The EPS blocks on the model boundaries can be seen in Figure 4.3.

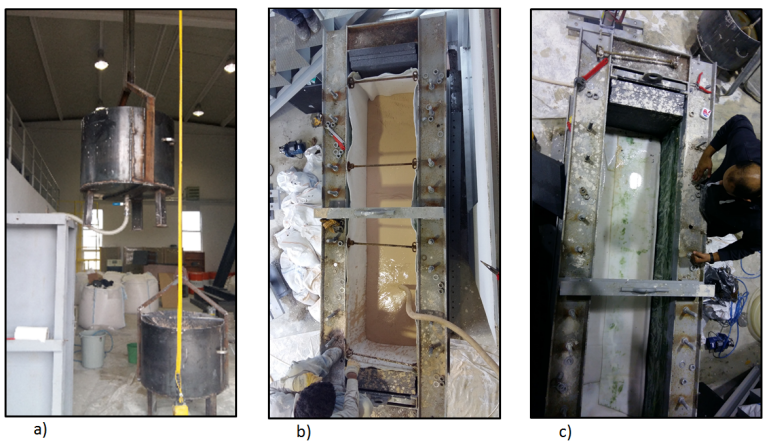

Figure 4.3. a) Clay slurry infill from the drum, b) Top view of clay slurry infill process, c) consolidated clay bed.

Once the consolidation of the clay slurry was completed, model OSCs and GECs were installed inside the soft clay bed by a column driving unit that was specially put together for the rigid box experiments. The column driving unit made use of a one-meter-stroke pneumatic piston for pushing a thin-walled casing pipe into the clay bed. The inner diameter of the casing pipe is 168 mm with its wall thickness being 1.5 mm. The column driving unit has an internal reaction frame that is made up of four 22 mm diameter grooved steel bars (2 meters long) and two laser cut steel plates. In the early design of the column driving unit, no provisions for a guide collar to ensure the verticality of the columns was made. The verticality of the columns were ensured by leveling the casing pipe with a bubble level. Figure 4.4 illustrates the column driving unit both by itself and during column driving process. The stoke limit of the pneumatic piston is exhausted after driving the casing pipe for a meter. Once this limit is reached, the direction of the air supply to the pneumatic piston is reversed and the piston rod is retracted back into the piston. Additional pieces are placed between the casing pipe head and the piston drive rod to penetrate the casing pipe to the desired depth within the clay bed.

Figure 4.4. Casing pipe driving unit.

Within the scope of the present study, both floating and end bearing columns were produced. Figure 4.5 depicts the rigid box assembly mounted on the shaking table and the see-through image of the rigid box. Also depicted in Figure 4.5 are the dimensions of the rigid box assembly and the typical disposition of floating and end-bearing columns in a model test.

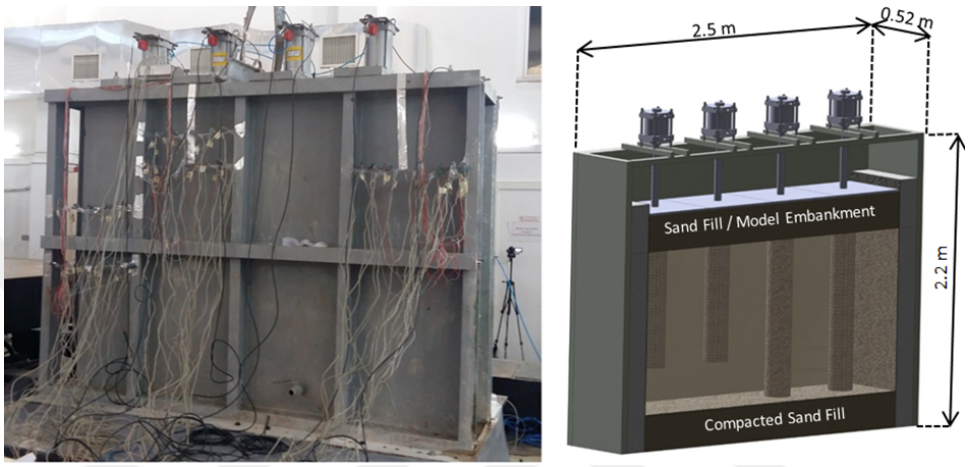

Figure 4.5. Instrumentation and see-through image of the rigid box assembly.

4.2. Laminar Box

The laminar box is essentially composed of 16 layers of individually supported laminates. Each laminate level is made up of aluminum sigma profiles with a height and width of 100 and 50 mm, respectively. A vertical clearance of 2 mm is provided between each laminate level in order to maintain independent movement of the laminates. A 300 mm deep rigid base cavity is provided at the base of the laminar box to accommodate a firm bearing stratum for the granular columns. The rigid base cavity also aided in minimizing the impedance contrast between materials which will be explained in detail in the subsequent sections of this study. With the rigid base cavity, laminates' thickness, and the vertical gap between the laminates, the laminar box stands 1932 mm tall. The plan dimensions of the laminar box are 900 by 900 mm.

4.2.1. Properties of the Laminar Box

The laminar box was designed with the intention of mimicking the site conditions that the soft clay soil undergoes during seismic excitations. The moving parts of the box are designed so that there will be minimum resistance to the passage of the shear wave through the housed soil specimen. The boundaries of the laminar box were designed to be unyielding under the action of static and dynamic loads. The static loads are the lateral component of the self-weight of the soil and the added overburden pressure that is induced during consolidation of the clay slurry or during the shake table tests with maintained over burden pressure. The dynamic loads are the loads caused by the application of accelerations to the soil body by virtue of the shaking table. The boundaries are made up of aluminum sigma profiles with hollow space inside the profiles which reduces weight. The aluminum sigma profiles have continuous hollow spaces in their length-wise direction. This very property of the aluminum profiles has inspired the design of the laminate levels which constitute the overall design of the laminar box.

During the conceptual design process of the laminar box, many available laminar box designs were studied and shortcomings of these designs were identified. "Stack-of-laminates separated or supported by bearings" design methodology is frequently encountered in the literature and majority of the laminar box designs have adopted this method due to its simplicity. The most obvious shortcoming of laminar boxes that rely of stack-of-laminates type of design is the increasing vertical load on the laminate bearings towards the bottom of the laminar box. Since each laminate vertically supports the laminates above itself, the cumulative increase in vertical stress increases the friction at bearing level which adversely affects the free lateral movement of the lower laminates. There is often uneven amount of friction occurring at different levels of the laminates which results in twisting or rocking of the laminar box, as well. Cantilever deformations occurring in stack of laminates design has also been reported in the literature (Hushmand *et al.*, 1988). Lastly, toppling of the laminar box due to eccentricity of the shifted center of mass of the retained soil is a serious concern. Bethapudi (2008) have used tension cables to arrest the excessive lateral motion of the laminates to avoid toppling of the laminar box. A view of the tension cables acting in

vertical and horizontal directions used by Bethapudi (2008) are illustrated in Figure 4.6. In the design of the present laminar box, the laminates bounding the soil specimen are continuously supported which ensures that the laminar box or the individual laminates do not undergo toppling.

a) Vertical Cables (b) Horizontal cables

Figure 4.6. Tension cables used by Bethapudi (2008) to prevent toppling of the laminar box.

The design of the laminar box was conceptualized to mitigate the above mentioned problems associated with the use of the laminar box. The problem associated with the cumulative load effects of on a given laminate by the overlaying laminates is solved by devising a way to individually support each laminate. The laminates are designed so that two smooth steel linear guide rods pass through the hollow space in the aluminum sigma profiles, which are facing the direction of shaking in their lengthwise direction, constituting each lamina. The laminates are connected to the linear guide rods with four Teflon bearings at the corners. The use of Teflon bearings ensured minimum friction with minimal degradation of friction properties over time. The linear guide rods fixed to supporting columns and are fitted with 10 mm thick rubber stoppers in each end to mitigate the effects of banging of the laminates to the columns of the laminar box. The clear space for each laminate to move was 220 mm which equates to a shear strain of 14% throughout the height of the laminar box. During the course of the experiments, under various dynamic excitations, the lateral deformation capacity of the laminates were rarely exhausted.

Figure 4.7 depicts the general features of the laminar box. At the bottom portion of the laminar box, there is a rigid base cavity. The base cavity is designed to be stationary under the action of the dynamic loads. It is included in the design to create a level filled with gravel material. The motive behind including this layer is the similitude in the impedance factors of gravel and clay. This layer enables the shear waves generated by the shaking table to travel through an earth material into the soft soil bed. The high impedance contrast between the steel and weak clay is thusly avoided. Other than providing a layer which mitigates the effects of high impedance contrast, the base cavity also provides a firm layer for the end bearing ordinary stone columns and geosynthetic encased stone columns that are to be installed in the soft clay which will be housed in the laminar box. Figure 16 also depicts 16 layers of individually supported laminates and the support columns that the linear guide rods are fixed onto.

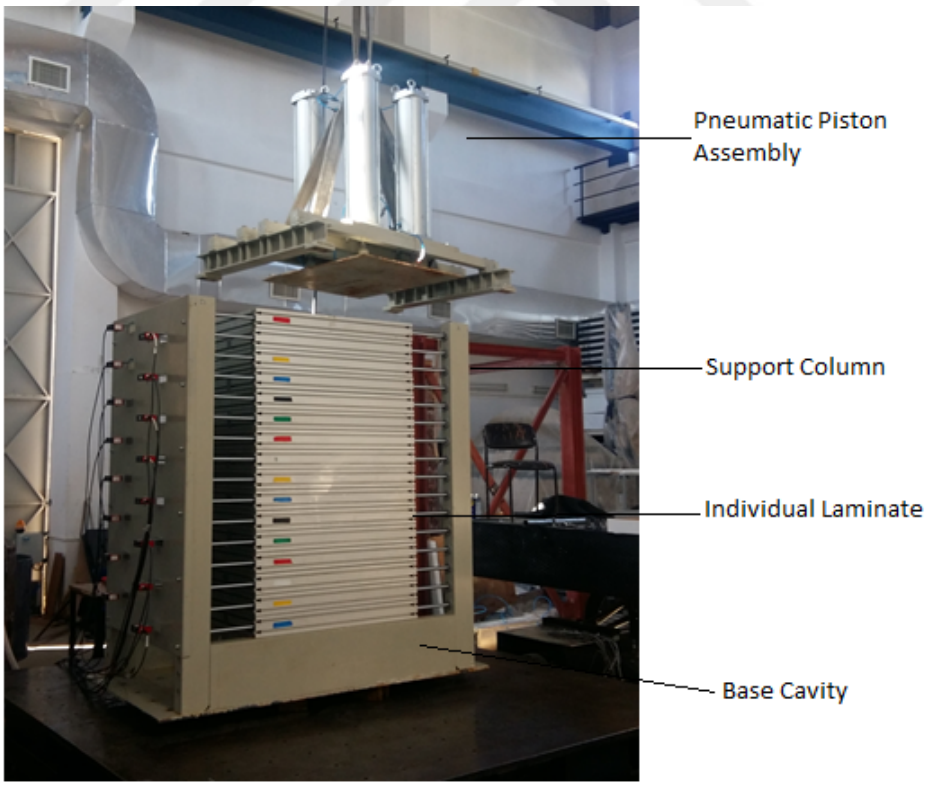

Figure 4.7. General features of the laminar box.

Figure 4.8 illustrates two of the surcharge plates that are connected to pneumatic pistons. 445 by 445 mm surcharge plates are used to consolidate the clay slurry inside

the laminar box. The plan dimensions (inner clear dimensions) of the laminar box is 900 by 900 mm. The surcharge plates are trimmed by 5 mm in order to avoid overlap of the plates during consolidation. The gap between the plates also aid in dissipation of the pore water during consolidation. The surcharge plates driven by pneumatic pistons with a 800 mm stroke capacity. The high stroke capacity of the pistons enable the consolidation of the clay slurry at one go without addition of extra drive rods. The inner diameters of the pneumatic pistons are 160 mm. This means that the surcharge pressure derived at the plate level per 100 kPa of air pressure is about 10 kPa. The pneumatic pistons are connected to an air supply unit. The air supply to the pneumatic pistons is controlled with a precision air regulator with a regulation accuracy of 0.05%. The regulated air is allowed to pass through an air pressure sensor which is connected to a single-channel data display unit. The regulated air pressure value is adjusted and monitored by making use of this unit throughout the consolidation phase. Figure 4.9 illustrates the entirety of the surcharge unit suspended in the air by making use of an indoor crane.

Figure 4.8. Two of the surcharge plates.

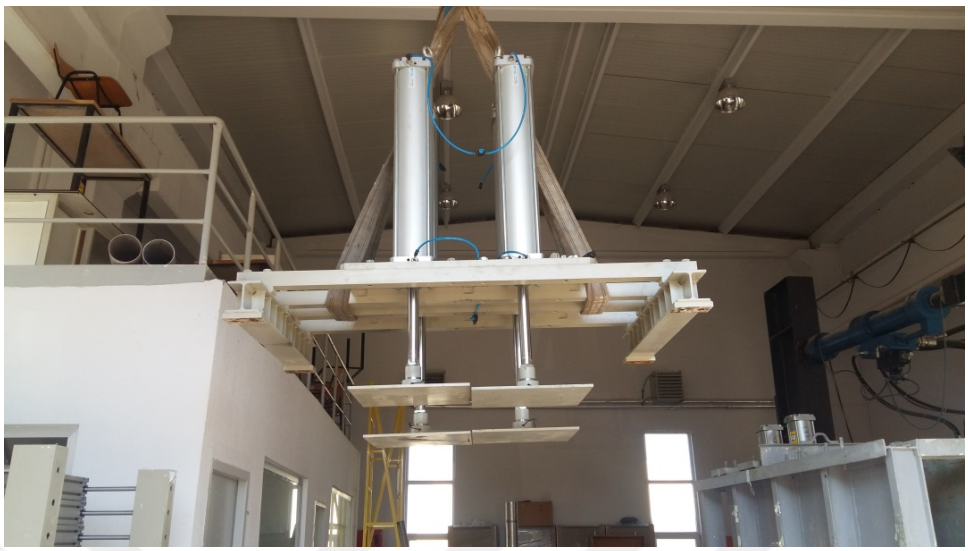

Figure 4.9. The surcharge unit suspended in the air.

Figure 4.10 illustrates the components of the column driving unit. The column driving unit is used to push a thin walled tube (casing pipe) with an inner diameter of 136 mm in to the soft clay bed. The force required for driving the casing pipe into the clay bed is provided by a 1 meter-stroke pneumatic piston with an inner piston diameter of 250 mm. The casing pipe is driven through a guide collar of 100 mm thickness to ensure the verticality of the resulting columns.

Figure 4.10. Components of the casing pipe driving unit.

4.2.2. Sensor Placement on the Laminar Box

In this section, only the sensors that are placed on the laminar box will be discussed. There are many of sensors placed on the GECs and inside the model soil which are beyond the scope of this section. The horizontal movements of the laminates are tracked by laser displacement sensors. The laser displacement sensors are deployed at two different vertical alignments. The reason for that is to increase the distance between laser displacement sensors that are targeted to adjacent laminate layers. The laser displacement sensors rely on the reflected laser beam from a target to compute the distance of the target. If the sensors are deployed too close to each other, the sensor could receive the reflected laser beam from the neighboring laminate and reliability of the distance measurements is compromised. LEUZE, the producer of the laser displacement sensors used in this study, recommends that the sensor spacing should be greater than 150 mm. The sensor spacing with the current configuration is 200 mm. The laser displacement sensors are illustrated in Figure 4.11a. In order to measure the acceleration response of each laminate, 16 accelerometers are attached on the laminates. The accelerometers are attached on the so called "backside" of the laminar box are illustrated in Figure 4.11b. An additional accelerometer is attached to the rigid base cavity portion of the laminar box to quantify the input accelerations given to the assembly. Figure 4.12 gives a sketch of a typical experimental setup where GECs are tested. The disposition of the columns in plan is also presented in Figure 4.12. Additions to the sensors depicted in Figure 4.12 are pore water pressure gauges and soil pressure gauges which are not utilized in every test. Implementation of the strain rosettes will be discussed in the subsequent sections.

Figure 4.11. Laser displacement sensors and accelerometers attached on the laminar box.

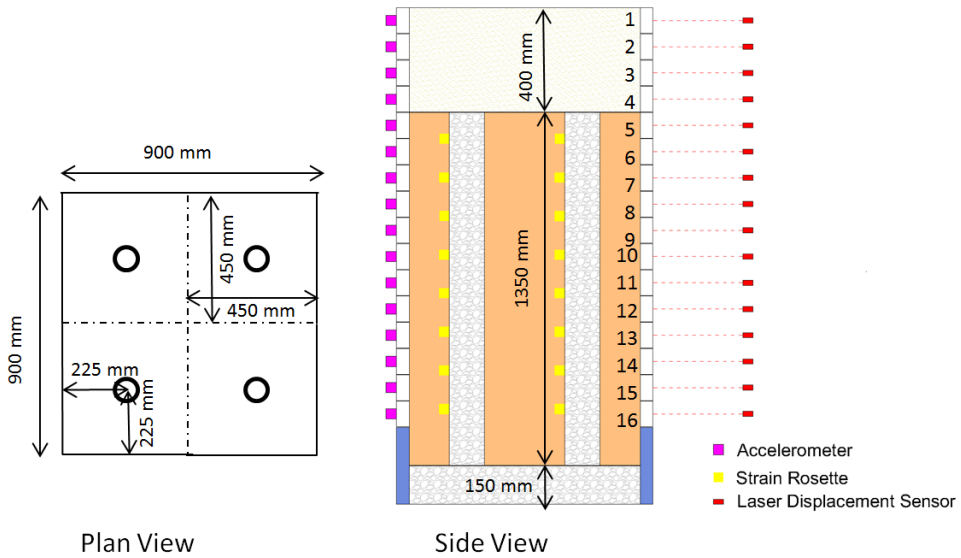

Figure 4.12. Disposition of sensors in a test where GECs are tested.

4.3. Sample Preparation Technique for the Laminar Box

4.3.1. Clay Slurry Preparation, Placement, and Consolidation

Meymand (1998) used a specially constructed continuous progressive cavity mixer / pump to mix and pump the clay slurry into the testing assembly. In the present study, a simpler sample preparation and placement technique is adopted. Large stainless steel drums are connected to a crane scale and suspended from an indoor crane. For every batch of clay slurry 150 kg of tap water is filled inside the drums. The powder form kaolinite clay is gradually added and continuously mixed with a power mixer tool until the added amount of kaolinite is 200 kg. The clay slurry is thoroughly mixed and aged until no lumps were present. The drums are fitted with 50 mm diameter hose outlets at the base and once the desired homogeneity of the clay slurry is reached, the drums are raised to achieve an elevation head. The valve on the 50 mm outlet is opened and the clay slurry is hosed into the laminar box by gravitational flow.

A double lining detail is realized inside the laminar box. The first layer of lining is consisted of a thin singular plastic sheet which is folded to make the interior of the laminar box watertight. Since a singular sheet of plastic is used without any additions or overlaps, leakage of the interstitial water is prevented. The second lining level is a nonwoven geotextile layer with a mass per unit area value of 500 g/m^2. The geotextile lining is tailored in a prismatic shape to fit the inner clearances and height of the laminar box. A 500 mm overhang is allowed on the geotextile lining which is used to envelope the clay slurry retained inside the liner. The overhang is glued with a silicon based adhesive to prevent the leakage of clay slurry under the surcharge load applied by the steel loading plates. Since the geotextile liner allowed drainage of the excess pore water during consolidation, the drainage path reduced to 450 mm for the mid portions of the clay bed. Reduced drainage path allowed for shorter consolidation time.

The rigid base cavity of the laminar box was filled with the above specified gravel to a height of 150 mm and compacted. The gravel layer was saturated with tap water. The saturation was done superficially; water was added on top of the gravel layer until

the water level became flush with the top of the gravel layer. In order to prevent the puncture of the plastic sheet liner, a 900 x 900 mm non-woven geotextile was placed on the gravel to act as a cushion layer between the gravel and the plastic liner material.

The outer liner comprised of plastic sheet is tensioned in order to avoid the downdrag of the liner with the surcharge plates. During the course of the consolidation, it was observed that the clay bed was inundated under water and no visible sign of leakage of the excess interstitial water was observed. The 800 mm stroke capacity of the pneumatic pistons was sufficient to fully consolidate the clay bed under 25 kPa surcharge load. With half the rigid inclusion filled with clay slurry and clay slurry level flush with the top lamina level, the clay slurry was initially filled to a height of about 1750 mm. The consolidation settlement in the clay bed was about 400 mm. The depth of the resulting clay bed was approximately 1350 mm with 150 mm of the clay bed inside the rigid base cavity.

4.3.2. Column Installation

Once the consolidation of the clay was completed, OSCs and GECs were installed. The interstitial water accumulated on top of the surcharge plates overlying the clay bed was syphoned out of the laminar box in order not to introduce softening of the clay during column installation process. The both the OSCs and GECs were installed by displacement method. A thin-walled stainless steel casing pipe with an inner diameter of 136 mm was closed off with a flat shoe and driven into the weak clay bed. The bottom end of the casing pipe is closed off with a flat shoe to ensure that the clay does not seep into the hollow space that is provided for GECs and OSCs. The flat shoe was not fixed to the edge of the casing pipe. The link between the flat shoe and the edge of the casing pipe worked in compression. During the casing driving process the flat shoe was pushed down. Once the casing pipe is driven to the desired depth, the vertical cavity created by the driving of the casing is checked to make sure that the volume is devoid of any clay. For this purpose, a flash light is lowered inside the driven casing pipe. Figure 4.13 illustrates such a photograph taken inside the casing pipe driven to the soft clay bed.

Four columns were driven with their centers concentric with the geometrical centers' of the settlement plates and surcharge pistons. The area placement ratio of columns to soft soil is 7%.

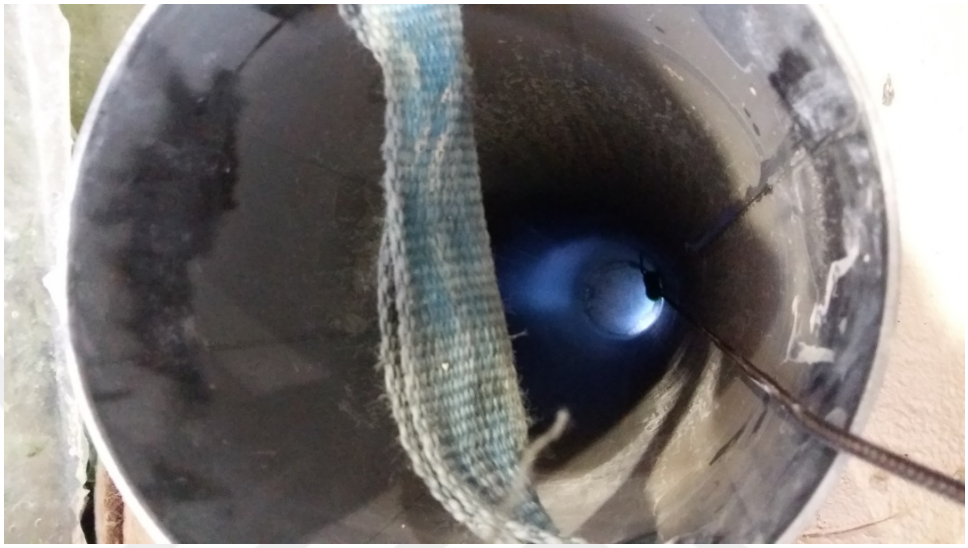

Figure 4.13. Photograph depicting the inside of the driven casing pipe illumined with a suspended torch.

The columns were infilled to a height of about 1350 mm with 7 consecutive steps of gravel addition and subsequent compaction. The casing pipe was gradually retracted as the column placement commenced with care taken not to expose the unfilled portion to surrounding clay. Once the casing pipe was retracted, the flat shoe remained at the base of the installed column. The placement procedure of GECs differed slightly than that of the OSCs with the instrumented reinforcement placed before the infill of the gravel. During placement, it was made sure that the strain gauges faced the direction of shaking by adding a few hundred grams of gravel inside the geosynthetic reinforcement tubes which were closed off with circular caps made of geotextile material identical to the geotextile liner.

4.4. Calibration and Implementation of the Sensors and the Data Logger System

A multitude of sensors were utilized throughout the course of the experimental program and the data coming from these sensors had to be acquisitioned. The calibration of the sensors is an integral part of gathering reliable data from the physical tests. In this part of the forthcoming study, the calibration and implementation techniques used will be discussed. Novel methods of sensor calibration and implementation have been undertaken for the realization of the experiments. Lastly, an account of the multi-channel data logger that is put together for this study will be presented.

4.4.1. Calibration and Implementation of Strain Rosettes

The strain rosettes are instrumented in order to track the strains developing on the geosynthetic reinforcement under the action of the dynamic input motions. The watertight strain rosettes (TML, WFRA-6-11-5L) used in this study is produced by Tokyo Sokki Kenkyujo Co., LTD. The strain gauges are covered in an epoxy resin and it is anticipated that together with the strain gauge adhesive used (TML, CN-Y Adhesive) the area of strain gauge application on the geotextile will have a larger stiffness than that of the virgin material. Moreover, it was seen that each geotextile used had unique surface and bonding characteristics which led to devising of different strain rosette attachment procedures for each material.

A series of calibration tests under tensile forces were run on the geotextile encasements instrumented with strain gauges. Photographs depicting the calibration tests for all geotextiles used in this study are given in Figure 4.14. The geotextile specimens are instrumented with strain rosettes. The strain rosettes are attached on the calibration test specimens with the exact same manner as the model GECs. The specimens are tensioned by making use of an MTS load frame. Since the internal load cell on the MTS load frame has a capacity of 10 tons, a load cell with a 500 kgf capacity is attached on the testing apparatus. The samples were tensioned at a rate of 2 mm/min. Rather than going through the lengthily process of producing or purchasing purpose

built grabs, the outer construction of triaxial bulbs were modified to serve as grabs.

The vertical movement of the top portion of the test setup is recorded by virtue of a laser displacement sensor. Since the original dimensions of the sample is known, the measured distance can be converted to strain. The strain calculated from displacement readings is termed as the absolute strain. The strain value that is measured from the strain gauge is, on the other hand, termed as the measured strain. The objective of the calibration tests was to come up with a coefficient of conversion between the absolute and measured strain for each geotextile. It was anticipated the coefficient of conversion would be different for different geotextiles. The test revealed that a singular conversion factor would not effectively convert the measured strains to actual strains. The relationship between the absolute and measured strain was defined by transfer functions which were sensitive to the level of strain that the material experienced.

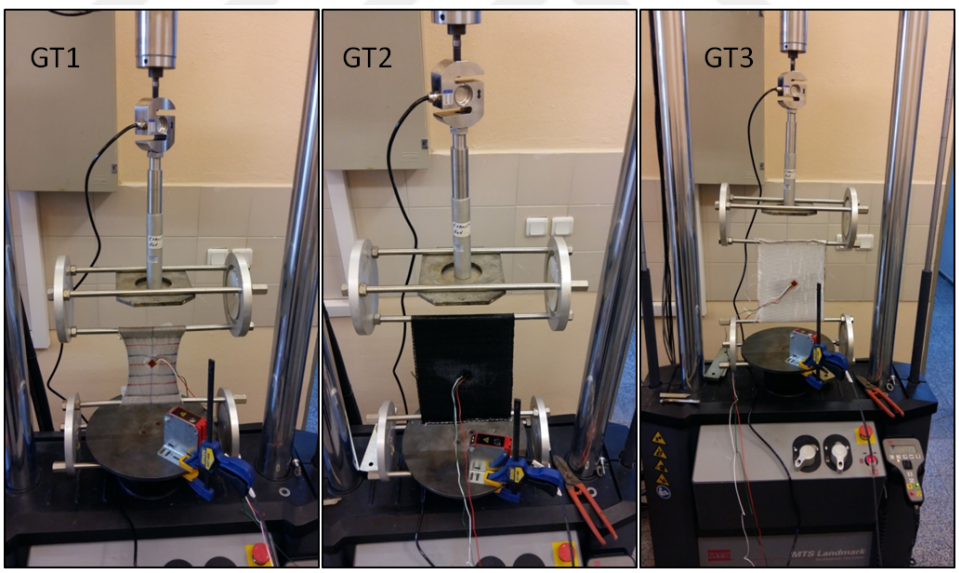

Figure 4.14. Strain gauge calibration test setups for the geotextiles used.

The transfer function for the vertical strain component of GT1 calibration test is presented in Figure 4.15. The ordinate axis in Figure 4.15 is the measured strain response from the strain gauge attached at the center of GT1. Two linear approximation lines of the actual strain (calculated by making use of the laser displacement readings) are adopted to fit the general trend of the data measured strain data. It is seen that the strain readings are grossly low in amplitude so the method of linear fitting was

done by dividing the actual strain reading by correction factors, k. In order to work out the actual strains, the correction factors are to be used in reverse in the mathematical sense (i.e. multiplication). Depending on the intensity of the strain the measured strain value is multiplied either by 55 or 110 with the threshold value being 0.0008. The complete strain data coming from the individual strain gauges oriented in vertical, horizontal, and skew directions pertaining to tensile loading of GT1 is presented in Figure 4.16. It is worth noting that the strain gauges used have a strain measurement capacity of 3.5%. The vertical strain measurement is thusly interrupted at a strain value of about 3.5%. Another noteworthy detail in Figure 4.16 is the development of compressive strains. It is common knowledge that geotextiles work in tension and not under compression. In Figure 4.15, the negative algebraic sign refers to tensile strains while positive sign refers to compressive strains. The horizontal strain reading reflects that the material is under compression. This is probably due to Poisson effects on the material. In Figure 4.14, it can readily be seen that the GT1 has significantly shortened in the horizontal direction. Therefore, with the visual inspection of the material supporting the measurements, it could be postulated that the geotextiles can be subjected to complementary compressive strains.

In Figure 4.17 it is seen that the dependence of the horizontal strains on the vertical strain amplitude for GT2 is significantly less than that of GT1. The probable cause of this is the difference in the production techniques of the materials. GT1 is a nonwoven spunbonded material. The fibers are interlocked in all direction of the materials matrix. GT2, however, is a woven geotextile. The fibers are woven at 90 degrees to each other and there is, if any, a very weak frictional interaction between orthogonally aligned sets of fibers. The introduction of the strain gauge adhesive partly connects the fibers oriented in vertical and horizontal directions and that explains the weak interaction between the vertical and horizontal strains. In Figure 4.17, it is seen that the amplitude of vertical and horizontal strains is almost one to one. Figure 4.18 depicts the transfer function for the vertical component of GT3. Figure 4.19 depicts the calibration test data for GT3 for all strain gauges. The plots of strain in Figure 4.19 are staggered due to many instances of fiber rupture that took place during testing.

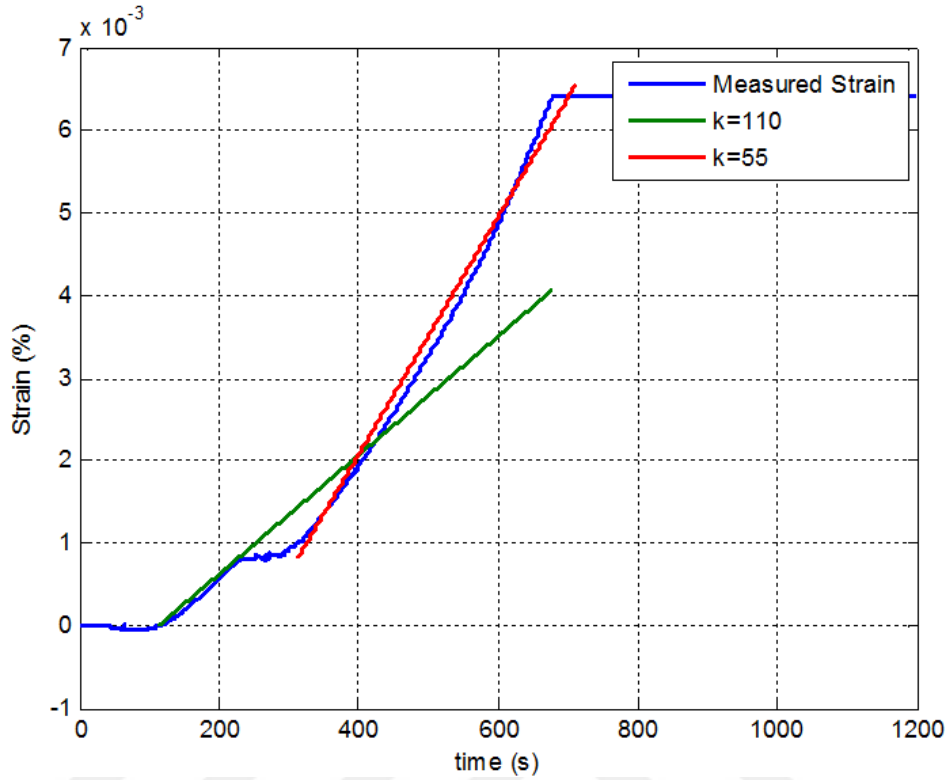

Figure 4.15. Transfer function for the vertical component of GT1.

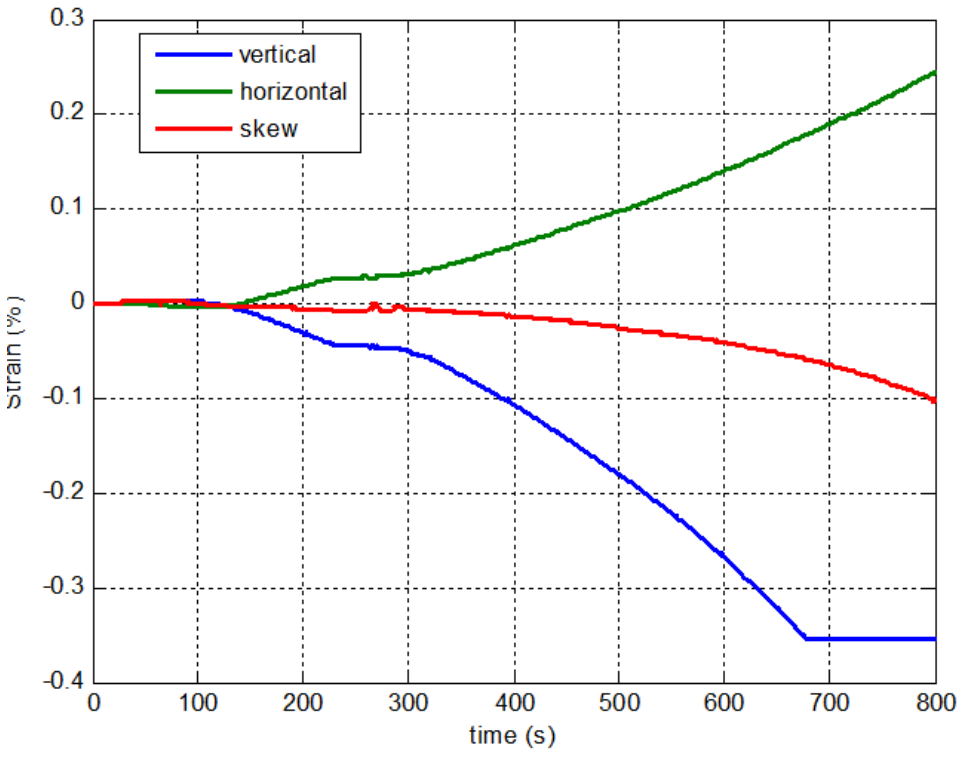

Figure 4.16. Strain values of GT1, transfer function applied.

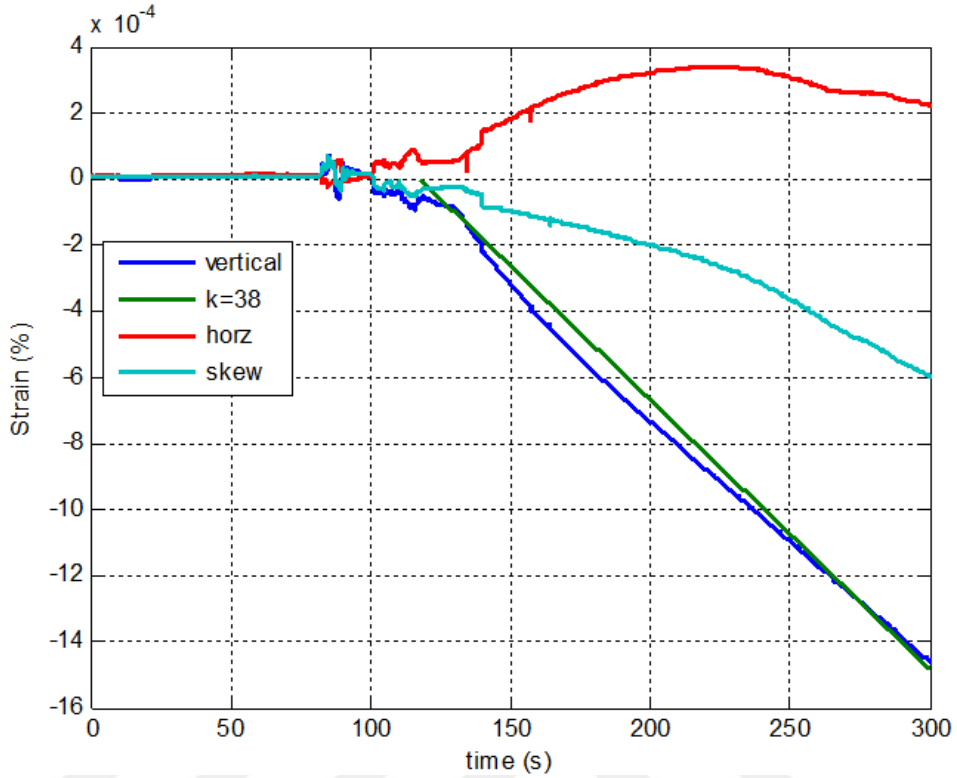

Figure 4.17. Measured strain values and fitted actual strain line for GT2.

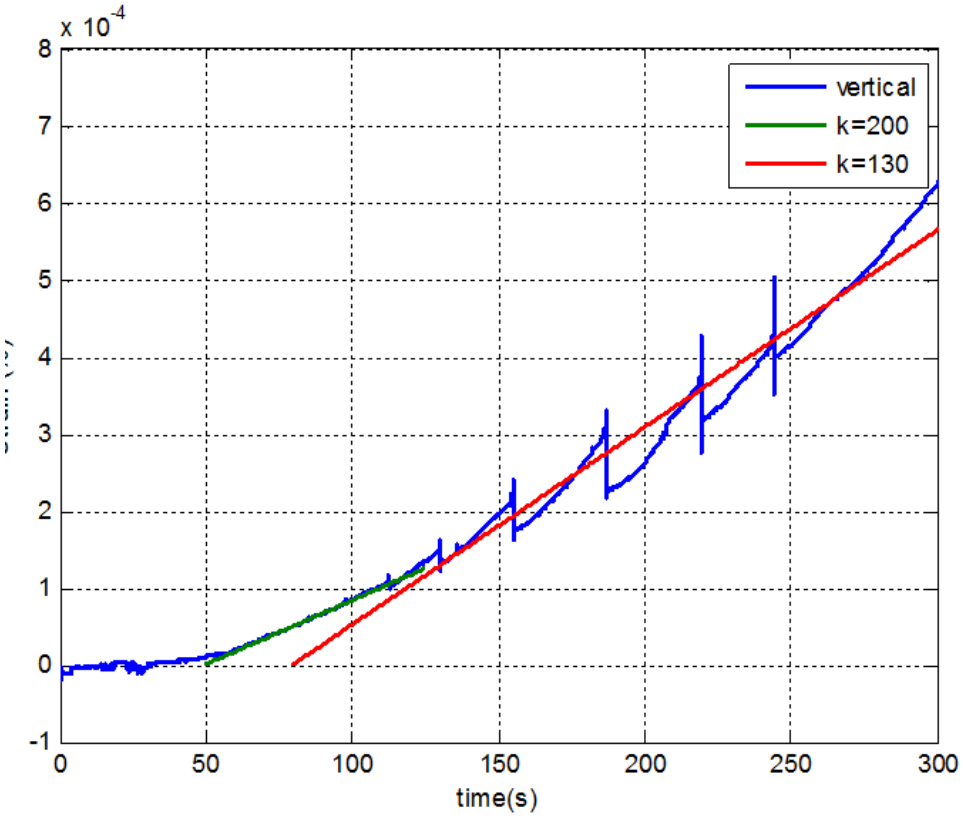

Figure 4.18. Transfer function for the vertical component of GT3.

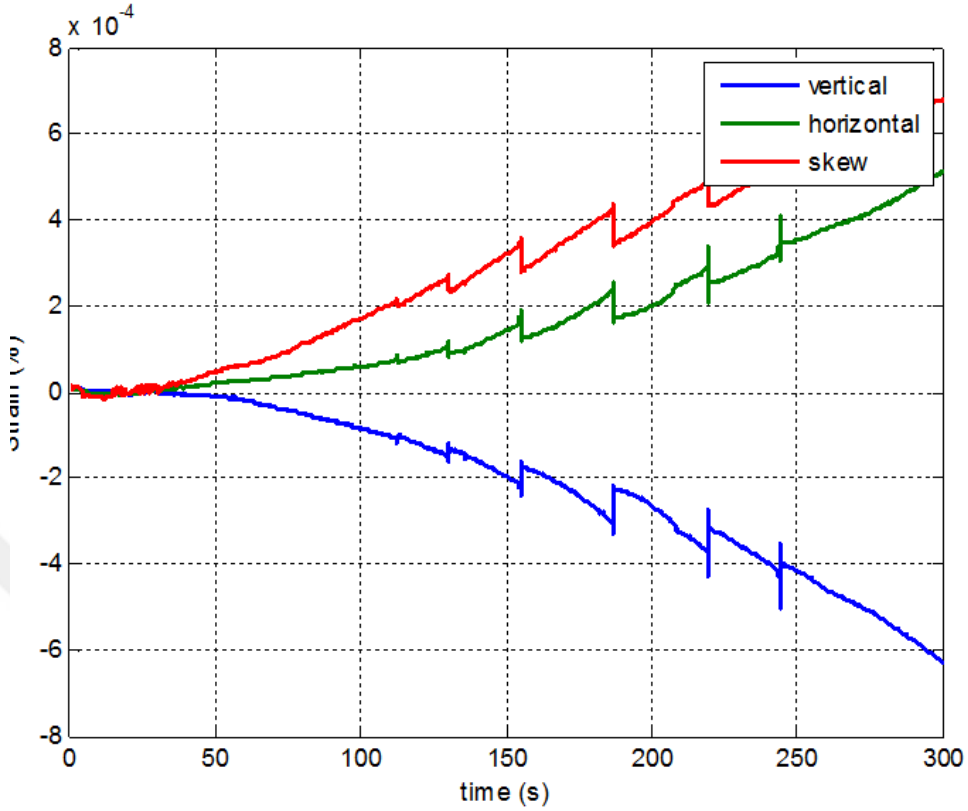

Figure 4.19. Response of strain gauges in all directions for GT3.

Different methods of strain rosette implementation (attachment) were devised for different materials. The spunbonded material, namely GT1, offered ease of strain gauge attachment. The material allowed for direct attachment of strain rosettes with the use of strain gauge adhesive. The locations of the strain rosettes are marked on the material and the strain gauge is attached in the desired orientation. The strain gauge adhesive is used to saturate the material's matrix of fibers and the strain rosette is applied. The strain rosette is pushed down for about 2 minutes by applying thumb pressure.

The method of strain rosette attachment for GT2 and GT3 are slightly different than that of GT1. GT2 is a woven geotextile which has a polished surface. In order to attach strain gauges to this material the strain gauge attachment surface had to be agitated with sand paper. Care was taken not to completely breakdown the fiber structure in the process. Once the surface was ready for strain rosette placement, strain gauge adhesive was applied and the strain rosette was placed. The method of strain

gauge attachment for GT3 was probably the most cumbersome. The fibers of GT3 were almost inert to the strain gauge adhesive used. There were large gaps between the individual fibers, as well. The adhesive was not retained on the geotextile's surface long enough to allow for the bonding of the strain rosette. As a solution, the fibers of GT3 were sandwiched between a 40 mm by 40 mm piece of GT1 and the strain rosette. The adhesive was administered on the strain gauge attachment location of GT3 which was underlain by a piece of GT1. GT1 was selected due its high adhesive absorption capacity. The strain rosette was then placed on the attachment location, locking the fibers of GT3 between itself and the lower layer of GT1 which retains the adhesive. Figure 4.20 illustrates the 20 strain rosettes attached to GT1 and a close up image of a singular strain rosette. Figure 4.21 illustrates the GEC reinforcements made out of GT2 and GT3 instrumented with strain rosettes.

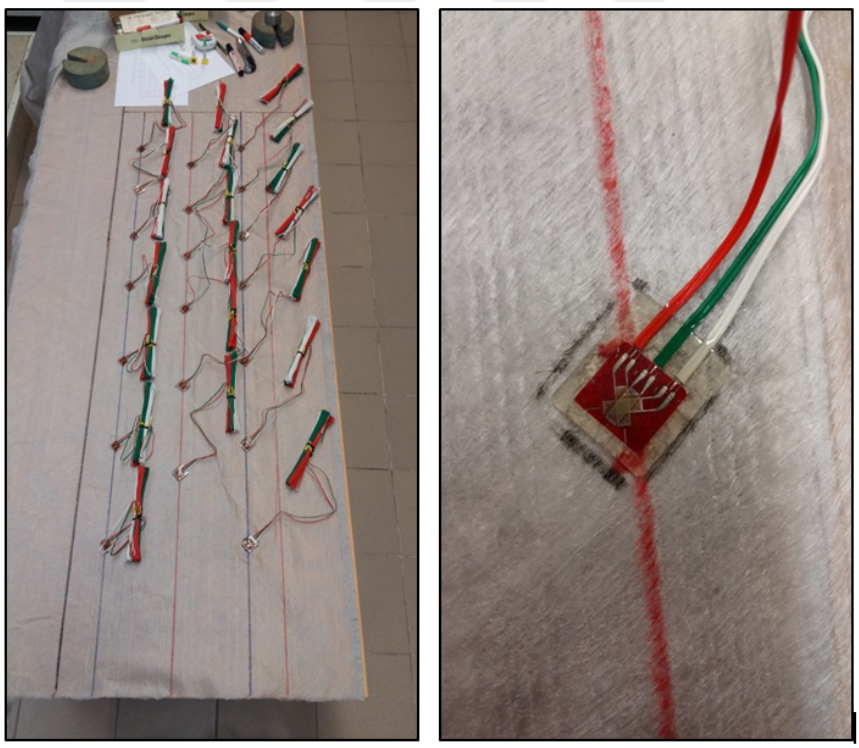

Figure 4.20. Attached Strain Gauges to GT1.

Figure 4.21. Instrumented reinforcements made up of GT2 and GT3.

4.4.2. Sensor Calibration and Data Logger System

The reliability of the data gathered by the sensors is dependent of proper calibration of sensors under controlled conditions. Within the scope of this study, the sensors are calibrated in laboratory conditions and where applicable, the sensor calibrations are checked prior to the deployment of sensors.

Calibration of soil pressure gauges is a difficult process which should be undertaken with extreme caution as outlined by Talesnick (2013). It is generally accepted that the size, flexibility and geometry of the measuring device relative to the soil will have a profound effect on the response and reliability of the soil pressure measurements. Studies that deal with soil pressure measurement strongly express the importance of calibration and testing under controlled conditions prior to utilizing any sensing system in actual testing configurations (Talesnick, 2013). It is therefore imperative that a through calibration effort is made before the deployment of soil pressure gauges. In this study, the soil pressure gauges are calibrated by applying incremental levels of

stress under controlled conditions. The response of the soil pressure gauge is measured and a calibration chart specific to each soil pressure gauge is created. The soil pressure calibration test setup is illustrated in Figure 4.22. The soil pressure gauge is placed under an air bladder which is vertically supported with a reaction frame. The pressure in the air bladder is incrementally increased by making use of a precision air regulator (Fairchild air regulator located on the Humboldt Flex Panel in Karl Terzaghi Soil Mechanics Laboratory) which has an analog manometer unit. The point-wise calibration curve is thusly acquired for various pressure levels.

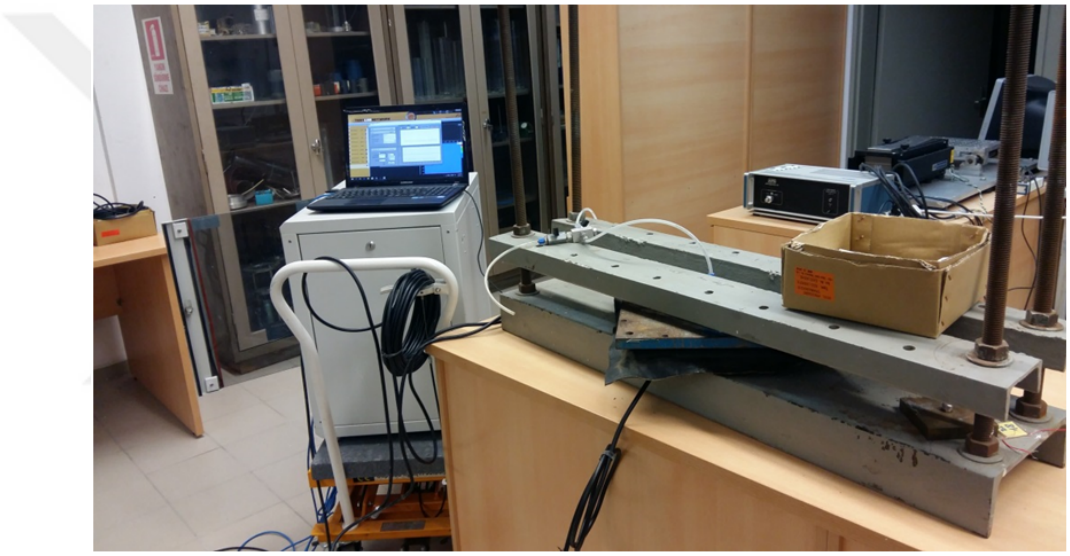

Figure 4.22. Soil pressure gauge calibration setup.

The load cells and the pneumatic actuators are also calibrated against each other by making use of the load frame illustrated in Figure 4.23. The pneumatic pistons used in the consolidation and stress-controlled column loads tests are tested at various air supply pressures to ensure that their force outputs are accurate and controllable. Similarly the load cell is loaded with the pneumatic pistons to ensure that the force readings are properly calibrated. The calibration setup is illustrated in Figure 4.23.

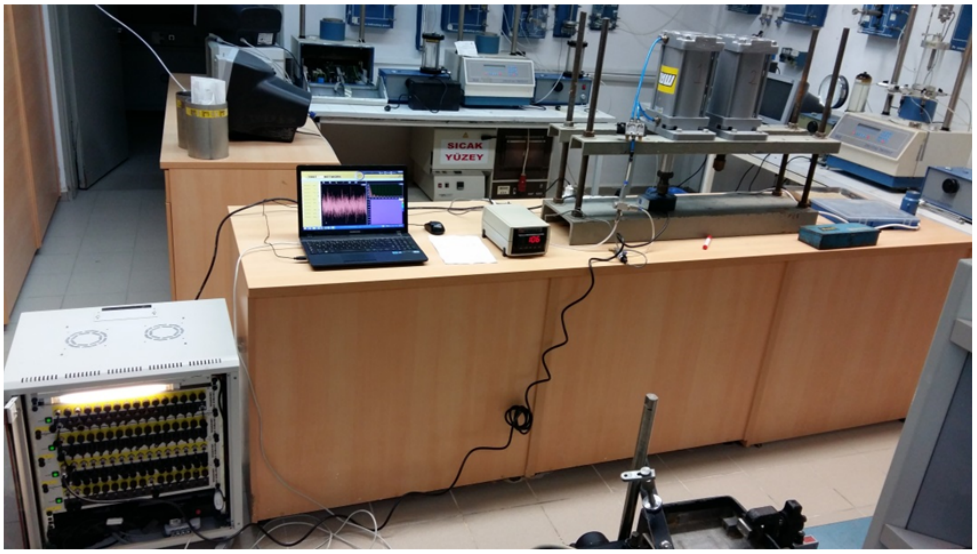

Figure 4.23. Load cell and pneumatic piston calibration setup.

Pore water pressure gauges (TML, KPB-PA, 500) are calibrated by making use of the calibration factors that are supplied by the producer. The calibration of the sensors are initially checked against hydrostatic pressure. Two 50 mm diameter Plexiglas tubes (1000 mm in length) are connected to each other to create a water column of about 2 m against hydrostatic pressures. Once the measurements of the hydrostatic water pressures yielded satisfactory results, the grooved end of the sensors were connected to the cell pressure outlet of the Humboldt Flex Panel equipment and water pressures are applied by making use of a precision air pressure regulator (Fairchild, M10). Care was taken not to exceed the maximum allowable pressure level (500 kPa) of the transducers.

The lase displacement sensors are calibrated by allowing the sensor to measure known distances that are within the measurement range (for Leuze ODSL 96B laser displacement sensor the minimum and maximum measurement ranges are 140 to 1400 mm) of the sensor. Calibration curves are created for each of the 16 laser displacement sensors used and the values are uploaded to the data logger interface. The pore water pressure gauges (KPB-PA-500, TML) were calibrated against a 2 meters deep static water column. The sensors were dipped in the water column at various depths and the sensor readouts were checked against the manufacturer's prescribed calibration factors. The MEMs type accelerometers used were calibrated against the gravity by applying

voltage reduction factors supplied by the manufacturer. The values of measured accelerations were checked against the gravity. The complete list tabulating the details of the used sensors is provided in Table 4.1.

Table 4.1. List of the sensors used in the experiments.

Sensor Type	Quantity	Brand	Range	Model
Laser Displacement Sensor	16	Leuze	14-1400 mm	ODSL 96B
Accelerometer	12	TDG	0-2 g	SenseBox-7001
Accelerometer	4	TDG	0-5 g	SenseBox-7001
Pore Water Pressure Gauge	10	TML	0-500 kPa	KPB-PA, 500
Soil Pressure Gauge	4	TLM	0-500 kPa	KDC-PA, 500
Watertight Strain Rosette	180	TML	30000 Micro Strain	WFRA-6-11-5L

The data logger utilized in the forthcoming study is a dynamic data logger with a sampling rate of 2 kHz. The data logger is comprised of 7 racks containing 16 channels which amount to 112 channels. A user interface software is used to calibrate sensors, specify sampling rate, record data, and electronically zero the readings of the sensors. Lastly, it is worth mentioning that the strain gauge calibration is also undertaken through the user interface by adjusting the potentiometer on the quarter bridges used to zero the strain readings prior to testing.

5. SHAKING TABLE TESTING PROGRAM

5.1. Rigid Box Experiments

A total of eleven shaking table tests were performed using the shake table facility at the Department of Earthquake Engineering that functions within the Kandilli Observatory and Earthquake Institute of Bogazici University. The ANCO R-148 is a uniaxial horizontal vibration shake table with areal footprint dimensions of 3 m x 3 m. The shaking table is driven by virtue of a servo-hydraulic actuator. Test objects up to 10 tons can be accommodated over a frequency range of 0-50 Hz. The maximum stroke capacity of the shaking table is ± 120 mm.

The experimental program pertaining to Rigid Box experiments are given in Table 5.1. The shake table experimental scheme for Rigid Box experiments are consisted of five base excitations. The first three input motions are scaled versions of Imperial Valley earthquake's (1940, El-Centro Station, NS direction, PGA=0.32g) accelerogram record of El-Centro station that shall henceforth be named as El-Centro load case. The acceleration amplitudes of the original accelerogram were not scaled but rather the frequency content of the recording was scaled by a factor of $\sqrt{2}$. Here scaling refers to increasing the frequency values by a factor of $\sqrt{2}$. El-Centro load case was applied with 25, 50, and 100% amplitude to the experimental model. Kobe earthquake was also scaled with the exact same methodology and following El-Centro load cases of varying amplitudes, 50 and 100% Kobe (1995, KJMA Station, NS direction, PGA=0.89g) load cases were applied to the experimental model. The peak ground accelerations of the applied input motions were 0.08, 0.16, 0.32, 0.44, and 0.89 g, respectively. The Arias Intensities of the earthquake motions are 0.14, 0.47, 1.78, 4.56, and 17.69 m/s. The average frequency content for El-Centro and Kobe excitations are 2 and 1.5 Hz, respectively. Figure 5.1 and Figure 5.2 illustrate the induced 100% El-Centro and Kobe accelerograms.

Table 5.1. Experimental program pertaining to Rigid box experiments.

Shaking Event	Load Case	Model-Scale Duration (s)	Peak Ground Acceleration (g)	Peak Ground Displacement (mm)
1	El-Centro 25 %	32.02	0.08	46.2
2	El-Centro 50 %	32.02	0.16	57.7
3	El-Centro 100 %	32.02	0.32	68.3
4	Kobe 50 %	26.35	0.44	93.5
5	Kobe 100 %	26.35	0.89	107.9

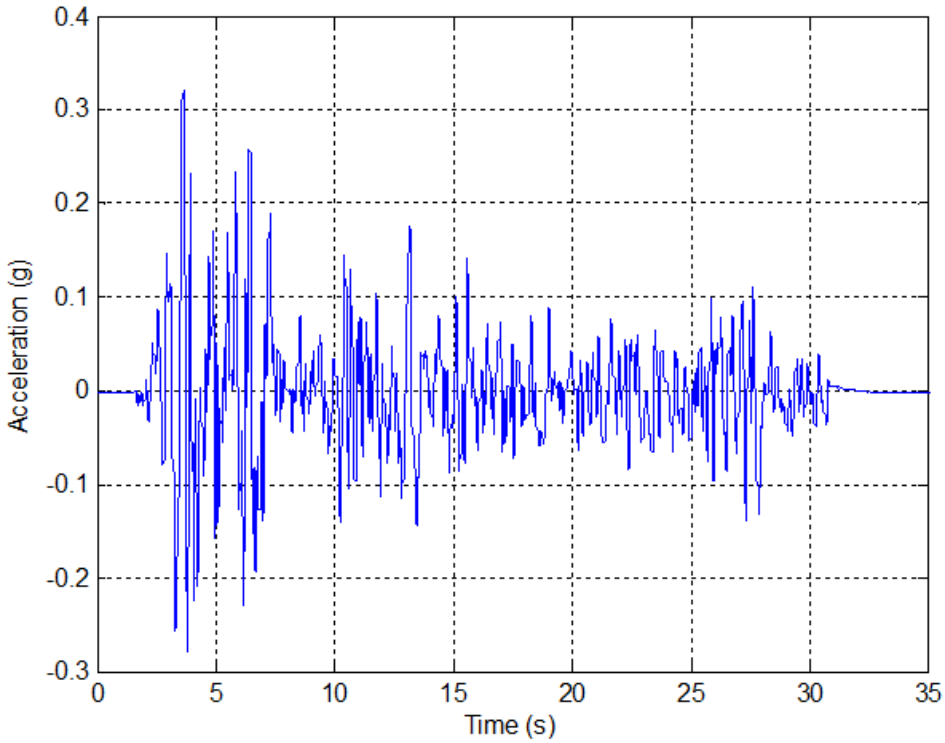

Figure 5.1. 100% amplitude El-Centro accelerogram.

In Table 5.2, the details of the experiments that are conducted utilizing the Rigid Box apparatus are given. The presence and type of geosynthetic reinforcement, dimensions, infill material type, and columns' end-bearing properties are tabulated in Table 5.2. The designations of the individual columns that are installed to Setups 1, 2, and 3 are also provided. The prefix f in columns' abbreviations indicates that the column is a floating column, in the absence of such a prefix it is inherently assumed that the column is end-bearing. As expected abbreviations OSC and GEC refer to Ordinary Stone Column and Geosynthetic Encased Column, respectively.

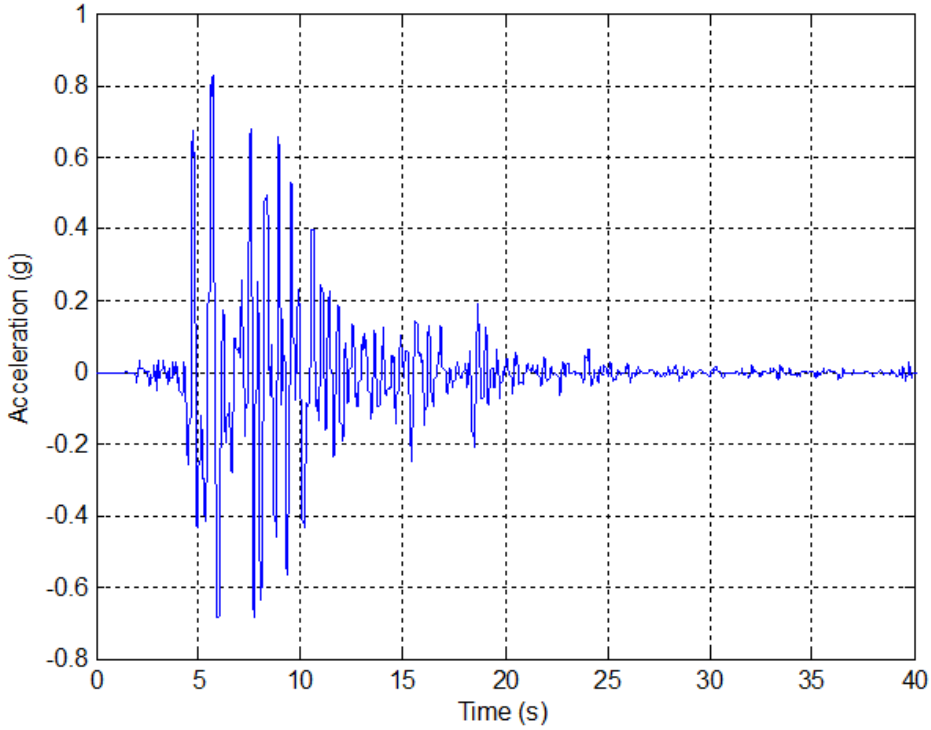

Figure 5.2. 100% Amplitude Kobe accelerogram.

The suffix s and g indicate the infill material for the columns with the infill material being sand for the former and gravel for the latter. Finally, the superscript numbers ranging from 1 to 3 indicate which setup the column belongs. This is provided in the abbreviations of the column designations for ease of analysis of the results. There is a total of two unit cells which are untreated for purposes of studying the benchmark condition where the soft clay is not enhanced with granular column inclusions. Accordingly, these unit cells are simply designated as Clay Bed^1 and Clay Bed^2. Throughout the course of Rigid Box experiments, floating and end-bearing OSCs with various infill materials and GECs of varying reinforcement and infill material are tested.

Table 5.2. Details of the columns in each Setup tested in Rigid Box experiments.

Setup #	Reinforcement	Column Designation	Dimensions			Infill Type
			Height (mm)	Diameter (mm)	Type	
	-	f-OSC-g1	1000	168	Floating	Gravel
	-	Clay Bed1	-	-	-	-
Setup 1	-	OSC-g1	1500	168	End-bearing	Gravel
	GT1	GEC-1-g1	1500	168	End-bearing	Gravel
	-	OSC-s2	1500	168	End-bearing	Sand
	GT1	GEC-1-s2	1500	168	End-bearing	Sand
Setup 2	-	f-OSC-g2	1000	168	Floating	Gravel
	-	Clay Bed2	-	-	-	-
	-	OSC-g3	1500	168	End-bearing	Gravel
	GT2	GEC-2-s3	1500	168	End-bearing	Sand
Setup 3	GT2	GEC-2-g3	1500	168	End-bearing	Gravel
	GT3	GEC-3-g3	1500	168	End-bearing	Gravel

5.2. Laminar Box Experiments

The shaking table tests conducted in conjunction with the Laminar Box apparatus are subdivided in two major groups. The first group of shaking table tests is consisted of sinusoidal wave forms of varying amplitude and frequency. The motivation for these experiments was the ease in analysis of the response of the soil column contained in the laminar box under the action of harmonic base excitations. These experiments are designated as Sinusoidal Excitation Scheme. The second group of the experiments is mainly comprised of simulated earthquake accelerograms of El-Centro and Kobe with varying amplitudes. The designation of this second group of load cases is Earthquake Excitation Scheme. The El-Centro and Kobe input motions used in the Earthquake Excitation Scheme in Laminar Box experiments are exactly the same as the ones used in Rigid Box experiments. The load case designations, peak ground accelerations, and duration of the load cases are tabulated in Table 5.3 and Table 5.4 for Sinusoidal and Earthquake Excitation Schemes, respectively. In Table 5.5, the model designations, column treatments and the Excitation Schemes that the models are subjected to are given for the entire testing program undertaken with the Laminar Box apparatus. Model 9 which is tabulated in Table 5.5 is an experiment where the laminar box is not subjected to base shaking. Instead, OSCs and GECs are brought to failure under

the action of stress controlled vertical loading tests. The columns in the models which are subjected to base shaking are also subjected to vertical load tests. Model 9 is designated as Intact Columns and the objective is to compare the vertical load carrying characteristics of the dynamically loaded and intact columns.

Table 5.3. Detains of the testing program for Sinusoidal Excitation Scheme.

#	Load Case	PGA (g)	Duration (s)
1	Pulse*	0.07	1
2	Sinesweep-1	0.1	60
3	0.5 Hz	0.1	40
4	1 Hz	0.13	40
5	1.5 Hz	0.3	40
6	2 Hz	0.35	40
7	3 Hz	0.68	40
8	4 Hz	0.76	40
9	5 Hz	0.81	40
10	Sinesweep-2	0.1	60
*Pulse signal is the first crest of the Sinesweep-1 signal			

Table 5.4. Detains of the testing program for Earthquake Excitation Scheme.

#	Load Case	PGA (g)	Duration (s)
1	Whitenoise-1	0.07	300
2	El-Centro 25 %	0.09	35
3	El-Centro 50 %	0.18	35
4	El-Centro 100 %	0.38	35
5	Whitenoise-2	0.07	300
6	Kobe 50 %	0.41	40
7	Kobe 100 %	0.82	40
8	Whitenoise-3	0.07	300

Table 5.5. Details of the models tested with the Laminar Box apparatus.

Model	Designation	Treatment	Excitation Scheme
1	Clay-S	-	Sinusoidal
2	OSC-S	ϕ 136 mm OSC x 4	Sinusoidal
3	GEC-J400-S	ϕ 136 mm GEC, GTX1 x 4	Sinusoidal
4	GEC-J1000-S	ϕ 136 mm GEC, GTX2 x 4	Sinusoidal
5	Clay-EQ	-	Earthquake
6	OSC-EQ	ϕ 136 mm OSC x 4	Earthquake
7	GEC-J400-EQ	ϕ 136 mm GEC, GTX1 x 4	Earthquake
8	GEC-J1000-EQ	ϕ 136 mm GEC, GTX2 x 4	Earthquake
9	Intact Columns	OSC, GEC GTX1, GEC GTX2 x 4	Static Vertical Load

The first crest of the Sinesweep signal that is tabulated in Table 13, is used as a pulse loading. More specifically the difference in the arrival time of the shear wave (the first crest of the signal in Sinesweep loading) to various instrumentation (accelerometer) levels is used to determine the shear wave velocity of the experimental models the results pertaining to this load case and analysis technique will be elaborated in the subsequent sections of this dissertation. Sinesweep signal has a duration of 60 seconds. The signal starts of at a loading frequency of 1 Hz and the loading frequency changes in every 4 seconds. The loading frequency of the signal progressively increases and in the last four seconds of the signal the loading frequency becomes 15 Hz. The signal sweeps the experimental model in a frequency window where the models probable resonant frequency may be encountered. The Sinesweep signal time history is illustrated in Figure 5.3.

Once the Sinesweep signal is induced on the models that are tested in the Sinusoidal Excitation Scheme, sinusoidal input motions with increasing frequency and maximum acceleration amplitude are applied to the model. The amplitude of the loading is increased with increasing frequency to invoke larger displacements and shear strains within the tested soil body. The acceleration time histories pertaining to 0.5, 2, and 5 Hz load cases are illustrated in Figure 5.4, Figure 5.5 and Figure 5.6, respectively.

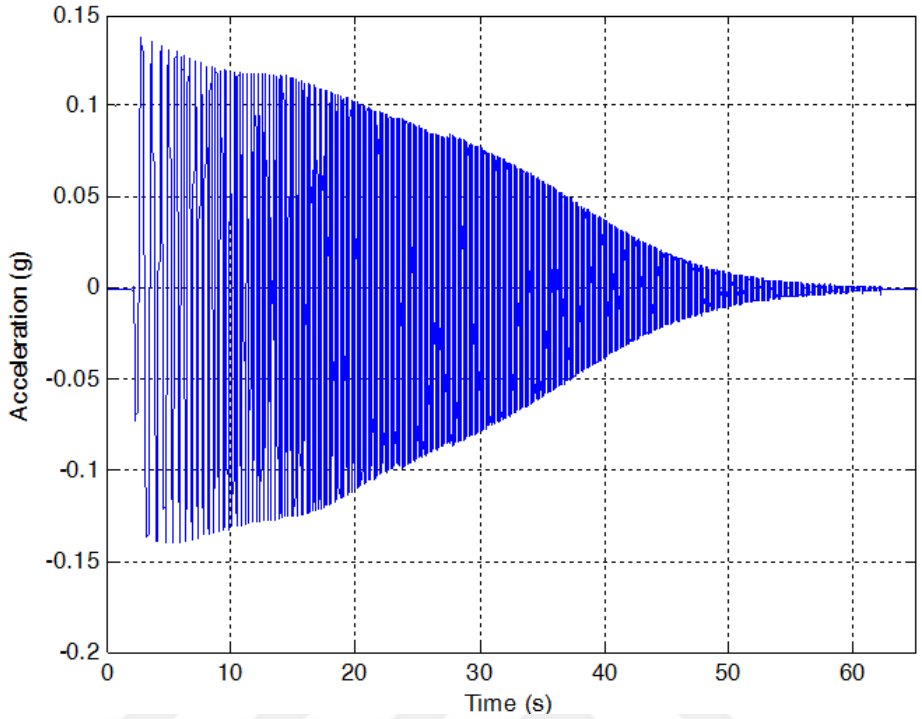

Figure 5.3. Sine sweep signal.

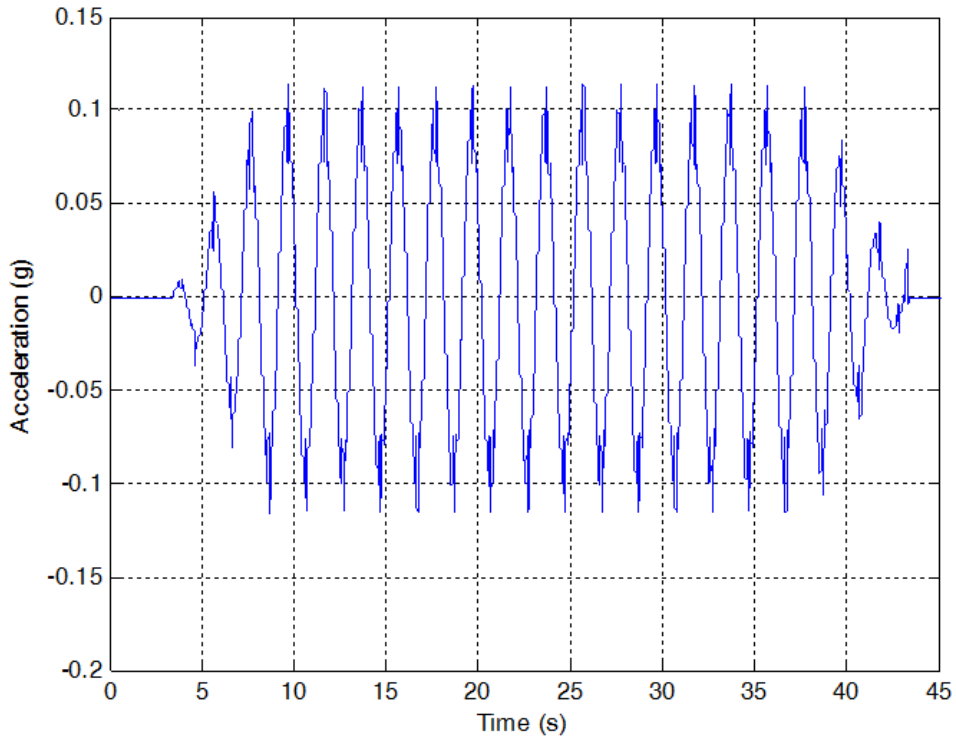

Figure 5.4. Acceleration time history for 0.5 Hz load case.

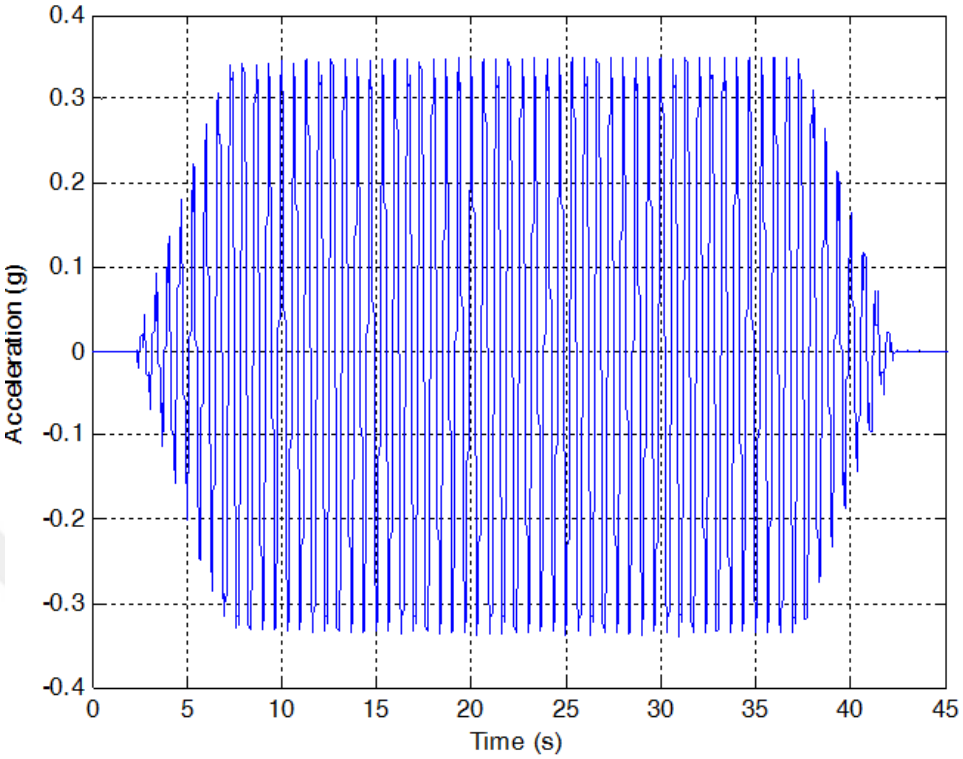

Figure 5.5. Acceleration time history for 2 Hz load case.

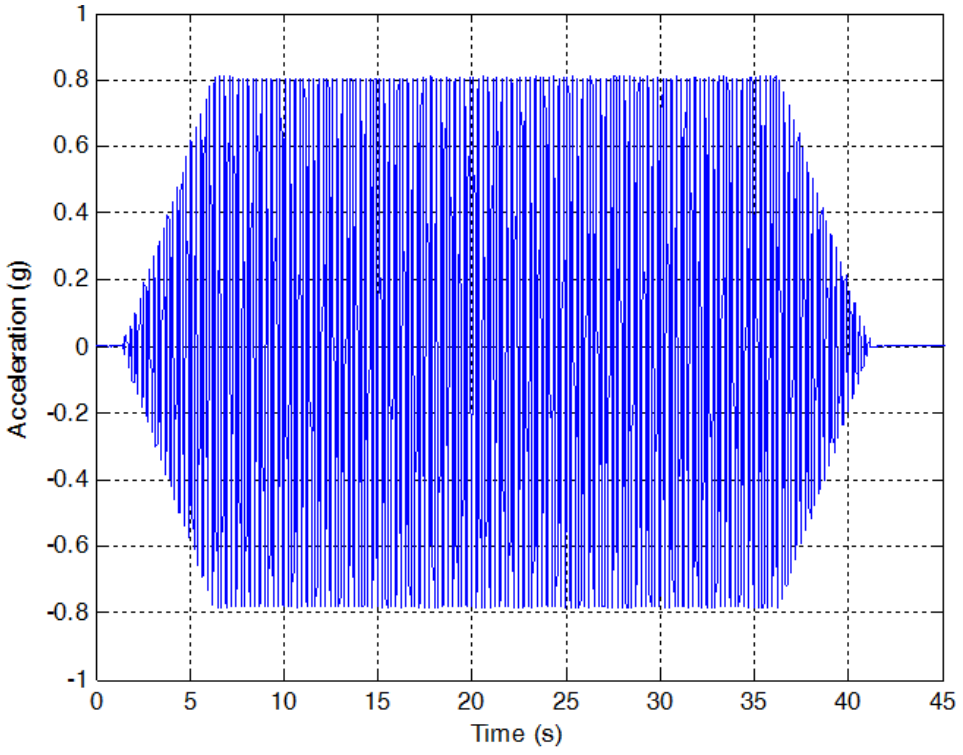

Figure 5.6. Acceleration time history for 5 Hz load case.

The Gaussian White Noise signal is illustrated in Figure 5.7. The duration of the signal excluding the zero pads at the beginning and at the end of the signal is 300 seconds. The White noise signal was employed as a modal testing technique by which the fundamental frequency of the model soils contained in the laminar box could be found. The fundamental frequency of the model soil was then used to calculate the low-strain stiffness of the soil deposit. The random white noise signal was generated utilizing MATLAB and the frequency content (bandwidth) of the white noise signal was 1-50 Hz. The acceleration time history plot of the white noise signal could be seen in Figure 5.7. Sufficient amount of zero pads were allowed both in the beginning and at the end of the signal in order to avoid problems with Fast Fourier Transform (FFT).

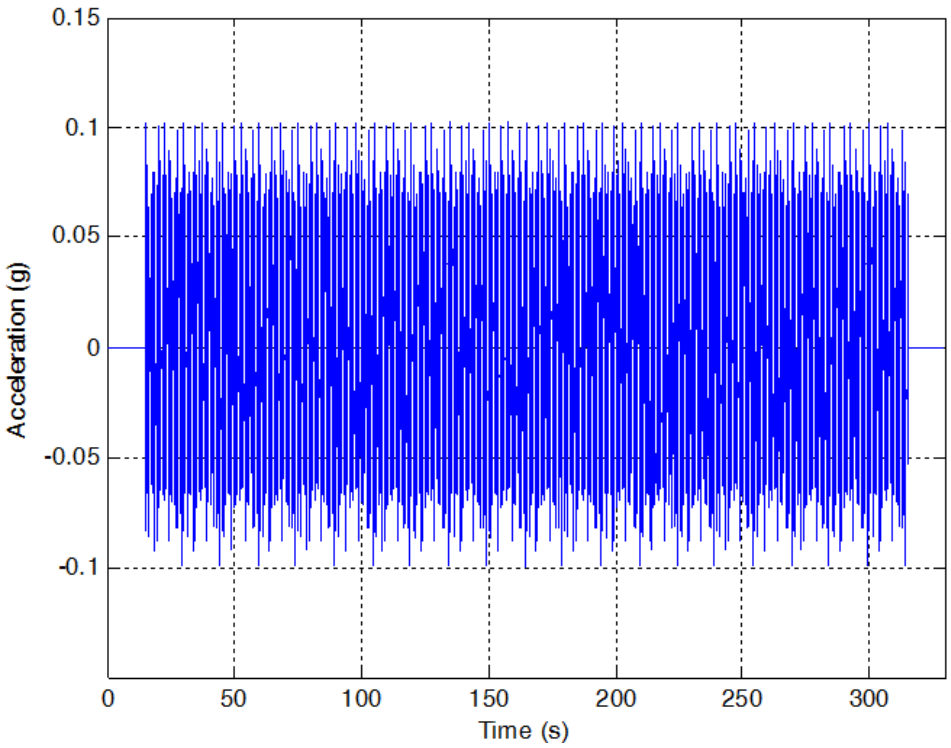

Figure 5.7. Gaussian White Noise signal's acceleration time history plot.

6. RIGID BOX RESULTS

The results discussed in this section of the dissertation is based on the materials published by the Geotextiles and Geomembranes journal titled "Seismic Behavior of Geosynthetic Encased Columns and Ordinary Stone Columns" with authors Cihan Cengiz and Prof. Erol Güler (2018). The dissertation author is the first author of this paper.

The rigid box assembly was produced to be a physical analogy of the GECs and OSCs that are not subjected to free-field conditions but rather confined with an earth retaining structure such as sheet pile walls, retaining walls, bridge abutments, etc. In order to limit the reflection of seismic waves from the boundaries of the testing assembly, EPS blocks are employed at either end of the box that is facing the direction of shaking. The rigid box assembly was produced to house four model unit cells with OSCs and GECs at the geometric center. The unit cells were 520 x 575 mm in plan with a depth of 1500 mm. The diameters of the columns were 168 mm which yields an aspect ratio (height to diameter) of about 10. A photograph of the rigid box assembly mounted on shaking table is given in Figure 6.1. The constituents of the physical models are subjected to seismic excitations with a sustained surcharge load of 25 kPa. Surcharge plates are used in the application of the vertical overburden stress to simulate an embankment load at the column head plane. The strains occurring in the geosynthetic reinforcements encasing the columns, settlement of the surcharge plates, acceleration applied to the system, and the displacement of the system is measured.

Figure 6.1. Rigid box assembly mounted on the shaking table.

6.1. Settlement of the Unit Cells under Seismic Loading

In order to evaluate the seismic performance of the foundation system provided with GEC or OSC enhancement, the settlement of the unit cells are measured and their relative performances are compared. In the analysis, it is assumed that the foundation system supports a superstructure that is sufficiently wide in both directions and no rocking, uplifting or non-grounding of the edges of the foundation occur. It is also inherently assumed that punching failure of the overlying superstructure does not take place.

The settlement response of the unit cells tested in Setup 1 under the action of 100% Kobe accelerogram is depicted in Figure 6.2. The settlement response of the unit cells throughout the experimental program typically resembled the settlement behavior depicted in Figure 6.2. The surcharge plates were initially at rest. Upon application of the dynamic base shaking, there was significant downward movement of the surcharge plates which was captured by the laser displacement sensors. The occurrence of the unit cell settlement coincided with the onset of the significant duration of the applied accelerograms for all loaded cases. Significant duration of an earthquake is the time interval in between the points at which 5% and 95% of total seismic energy of an

earthquake expressed in terms of Arias Intensity (IA) has been recorded. In Figure 6.2, the Husid plot pertaining to 100% Kobe accelerogram is plotted alongside with two data points that depict the 5 and 95% seismic input energy. The data points that correspond to 5 and 95% IA are at 24.45 and 34.47 seconds, respectively. It is readily seen that the settlements of the unit cells took place in this time window under the action of sustained 25 kPa surcharge load. With a major part of the settlements taking place during the significant duration of the applied earthquake loading, it is deducted that the recorded settlement response is induced by the dynamic loading.

While some of the settlements could be attributed to the densification of the sand layer, the stiffness of the columns clearly aid in the vertical load capacity performance of the individual unit cell. The cumulative unit cell settlements for setups 1, 2, and 3 are illustrated in Figure 6.3, Figure 6.4, and Figure 6.5, respectively. The untreated clay beds and the unit cells with floating ordinary stone column (f-OSC) inclusions experienced the highest amount of settlement. Out of the three end-bearing OSCs the gravel filled OSCs, namely, OSC-g^1 and OSC-g^3, performed slightly better than the sand infilled OSC-s^2 by experiencing 10 mm less settlement on average. The "soft" GT1 was utilized as a holding medium for the strain rosettes and the columns confined with GT^1 showed slightly better performance than the unconfined counterparts. The probable cause of increased settlement performance can be explained by the capability of weak geotextile to keep the column constituents intact during seismic loading.

In order to compare the performance of the granular column inclusions, two different settlement reduction factors are defined namely, Settlement Reduction Factor A and Settlement Reduction Factor B. The settlement values and reduction factors are tabulated in Table 6.1. Settlement Reduction Factor A defines the improvement achieved by adding column inclusions with and without encasement in comparison to clay bed itself. Settlement Reduction Factor B is defined as the improvement achieved additionally by using a geosynthetic encapsulation compared to the average performance of columns without encasement.

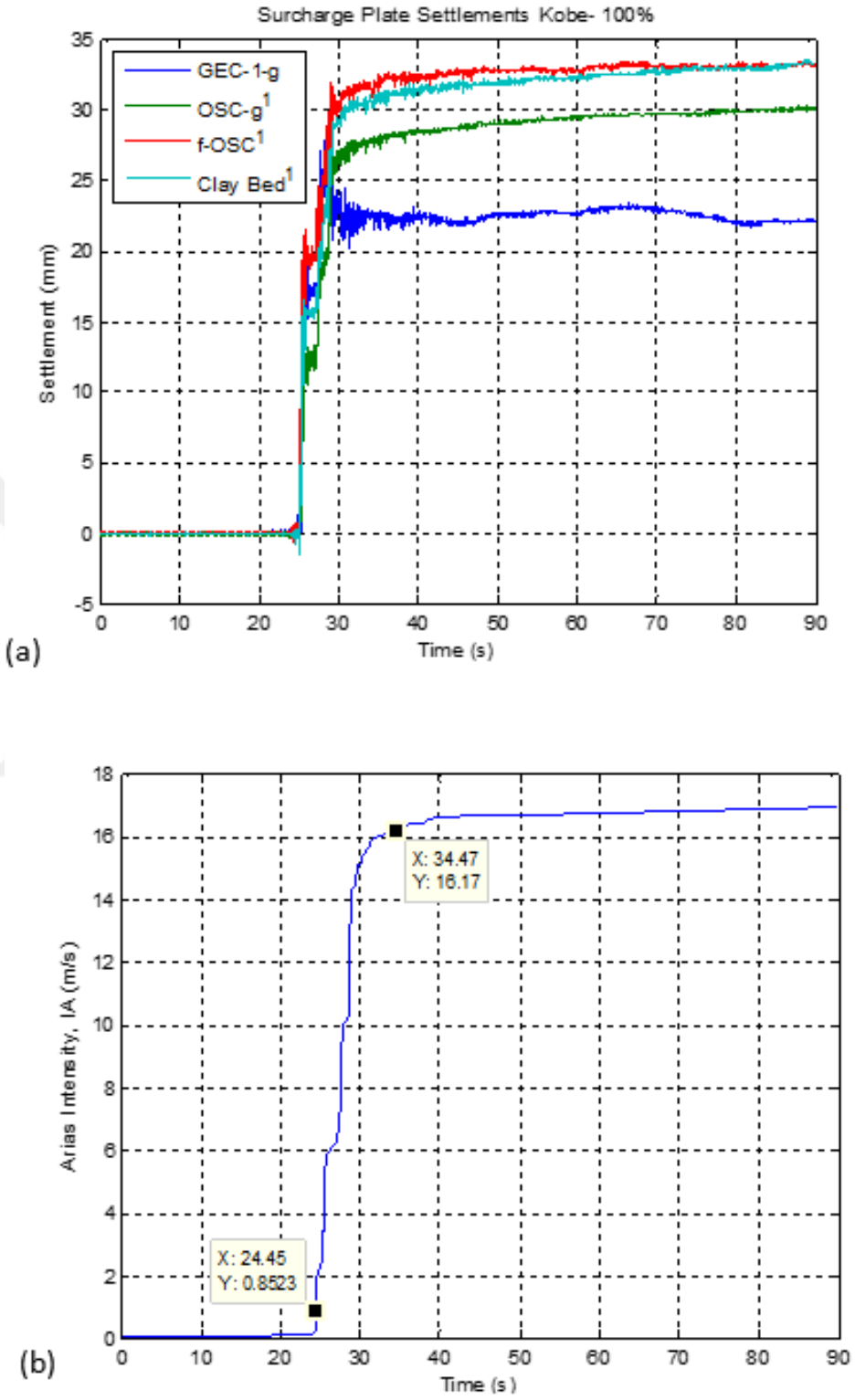

Figure 6.2. (a) Settlement response of the unit cells subjected to 100% Kobe accelerogram and (b) significant duration window of the accelerogram shown on a Husid plot.

In general it is seen that the increasing geotextile tensile stiffness yielded increased settlement reduction performance for all cases. While the unit cell enhanced with GEC-2-s[3] achieved settlement reduction factors A and B of 37 and 23%, the same values for the unit cell enhanced with GEC-2-g[3] were 43 and 30%, respectively. Since the sole difference in these unit cells are the column infill material, it could be said that granular column infill performed better for the GECs encased with GT2.

Further, the unit cell with GEC-3-g[3] inclusion exhibited 54 and 44% settlement reduction for factors A and B, respectively. Increased reinforcement modulus combined with the gravel infill yielded highest settlement reduction factors. Upon comparing the column performances, it could be said that gravel infill is more efficient in limiting the overall unit cell settlements.

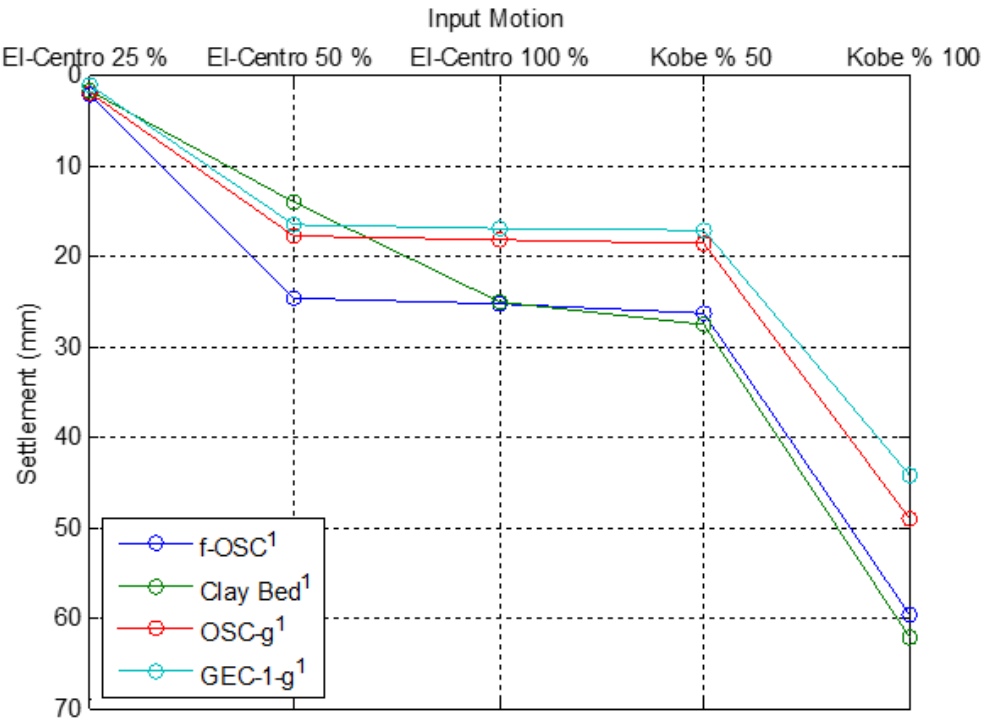

Figure 6.3. Cumulative settlement plots for Setup 1.

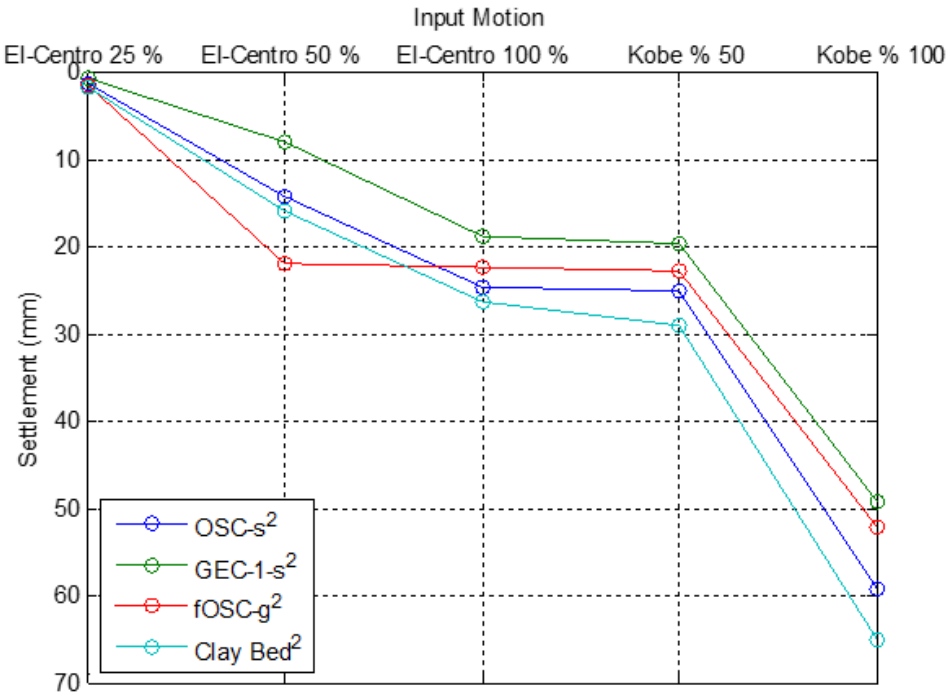

Figure 6.4. Cumulative settlement plots for Setup 2.

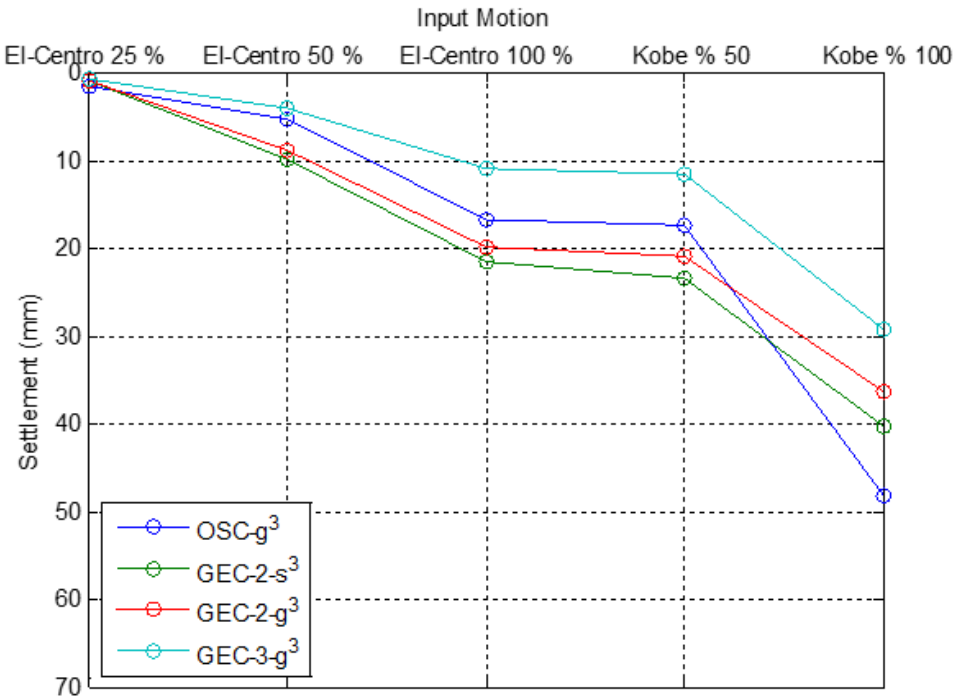

Figure 6.5. Cumulative settlement plots for Setup 3.

Table 6.1. Cumulative settlement values for the experimental program and calculated settlement reduction factors.

Column	Cumulative Settlement (mm)					Settlement	Settlement
Designation	El-Centro			Kobe		Reduction	Reduction
	25%	50%	100%	50%	100%	A (%)	B (%)
f-OSC-g1	2.15	24.73	25.29	26.43	59.69	6	-
Clay Bed1	1.67	23.55	25.11	27.62	62.1	-	-
OSC-g1	2.04	17.84	18.27	18.67	49.03	23	-
GEC-1-g1	1.24	16.47	16.89	17.12	44.24	30	15
OSC-s2	1.25	18.31	24.68	25.01	59.17	7	-
GEC-1-s2	0.82	17.96	18.93	19.66	49.19	23	6
f-OSC-g2	1.58	22.07	22.46	22.85	52.27	18	-
Clay Bed2	1.71	23.98	26.33	29.03	65.14	-	-
OSC-g3	1.55	15.36	16.77	17.45	48.29	24	-
GEC-2-s3	1.01	9.87	21.53	23.54	40.29	37	23
GEC-2-g3	0.92	8.91	19.97	21.03	36.35	43	30
GEC-3-g3	0.82	3.96	10.39	11.66	29.19	54	44

6.2. Strains Occurring on Geosynthetic Encasements during Seismic Loading

Measurements taken from strain gauges distributed at various elevations of the columns are used to evaluate the behavior of the GECs under seismic loading. Under the studied conditions, 3 different modes of reinforcement strain are observed. Figure 6.6 depicts the time dependent strain behavior of the reinforcement on GEC-2-g^3 at 400, 720, and 1040 mm depths during the 100% Kobe earthquake loading. In this particular case all three types of time - strain relationships were observed under 100% Kobe loading. Type A is the strain behavior where the strain increases with the application of seismic loading and the residual strain remains more or less at the maximum value after the loading ends. In Type B behavior, the strain curve in time domain reaches a peak and then the strain decreases until it reaches a constant value (as seen in strain plot at 720 mm depth). Type C is where the nature of the strain changes, during the course of the seismic loading, from tensile to compressive (as in the case of strain at 400 mm depth).

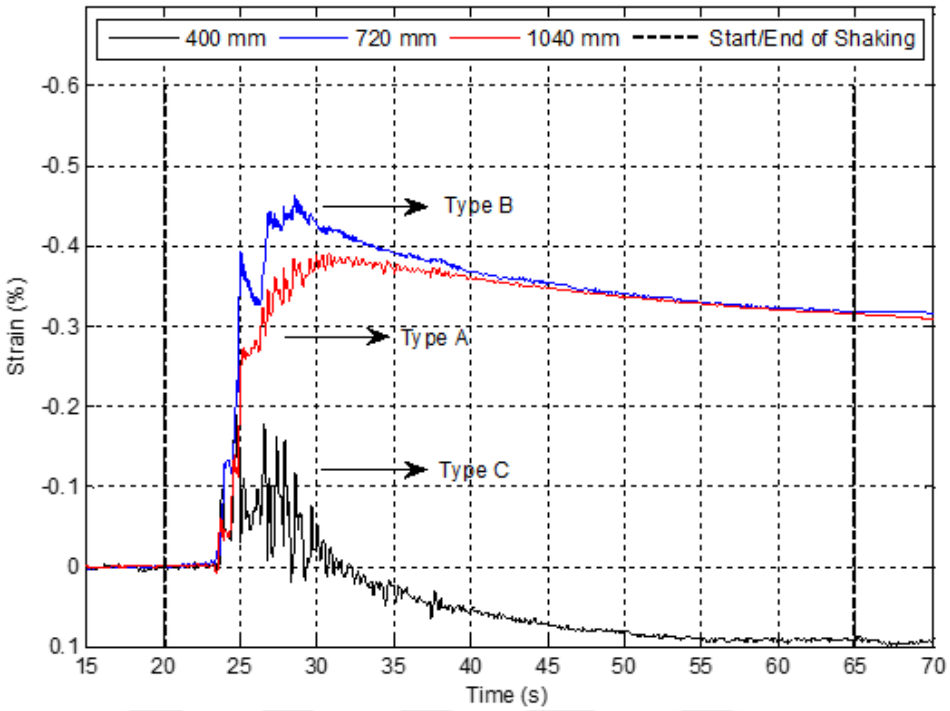

Figure 6.6. Type A, B, and C strains occurring on GEC-2-g[3] during 100% Kobe excitation.

Figure 6.7 depicts the response of the reinforcement to 100% Kobe loading at a depth of 560 mm on GEC-2-s[3] column. The response of the reinforcement to the applied loading is partially plastic. The peak reinforcement strain is observed during the time window of the applied dynamic load followed by the recovery of strains upon termination of the dynamic loads. The reinforcement response is antagonistic with horizontal extension (tensile strains) causing vertical contraction (compressive strains). In the upcoming chapter of the dissertation a more through account of the behavior of the reinforcement in terms of local strains will be presented.

In the analyses of the strains occurring on the encasement, the strain readings are reset after each earthquake shaking. Therefore the strains shown in Figure 6.8 to 50 give the additional stresses occurring during each shaking sequence and show the maximum measured strains for that specific strain gauge during seismic input motions.

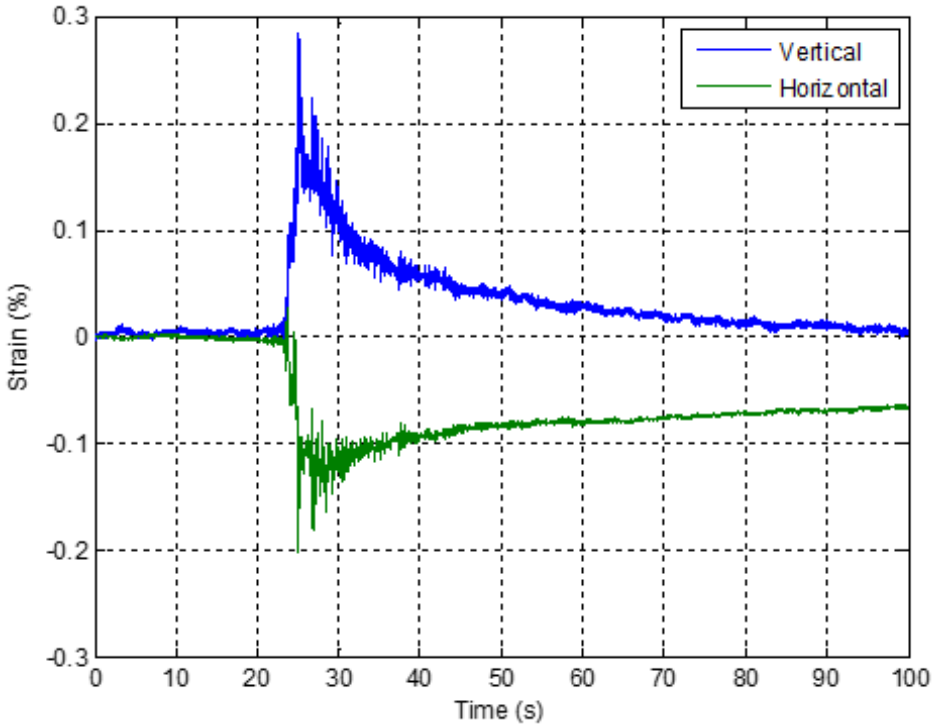

Figure 6.7. Strain response of the GT2 material that encased GEC-2-s[3] at a depth of 560 mm.

Figure 6.8 and Figure 6.9 show the maximum strains measured on columns encased with GT1. In Figure 6.8, GEC-1-g[1] exhibits distinctive peaks of strain at a depth of 560 mm both for 100% El-Centro and Kobe earthquake loading. GEC-1-g[1] had a maximum horizontal strain of 2.5% at 560 mm depth. GEC-1-s[2] experienced a maximum horizontal strain of about 2.5% at an elevation of 940 mm under the action of 100% Kobe excitation. 100% El-Centro loading caused 1.6% strain at the same elevation. Both of these columns, encased with GT1, showed localized distinct peaks of strain for 100% El-Centro and Kobe excitations. It is seen that these columns, after being subjected to 100% El-Centro loading, did not undergo large strains under the action of 50% Kobe excitation. The next excitation to trigger large strains was 100% Kobe recording. GT1 was intended to serve as a bearing medium for the strain rosettes to study the behavior of ordinary stone columns under seismic loading. With the realistic assumption that the confinement offered by GT1 is very low, it is seen that ordinary stone columns undergo high strain (deformation) under seismic impact.

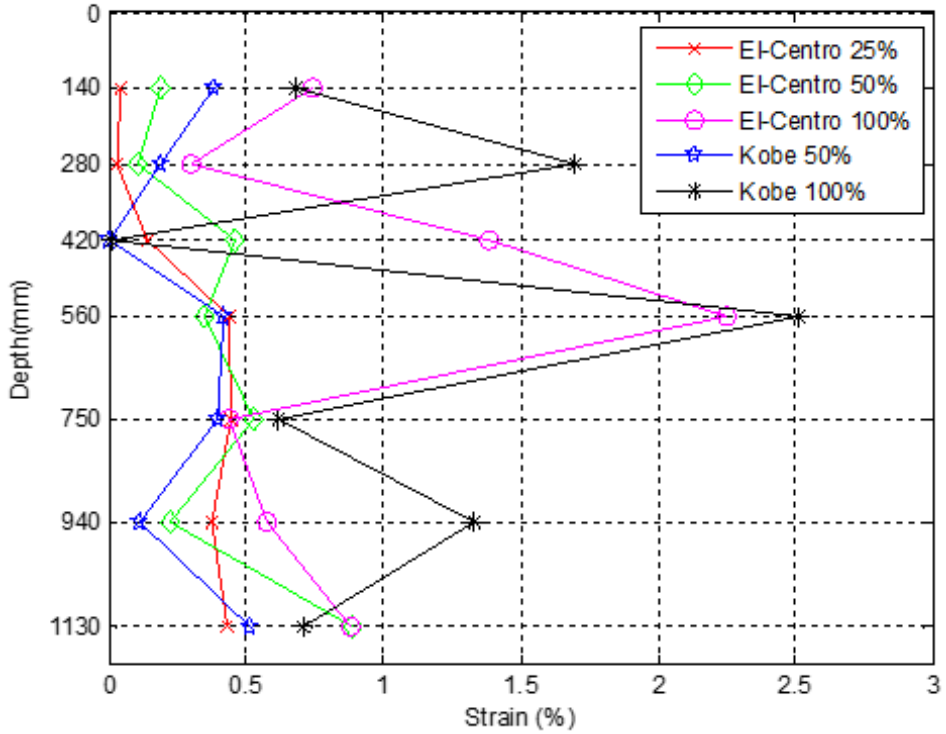

Figure 6.8. Maximum strains measured on GEC-1-g[1] under different excitations.

In Figure 6.10, the strain response of GEC-2-s[3] is illustrated. The horizontal strains for GEC-2-s[3] remained below 0.1% for all El-Centro accelerograms. 100% amplitude Kobe earthquake motion caused a maximum horizontal strain of about 0.5% at 880 mm depth. The horizontal strain demand on the reinforcement was at relatively low values at depths below 880 mm for all input motions. At this particular depth, under the action of 50% and 100% Kobe excitation, the strain demand reached peak values and from this point on, towards the upper portion of the column, the strain demand decreased. Strain response of the GEC illustrated in Figure 6.10 suggests that, similar to columns encased with GT1, which are essentially ordinary stone columns, there is a high strain demand on the reinforcement at the lower portion of the encased column which lies at a depth of approximately 5 to 7D.

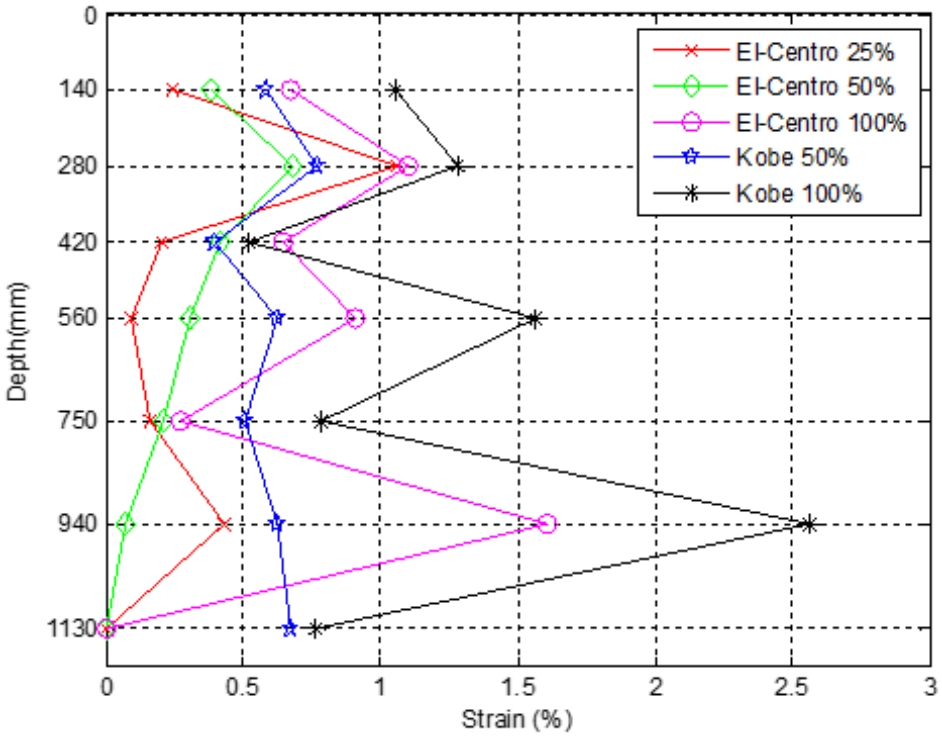

Figure 6.9. Maximum strains measured on GEC-1-g[1] under different excitations.

While partial encasement of upper part of GECs effectively mitigates bulging failure under static vertical loads in a homogeneous soft soil, it is seen here that such a solution may not be adequate for the design of GECs against seismically induced loads. The maximum strains occurring on GEC-2-g[3] under the action of seismic loading are illustrated in Figure 6.11. The distribution patterns of maximum strains throughout the height of the columns reinforced with GT2 for various earthquake loads are essentially similar. It is seen that strains developing at each loading stage create more or less equal strain increments at a given height with the exception of 100% Kobe loading which yields a large strain demand in the lower portions of the columns. Similar to GEC-2-s[3], the maximum strain demand on GEC-2-g[3] under the action of 100% Kobe loading, causes a large leap in strain at a depth of 5D to 7D. At the topmost instrumentation level there is almost no strain demand on the reinforcement. Both of the columns reinforced with GT2 have undergone maximum reinforcement strains of about 0.5%.

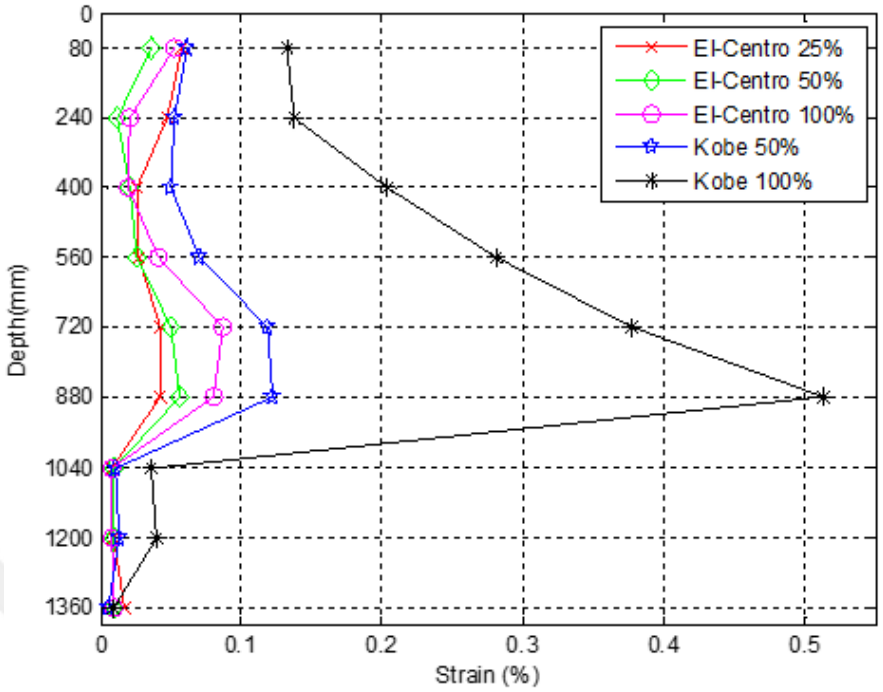

Figure 6.10. Maximum strains measured on GEC-2-s[3].

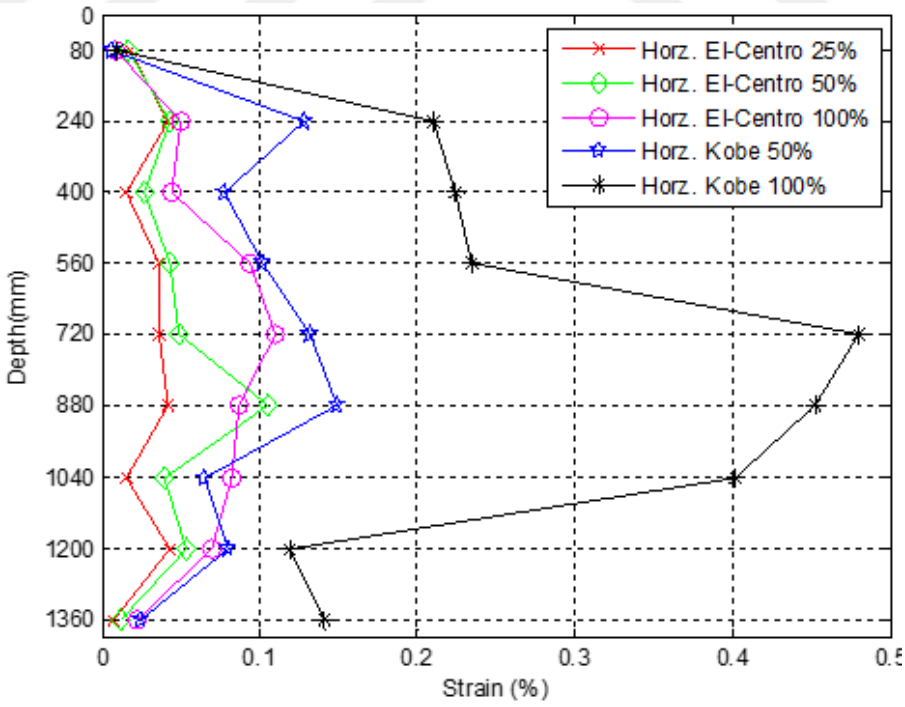

Figure 6.11. Maximum strains measured on GEC-2-g[3].

Figure 6.11 depicts the maximum strains on GEC-3-g[3]. All earthquake loads except for 100% Kobe loading evoked similar straining patterns on the reinforcement

with maximum strains being less than 0.2%. For these earthquake loads the upper portion of the reinforcement experienced a relatively higher strain demand. During the 100% Kobe excitation, both the pattern and the magnitude of the maximum strain changed. Instead of having a distinct maximum strain zone (GEC-2-s^2 and GEC-2-g^2 has these zones at depths of 880 and 720 mm, respectively), the curve in Figure 6.11 exhibits many local increased strain zones. In other words, there are more than one bulging zones at the elevations of 400, 720, and 1040 mm. This behavior can be attributed to the effect of including a relatively high modulus geotextile. Instead of bulging at a distinct location as in the case of the lower modulus counterparts, the high modulus material confines the gravel inside the column and the bulging of the column occurs over the entire height of the column. Similar findings have been reported by Hong *et al.* (2016) for the static loading case where the columns reinforced with relatively higher stiffness geotextiles exhibit roughly uniform deformation along the height of the column instead of a pronounced bulging deformation. In the upper portion of GEC-3-g^3, in elevations between 80 to 240 mm, strain demands on the reinforcement during seismic excitations except 100% Kobe earthquake are larger than GEC-2-s^3 and GEC-2-g^3.

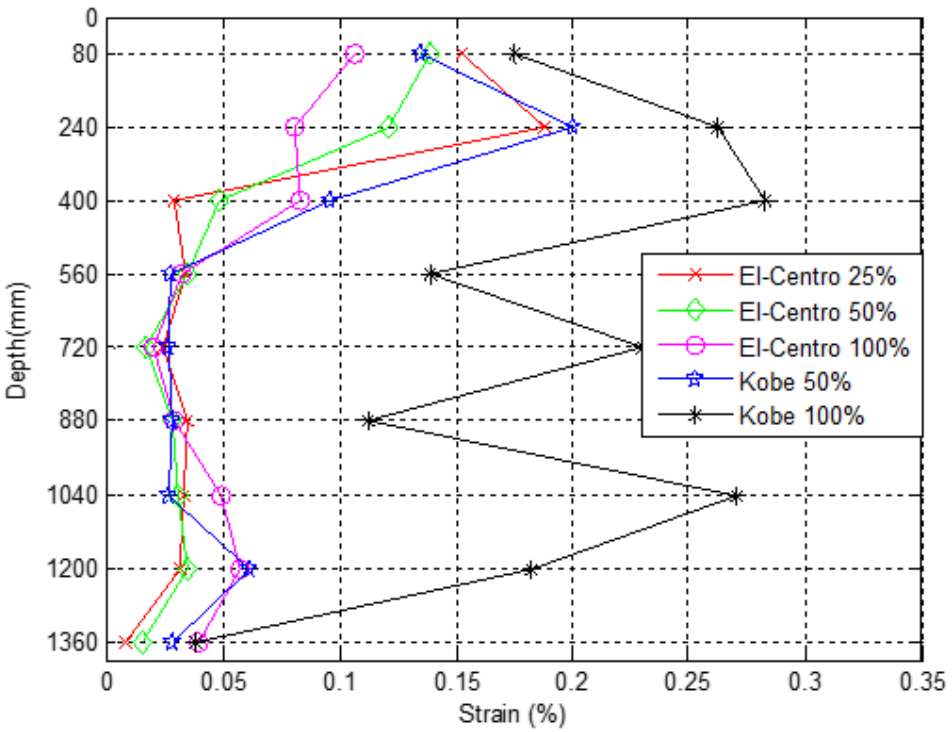

Figure 6.12. Maximum strains measured on GEC-3-g^3.

6.3. Interplay between Arias Intensity and Seismic Reinforcement Strains of Type A and B

Arias Intensity, IA (Arias, 1970) is an earthquake intensity measure that captures amplitude, frequency content, and duration of a strong ground motion and therefore it is a good indicator of the destructiveness of an earthquake. Arias Intensity correlates well with several commonly used demand measures of structural performance, liquefaction, and seismic slope stability. The cumulative seismic energy given by an earthquake is calculated as the integral of the square of the acceleration time history and it is expressed in time domain in a graph termed as Husid plot (Travasarou *et al.*, 2002). Following formula is used in calculating the Arias Intensity:

$$IA = \frac{\pi}{2g} \int_0^{T_d} a(t)^2 dt \tag{6.1}$$

Figure 6.13 demonstrates the 100% El-Centro accelerogram, the corresponding Husid plot where the cumulative seismic input energy (Arias Intensity) is expressed in time domain, strain occurring on GEC-1-s^2 at an elevation of 280 mm from column head plane, and the plots of strain versus IA. When the Arias intensity is calculated at consecutive times starting from the beginning of the earthquake, a relation such as given in Figure 6.13(b) is obtained. Although the ultimate IA value depends on the nature of the earthquake, the trend in time is similar in all earthquakes and is similar to the Strain versus Time curve (for example Figure 6.13c). This similarity has been obtained for Type A and B strain. Therefore the Arias Intensity was selected as a parameter to relate the time dependent strain response of the GEC reinforcement (encasement). While applied acceleration causes the deformations in the reinforcement, the reinforcement response is not elastic and therefore it does not follow the trend of the accelerogram. Rather as explained above the strains in the geosynthetic are developing cumulatively over time as the earthquake loads are imposed on the soil-geotextile system as represented by the IA. Therefore obtaining meaningful correlations

between these two quantities can serve as a predictive tool in assessment of tensile stresses in the encapsulation. In the plot of strain versus IA an almost linear increase in strain is observed with increasing values of IA. Similar relationships between IA and strain values are observed throughout the tested columns. Figure 6.14 shows a similar relationship for the strains occurring on GEC-2-g[3] at 880 mm elevation below column head plane under the action of 100% Kobe earthquake excitation. It is seen that the reinforcement strains developing under seismic input energy could be resembled by a linear or bilinear plot where the first portion has a trend of linear increase with increasing IA and the second portion is a horizontal plateau.

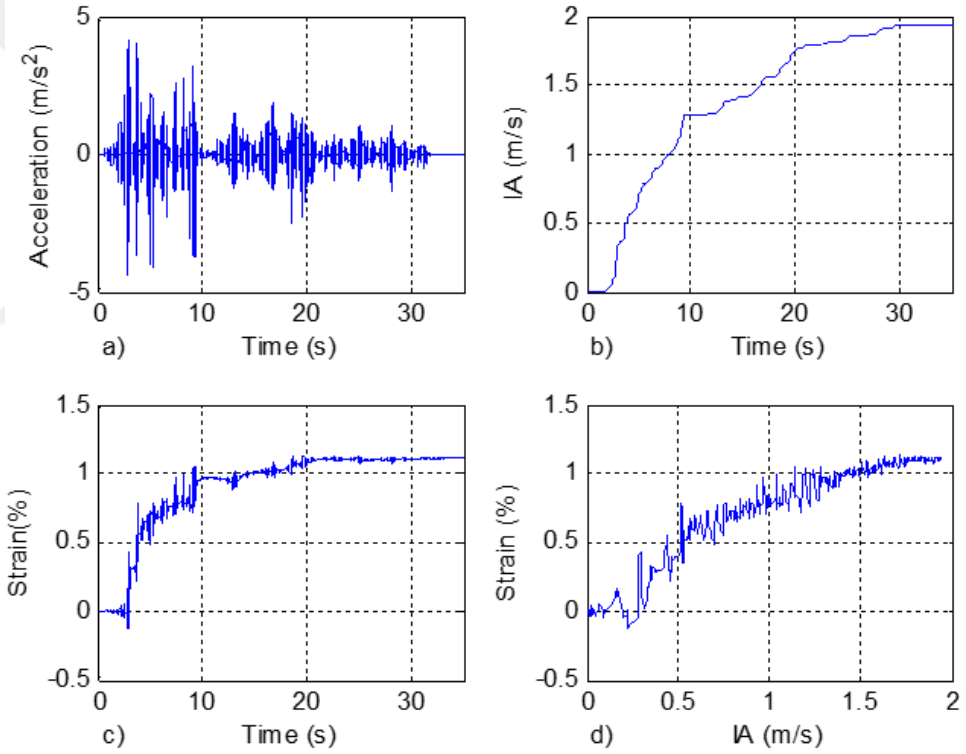

Figure 6.13. a) 100% amplitude El-Centro accelerogram, b) Husid plot for 100% amplitude El-Centro accelerogram, c) strain on GEC-1-s[2] at 280 mm, d) strain versus IA.

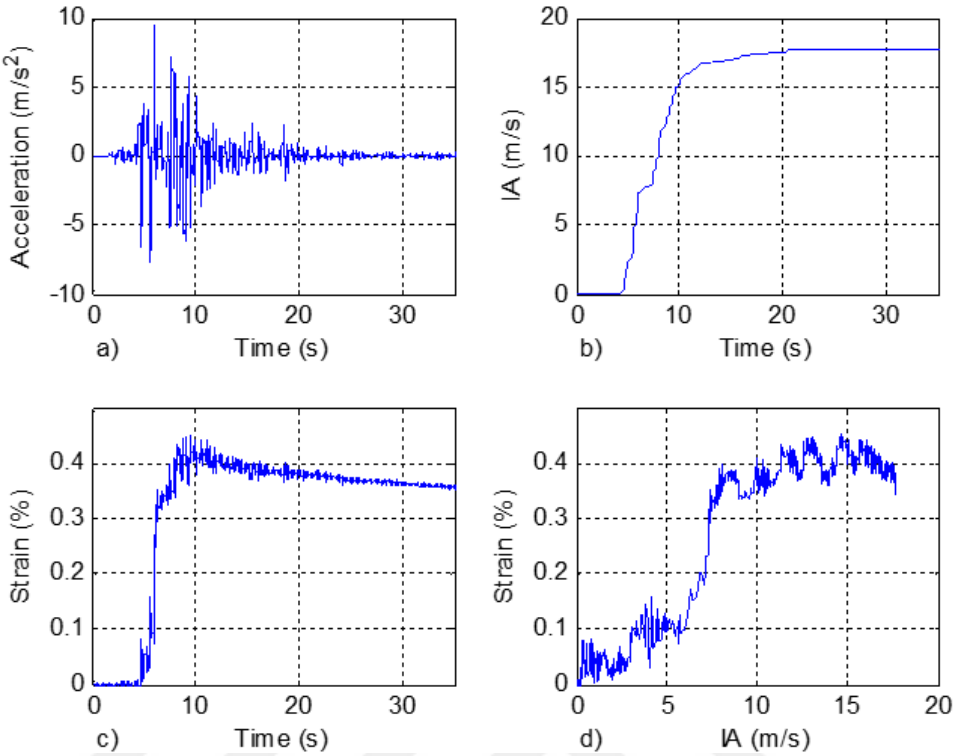

Figure 6.14. 100% amplitude Kobe accelerogram, b) Husid plot for 100% amplitude Kobe accelerogram, c) strain on GEC-2-s[3] at 880 mm, d) strain versus IA.

The interplay between IA and the reinforcement strains are consistent throughout the entirety of shaking table tests for a given location on the reinforcement. Figure 6.15 shows the strains occurring on GEC-2-s[3] at 720 mm elevation from the column head plane, the evolution of IA, strain versus IA, and normalized IA and strain plots for all applied accelerograms. A linear approximation line is plotted to fit the general trend of the strain versus IA curve. Normalized IA and strain plots given in time domain could further prove that there is a correlation between IA and strains occurring on the confining geotextile. Figure 6.16 and Figure 6.17 show similar set of curves for GEC-2-g[3] and GEC-3-g[3] to that of Figure 6.15 for strains at elevations of 1040 mm for the former and 1200 mm for the latter. It is seen that the almost linear relation between IA and reinforcement strain at a given point on the column is not only valid for a seismic loading stage but also for the entirety of the loading program. The reinforcement strain is consistently increasing with increasing seismic input energy. The slope of the linear approximation line is related with the tensile stiffness of the reinforcement geotextile

and the position of the strain reading on the column.

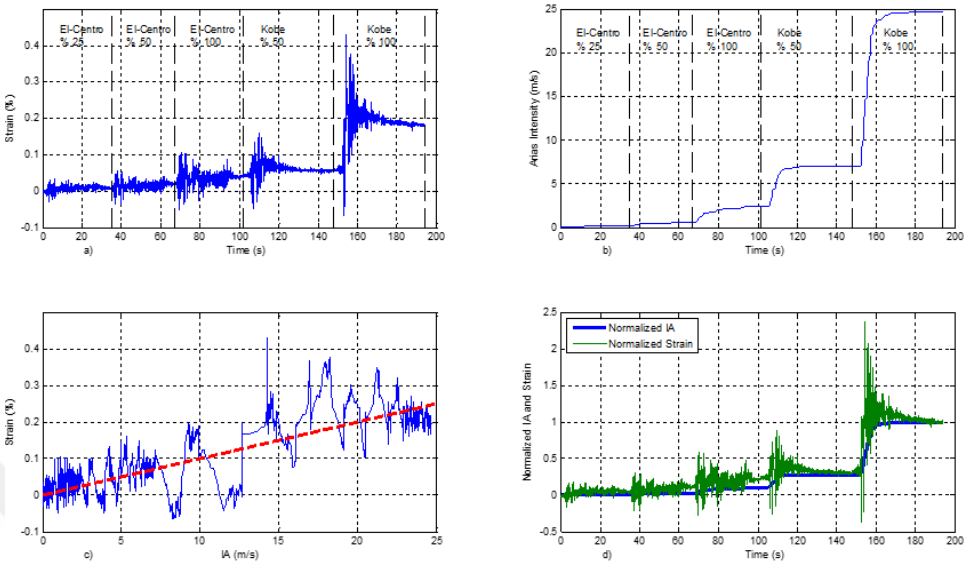

Figure 6.15. a) Horizontal strain on GEC-2-s[3] at 720 mm throughout seismic excitations, b) cumulative Husid plot for seismic excitations, c) strain versus IA, d) normalized strain and IA in time domain.

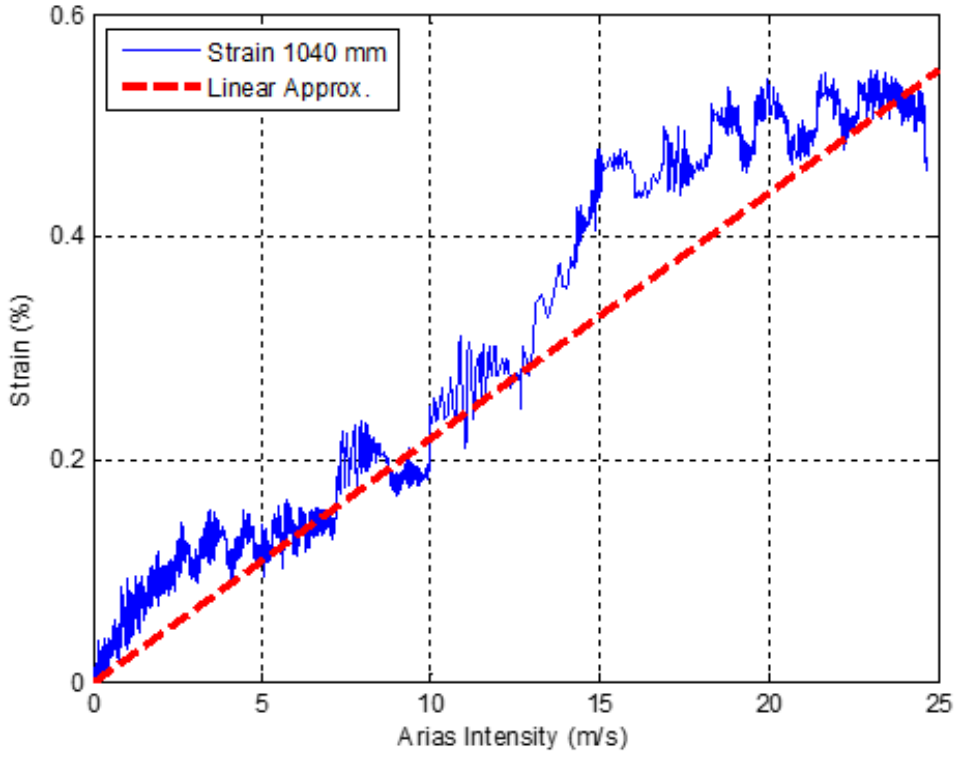

Figure 6.16. Linear approximation for IA and reinforcement strain for GEC-3-g[3] at 1200 mm throughout seismic excitations.

Figure 6.17 illustrate the evolution of maximum and average reinforcement strains as a function of peak ground acceleration (PGA). For both GEC-2-s[3] and GEC-2-g[3] the maximum cumulative strains are recorded at an elevation of 880 mm. For GEC-3-s[3] the location of maximum cumulative strain was at a depth of 1040 mm. As the tensile stiffness of the encasement increases, the maximum strains occurring due to seismic loading decrease. Although the maximum strain on GEC-3-s[3] is about half of the maximum strain developing on GEC-2-s[3] and GEC-2-g[3], the average strain values for these columns are in the same range, but the strain distribution is quite different. Since GEC-3-g[3] is reinforced with a stiffer geotextile, the strain demand is distributed more evenly along the column height and this prevents excessive straining at one distinct location. In Figure 6.17 also, the averages of the maximum strains at all heights are given. They indicate that the average values are significantly lower than the maximums and for example at the PGA of 0.89, it is approximately 0.2% regardless of reinforcement and infill type. Figure 6.17 may serve as a predictive tool in estimating the additional strain demand on GECs' reinforcement for seismically induced loads.

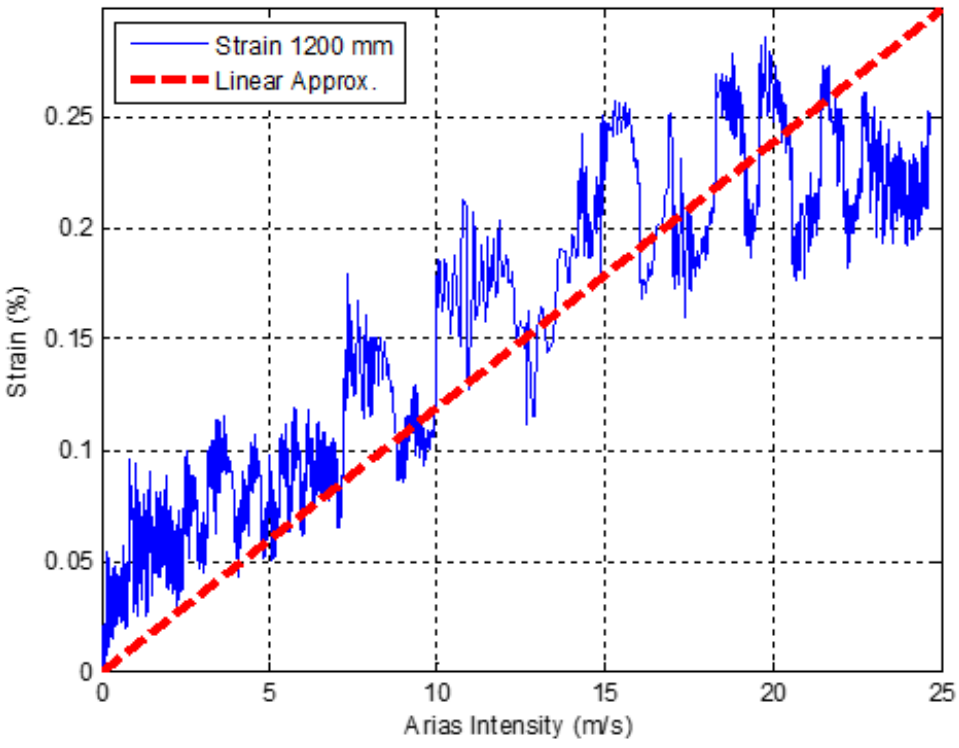

Figure 6.17. Maximum and average reinforcement strains in PGA domain.

6.4. Ramifications for Prototype Columns

As has been explained in detail in the previous sections, additional hoop strains develop in the geosynthetic encasement under earthquake loading conditions. In Figure 6.17, it can be seen that there is an almost direct relationship between these strains and PGA.

If the findings from the model study were extended to full field prototypes since the strains will remain the same but the tensile stiffness of the encapsulation geosynthetics will be 6.25 times higher than in the model. The additional stress created by the earthquake loading at various PGAs can be estimated as given in Table 6.2. Table 6.2 shows the model strains occurring on the reinforcement and the field prototype reinforcement stresses that these strains cause. At a PGA of 0.44, which corresponds to a highly seismic zone, the additional stress created during the earthquake will be approximately 9.6 and 8.8 kN for GT2 and GT3, respectively. For an extreme earthquake condition, similar to the Kobe earthquake, the additional tensile force in the reinforcement can be as high as 20.9 and 25.7 kN/m. As a result it is recommended that a margin for hoop (horizontal) tensile strength must be taken into consideration for earthquake loading conditions. These results also indicate that the confinement provided is of similar order of magnitude under the action of the earthquake load regardless of the stiffness of the reinforcement.

While 1-g shake table tests are possibly subjective to scale effects due to the influence of stress levels and the lack of reasonable scaling techniques (Latha and Santhanakumar, 2015), the size of soil sample that can be accommodated by the shaking table gives rise to a more reasonable scaling of the soil grain constituents of the model. Centrifuge tests on the other hand, offer more realistic representation of stresses that are typically occurring in the field. Centrifuge shaking table tests are generally regarded as being better than 1-g tests from the viewpoint of stress levels. However, the similitude of soil particle size is far less satisfied due to the relatively small model size (Wang *et al.*, 2017). Therefore the test results obtained from the experimental work can provide substantial insight into the behavior of field prototypes.

Table 6.2. Calculations of additional tensile forces on prototype columns' encasements

PGA (g)	Cumulative IA (m/s)	GT2		GT3	
		GT2 Strain	Prototype Additional Stress (kN)	GT3 Strain (%)	Prototype Additional Stress (kN)
0.08	0.14	0.04	1.06	0.03	2.09
0.16	0.61	0.14	3.7	0.06	4.02
0.32	2.39	0.23	5.88	0.11	7.14
0.44	6.95	0.38	9.61	0.14	8.82
0.89	24.64	0.83	20.92	0.41	25.72

6.5. Vertical Load Tests on Columns

Upon completion of the dynamic load tests, the vertical load carrying capacity of the columns were tested by making use of a 200 mm diameter loading cap. The vertical loading force was derived from a pneumatic piston that is identical to the ones used for surcharge loading. The surcharge plates and laser displacement sensors targeted on the plates and stress-controlled column load test setup are illustrated in Figure 6.18. Exhumed column (GEC-1-g[1]) after the column load tests and a close up image of the exhumed GEC-3-g[3] is illustrated in Figure 6.19. The pressure was applied through a precision air regulator with increments of about 25 kPa. Each stress increment was maintained on the column head plane for a duration of 120 seconds. Once the air pressure capacity of the loading system was exhausted (at a vertical pressure of about 300 kPa), the columns were unloaded with and reloaded with increments of 50 kPa. The reinforcement strain and settlement responses that will be illustrated in the rest of the present chapter include both the loading and the unloading response of the columns.

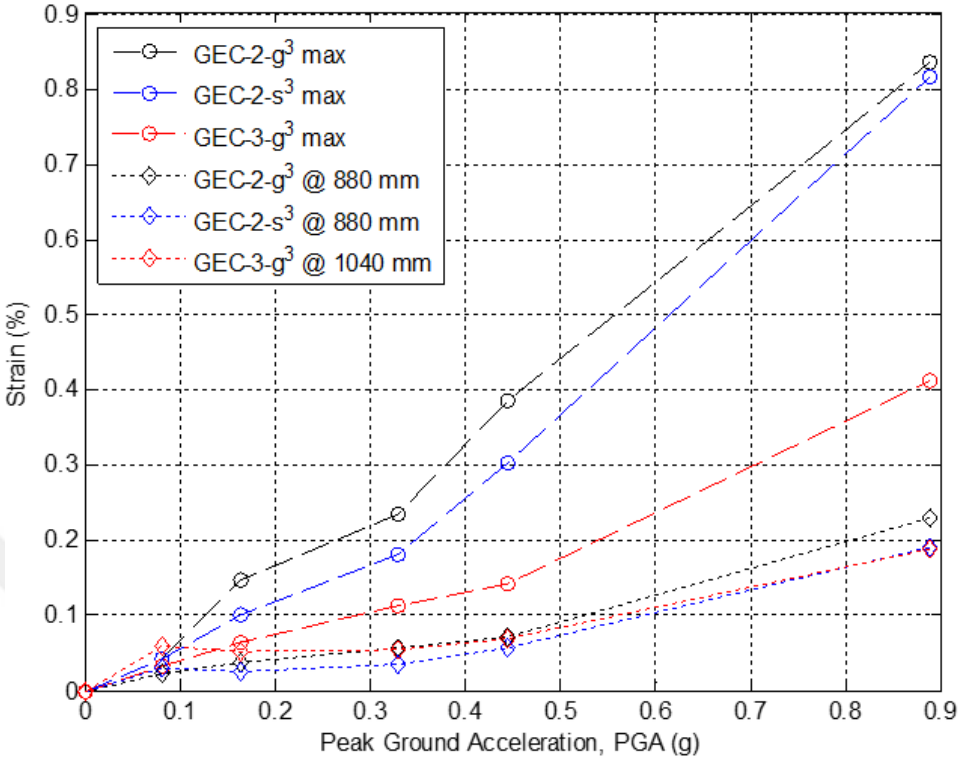

Figure 6.18. Various photographs pertaining to the surcharge loading and laser displacement sensors, and column load test setup.

The strain gauges affixed to the geosynthetic reinforcements were also made use of during the course of the column load tests. Since columns reinforced with GT1 are considered to be ordinary stone columns, the stress-strain behavior of these columns will not be analyzed any further. Some of the strain gauges attached to those columns had exhausted their measuring capability by the end of the dynamic load cases applied. The strain gauges attached had a maximum measurement range of up to 3% strain. The trend of the strains occurring on GT1 material, was of plastic nature and therefore the capacity of the gauges were mostly exhausted.

The horizontal strain components during the course of the column loading tests that occurred on GEC-2-s^3 are illustrated in Figure 6.20. In Figure 6.20, it is seen that the column bulging is more pronounced for depths of 80 and 240 mm. The horizontal strains are decreasing with depth and at a depth of about 720 mm from the column head plane the horizontal strains become smaller than 0.5%. The strain response

after 1690^{th} second of the load test pertains to the unloading-reloading phase of the experiment.

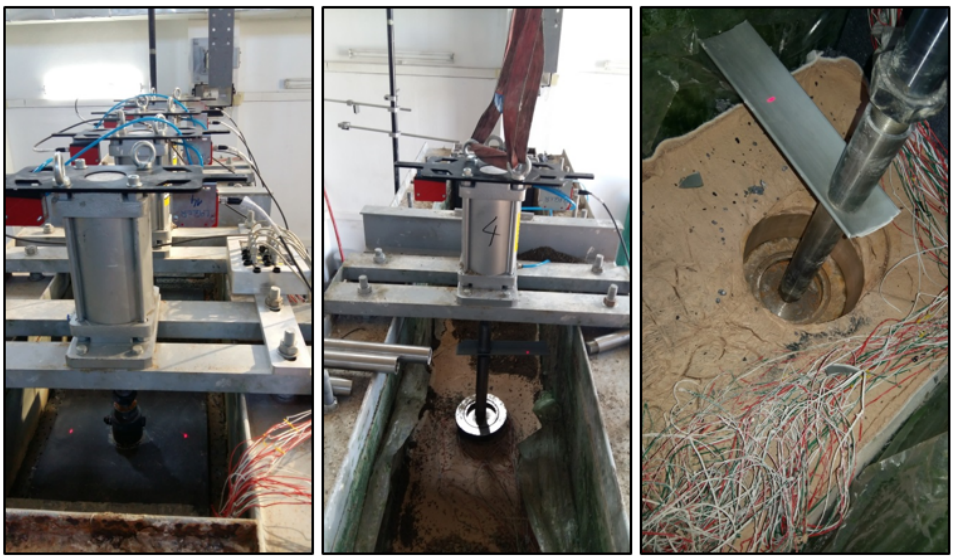

Figure 6.19. Various photographs pertaining to the exhumed columns.

Upon unloading and reloading the column, it is seen that the lateral strain demand to resist the vertical loads is somewhat reduced and the strain in the 80 and 240 mm depth from the column head plane is significantly reduced. The hoop (horizontal or lateral) strain response plots for GEC-2-g^3 and GEC-3-g^3 columns are illustrated in Figure 6.21 and Figure 6.22, respectively.

Figure 6.20. Horizontal strain response of GEC-2-s^3 during column load tests.

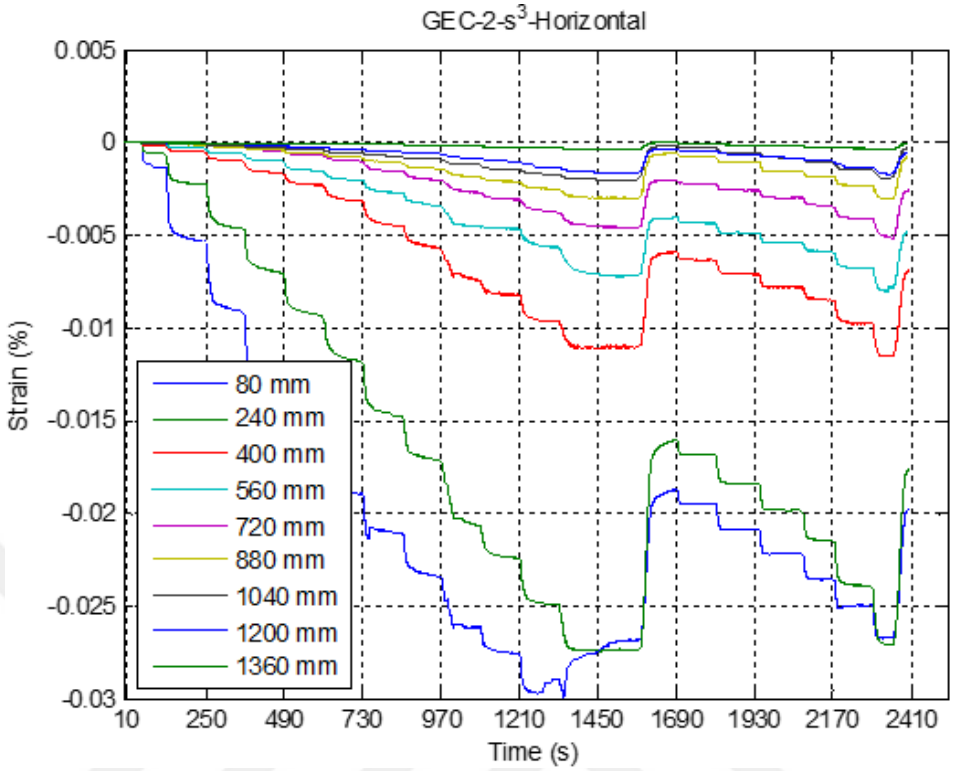

Figure 6.21. Vertical strain response of GEC-2-s^3 during column load tests.

Similar to the behavior of GEC-2-s^3, the horizontal strain behavior of GEC-2-g^3 at the top two instrumentation levels at depths of 80 and 240 mm exhibit the highest lateral strain demand. Upon unloading and reloading, the strain demand on the 240 mm deep instrumentation level exceeded that of the 80 mm. the probable cause of this is the densification of the gravel which consequently pushed the bulging depth to 240 mm. The general trend of the strain read-out data is "shakier" and it is thought that this is due to the rearrangement of the gravel particles that are in GEC-2-g^3. In the sand infilled GEC-2-s^3 column, the strain response is smoother for all instrumentation levels. The strain response of GEC-3-g^3, illustrated in Figure 6.22 shows that the column bulging took place at a depth of 400 mm. It can be said that the stiffer reinforcement geotextile prevented the bulging of the column at the top portion and hence the bulging depth shifted down the lower portions of the column. The maximum hoop strains that were measured in GEC-2-s^3, GEC-2-g^3, and GEC-3-g^3 were 3, 2.7, and 1.2%, respectively.

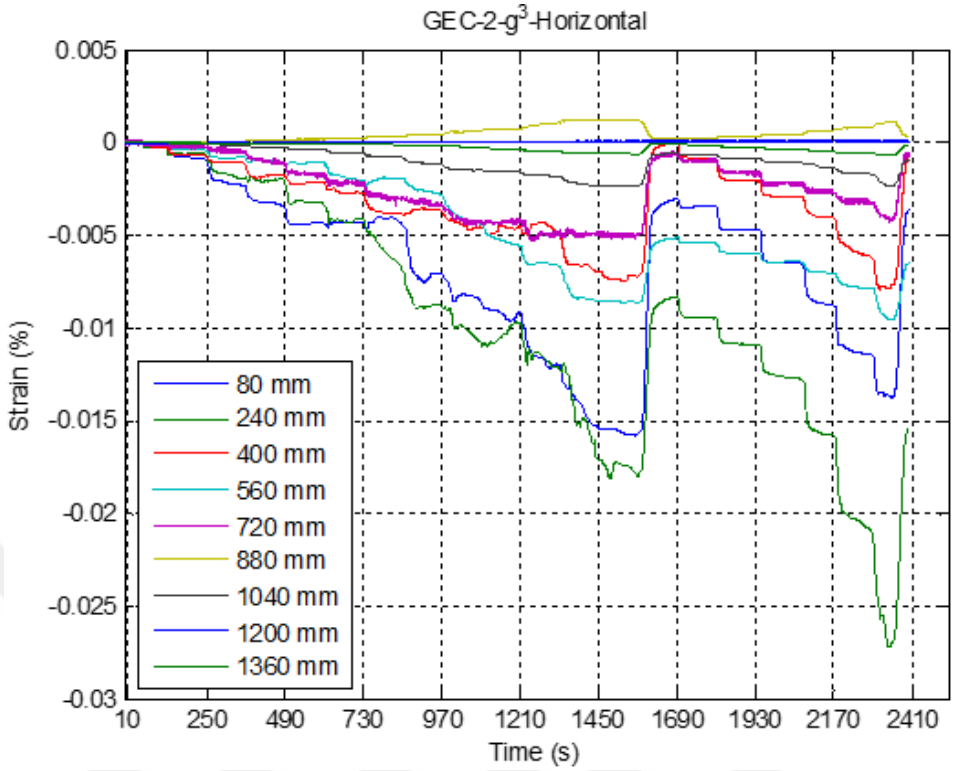

Figure 6.22. Horizontal strain response of GEC-2-g^3 during column load tests.

The vertical strain response of the GEC-2-s^3, GEC-2-g^3, and GEC-3-g^3 are illustrated in Figure 6.23, Figure 6.24, and Figure 6.25, respectively. The vertical strain response of the columns shed light into the bulging behavior of the columns. In the currently available literature, the vertical component of strains under the action of vertical loading has not been considered. Since it is thought that the primary mechanism of column failure for bulging, only the reinforcement strains that prevent bulging are considered in the literature so far. By examining the change of trend of the vertical strain behavior, the shifting of the bulging zone as the column is loaded (and consequently shortened) can he observed. In Figure 6.23, the response of the reinforcement at a depth of 400 mm is changing its trend as the column is loaded. Initially, the vertical strain response of the reinforcement at a depth of 1040 mm is at tension while the reinforcement at the rest of the instrumentation levels are in compression. The response of the reinforcement at a depth of 400 mm however, changes trend and into 730 seconds of vertical loading (around 150 kPa vertical pressure), the trend shifts form compressive to tensile. A similar shift in trend of the vertical strains are observed for

GEC-3-g^3 at depths of 80 and 400 mm.

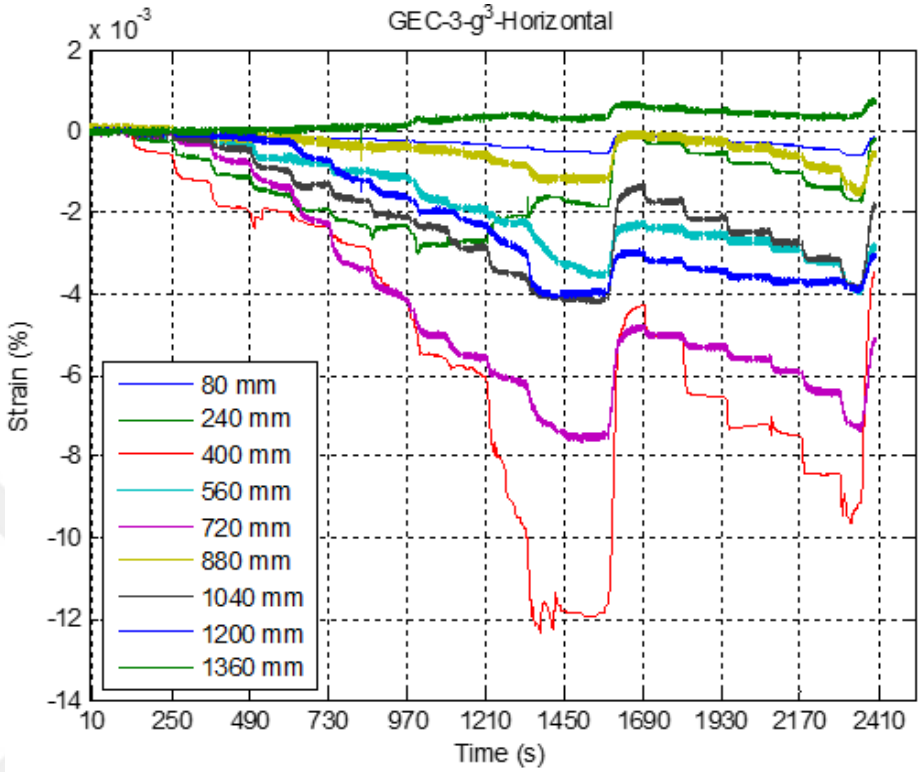

Figure 6.23. Vertical strain response of GEC-2-g^3 during column load tests.

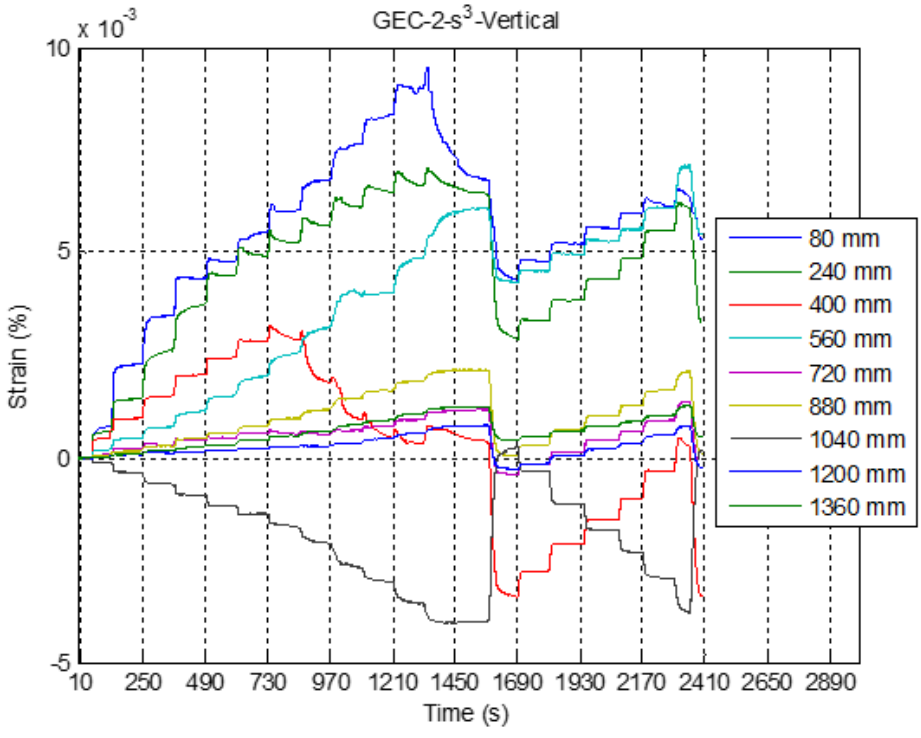

Figure 6.24. Horizontal strain response of GEC-2-g^3 during column load tests.

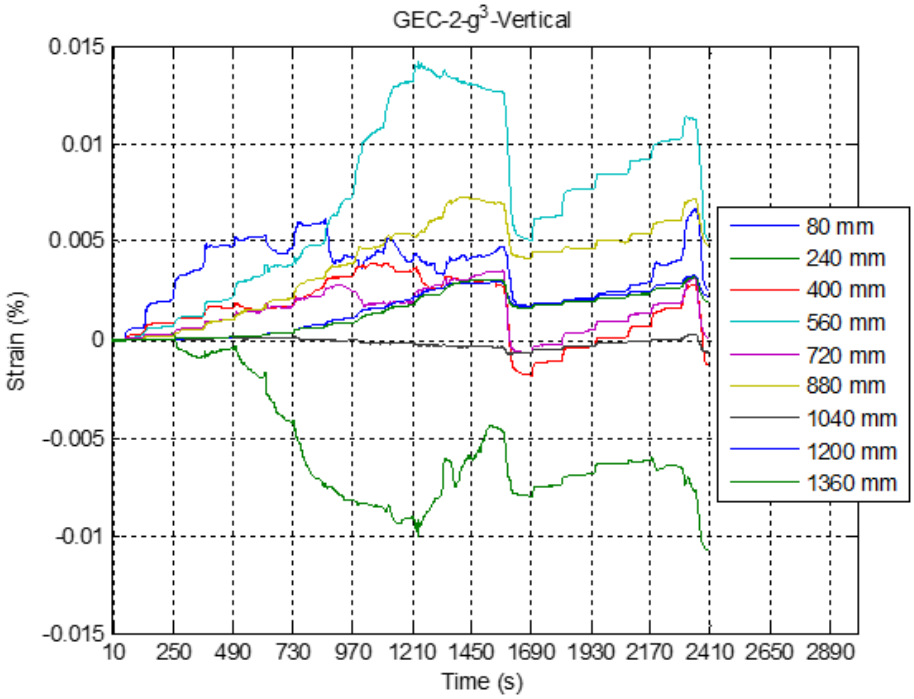

Figure 6.25. Vertical strain response of GEC-3-g^3 during column load tests.

The change in the vertical strain response is due to the downwards shift of the bulging zone and when the bulging zone's maximum curvature point coincides with the instrumentation zone, the vertical loading which should result in compressive vertical strains, starts to induce tensile strains. Since the instrumentation level is at the highest curvature bulging zone, a further increase in loading causes vertically oriented tensile strains to occur at that particular instrumentation zone. Figure 6.26 depicts the peak horizontal strains that occurred in the instrumentation levels during the column load tests. As can be seen in Figure 6.26, the column encased with stiffer reinforcement (GEC-3-g^3) experienced the least amount of tensile strains with a very limited difference between the maximum horizontal strain in the bulge zone to the rest of the strain readings. The stiffer material did not exhibit a pronounced zone of failure or bulging but instead the bulging is spread through the entire height of the column. The rest of the columns behaved in similar way exhibit compatible levels of lateral strain. The overall behaviors of gravel infilled columns of different reinforcement stiffness were also similar with local maximum zones of lateral strains occurring through the height of the column. In sand infilled column however, the strain increased successively towards the

column head plane.

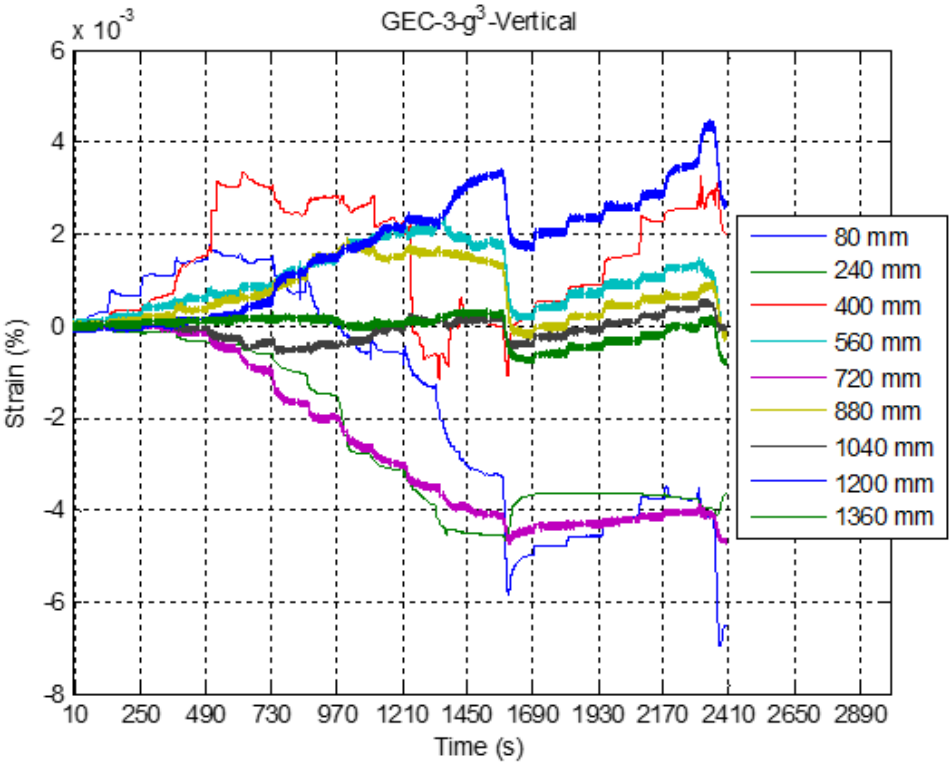

Figure 6.26. Maximum lateral strain response of the columns tested in Setup 3 under static vertical loads.

In Figure 6.27, the settlement versus loading time curves for the columns tested in Setup 3 are illustrated. The gravel infilled GEC-2-g^3 and GEC-3-g^3 columns experienced the least settlements with the GEC-3-g^3 settling about 55 mm at the end of the first loading cycle. Upon unloading and reloading GEC-3-g^3 settled by an additional 6 mm which equates the total settlement by the end of the tests to 60 mm. It is readily seen that the stiffer geotextile reinforcements decreased the settlements of the column in the vertical column load tests as well. GEC-2-g^3 and GEC-2-g^3 settled by 68 and 73 mm by the end of the first cycle of loading, respectively. Upon unloading and reloading, the final settlements of these columns became 71 mm for both columns. The end bearing ordinary stone column OSC-g^3 settled by 132 and 140 mm at the end of the first and second loading cycles.

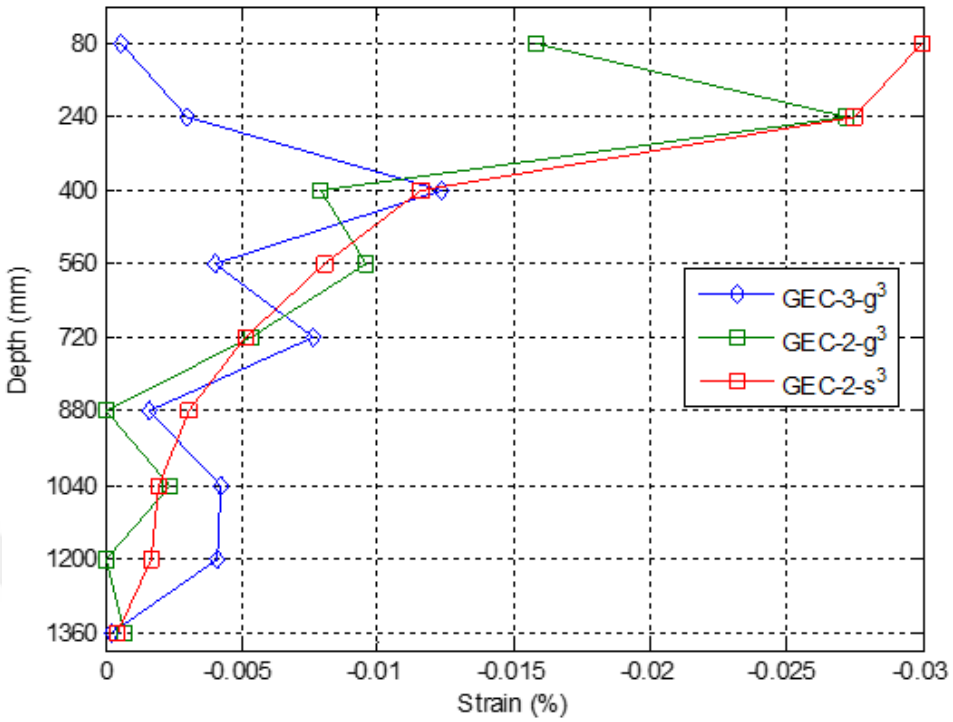

Figure 6.27. Settlement vs. time plots for the columns tested in Setup 3.

Figure 6.28 shows the results from stress-controlled vertical load tests of all columns (columns tested in Setup 1, 2, and 3) and the clay beds after the seismic excitations phase. The data illustrated in Figure 6.28 pertain only to the first cycle of loading and it does not illustrate the unloading-reloading portion of the data. The difference in pressure-settlement behavior of ordinary columns and columns reinforced with GT1 is not significant. It could be assumed that GT1 offered very little confinement effect and thusly including GT1 as a holding medium for strain rosettes did not introduce significant error to the assumption that columns reinforced with GT1 are in fact ordinary stone columns. GEC-3-g^3 experienced a maximum settlement value of about 55 mm at the end of the stress controlled loading phase. GEC-2-s^3 and GEC-2-g^3 experienced larger maximum settlements of 73 and 68 mm, respectively. It is seen that among the columns reinforced with GT2 the gravel infilled GEC-2-g^3 performed slightly better than sand infilled GEC-2-s^3.

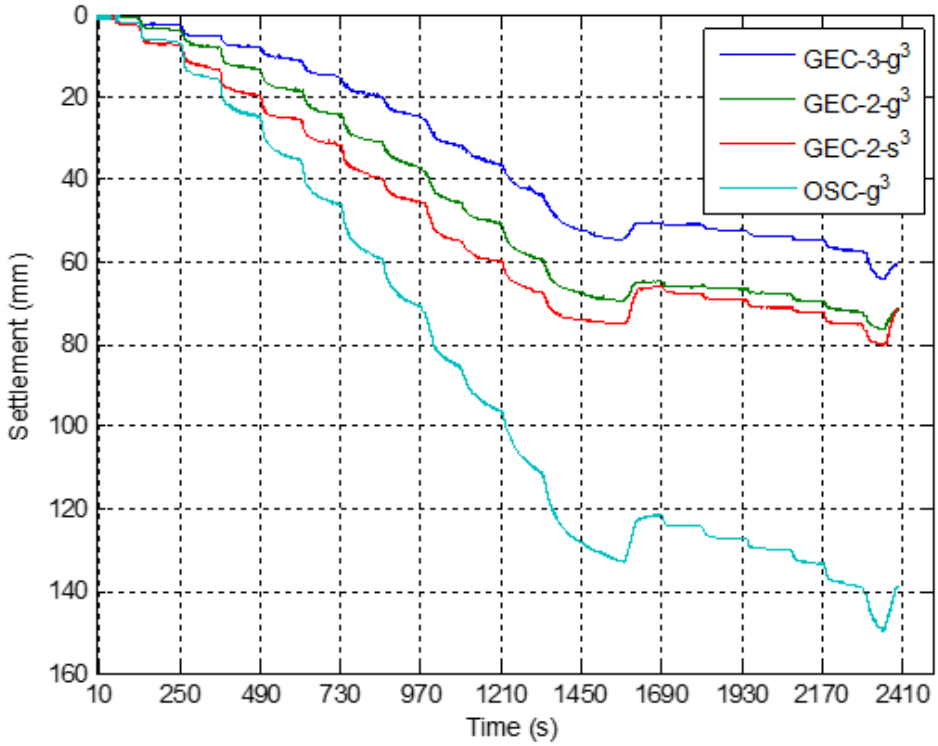

Figure 6.28. Results of stress controlled column tests .

6.5.1. Conclusions

This paper examined the seismic response and post-seismic action bearing capacity characteristics of geosynthetic encased columns and ordinary columns by making use of 1-g model tests. The following conclusions are drawn:

(i) In general, unit cells with end bearing columns have reduced the settlements during earthquake loading compared to floating OSCs. It is also seen that gravel infill reduced the settlements during the earthquake more effectively than sand infill.

(ii) While columns reinforced with GT2 have exhibited distinct maximum straining zones under seismic impact, the column reinforced with GT3 deformed in many locations with smaller amplitude of strains, say more evenly. Similar deformation behavior is also noted in the literature in static load tests of high modulus GECs where bulging does not occur and the lateral deformation along the height of the

column is roughly uniform.

(iii) The magnitude of the seismically induced horizontal strains on GECs varies depending on the encasement stiffness. For the infill materials sand and gravel similar order of magnitude of strains was observed. The encasement strains are seen to be as high as 0.5%. These magnitudes are large enough to be considered as an important factor in the design of foundations supported with GECs under earthquake loading conditions.

(iv) A large strain demand is found to affect GECs of medium reinforcement modulus at a depth of 5 to 7 D from the column head. The depth of this large strain demand zone is deeper than the accepted partial reinforcement depth in published research. It should be pointed out that in design of GECs in seismically active zones, partial reinforcement should be undertaken with caution.

(v) An almost linear relationship between the seismic input energy, expressed in terms of Arias Intensity, and reinforcement strain is observed. Further study is needed in order to come up with comprehensive design charts. Authors believe that the current study will spearhead such an effort.

(vi) Stress controlled vertical loading tests conducted after seismic loading revealed that the behavior of the columns confined with GT1 was close to that of the ordinary columns. However it was shown that the settlements of columns during seismic excitation, confined with GT1, are less than those of ordinary columns. The low modulus geotextile GT1 experienced significant strains under the action of induced seismic loads and aided in reducing settlement not necessarily by the confinement effect but rather by holding the column constituents intact during the seismic loading.

6.5.2. Discussion

The response of the soil-geotextile is both rate and stress history dependent. The time window in which the seismic energy is transferred to the system is important because it will control the deformation behavior. The constitutive model for geosynthetics is based bounding surface plasticity and overstress viscoplasticity, in which the

total strain rate is assumed to be composed of the following three components:

$$\dot{\varepsilon} = \dot{\varepsilon}^e + \dot{\varepsilon}^p + \dot{\varepsilon}^{vp} \tag{6.2}$$

Where $\dot{\varepsilon}^e$, $\dot{\varepsilon}^p$ and $\dot{\varepsilon}^{vp}$ are elastic, plastic and viscoplastic strain rates. It is known that the behavior of geosynthetics is strain-rate dependent. Considering the presented results it could be intuitively inferred that a sufficiently long duration sinusoidal accelerogram will not yield similar results. The calculated cumulative input energy due to sinusoidal loading will continuously increase in time domain but the amplitude of strain will not increase linearly with increasing energy. This is because of the stress history effect. There is a coupled action between soil mass and the reinforcement. Amplitude wise repetitive sinusoidal loading will not impose further displacement in the soil body thereby not forcing geotextile to deform. This is why there will not be linear correlation between IA and strain under sinusoidal loading. This is why this correlation works the best with real EQ records where the peak loading occurs once and material is virgin to such loading in its loading history.

7. LAMINAR BOX RESULTS

The results discussed in this section of the dissertation is based on the materials that are intended to be published by the Geotextiles and Geomembranes journal in a two-part-work tentatively titled "On the Performance and Behavior of Soft Clay Beds Enhanced with Geosynthetic Encased Columns Subjected to Dynamic Loads: Part 1 Response of the Columns" and "On the Performance and Behavior of Soft Clay Beds Enhanced with Geosynthetic Encased Columns Subjected to Dynamic Loads: Part 2 Response of the Embankment and Subsoil" with authors Cihan Cengiz and Erol Güler. The dissertation author is the first author in both of the above mentioned papers.

Laminar box assembly was produced to mimic the free-field response of a soil element that is subjected to dynamic base excitations. The boundaries of the box are designed to be unyielding under the action of the dynamic base excitations. The laminates of the laminar box are designed so that their inertia has minimal effect on the behavior of the contained soil specimen. The free-field behavior of the contained soil and the column constituents are studied in the laminar box assembly. The laminar box houses four 136 mm diameter columns with a height of 1350 mm which equates the height to diameter ratio of the model columns to roughly 10. Each granular column is installed in a unit cell that is 450 mm by 450 mm. The area replacement ratio is 7%.

The tests are divided in two major groups according to the nature of the input excitations applied to the experimental setup. The first group of the tests is designated as the Sinusoidal Excitation Scheme and the second group is designated as the Earthquake Excitation Scheme. The details pertaining to the excitation schemes are tabulated in Table 5.3 and Table 5.4. Table 5.5 gives an account of the undertaken tests and the presence of the column treatments for each test. The model designations given in this part of the dissertation refer to the model names tabulated in Table 5.5.

7.1. Displacement of the Soil Profile

The displacement response of the model soil layer is important for the design scenarios where lifelines and infrastructure may be present within or above the soft soil. For example, the maximum and residual displacement of the soil profile may be an important indicator of the serviceability of a railroad embankment after the embankment is subjected to seismic loading. The displacement response also paves the road for comparison of the relative stiffnesses of the soft soil profiles that are treated with different column details and configurations. The shear strains developing inside the soil layer are also calculated based on the measured displacement response.

The displacement measurements of the laminates were taken by laser displacement sensors at mid-height of the laminates. Therefore, while the displacement measurements taken at a depth of 50 mm reflect the behavior of the topmost laminate, the measurements taken at a depth of 1550 mm pertain to the bottommost or 16^{th} laminate layer. Figure 7.1 illustrates the displacement response of the laminates to 0.5 Hz load case that is applied in the Sinusoidal Excitation Scheme to Model 1 (benchmark untreated clay bed as per Table 5.5). In Figure 7.1, the displacement responses of all 16 laminate layers are illustrated. The data is collected for a duration of 100 seconds in each test and the plots in Figure 7.1 only include the displacement data from 10 to 70 seconds.

In Figure 7.2, the positions of the laminates at the onset of the 0.5 Hz load case (for 20, 20.5, 20.7, 20.8, 21, and 21.2 seconds) are given. The curves pertaining to different time values are representative of the horizontal positions of each laminate measured at that particular time instance. While the plots of the laminate positions at a given time instance is of interest, the maximum displacement recorded in each laminate under the action of various input excitations shed light into the extent to which the soil deforms. The maximum lateral displacements of all the models tested in Sinusoidal Excitation Scheme are illustrated in Figure 7.3, Figure 7.4, and Figure 7.5.

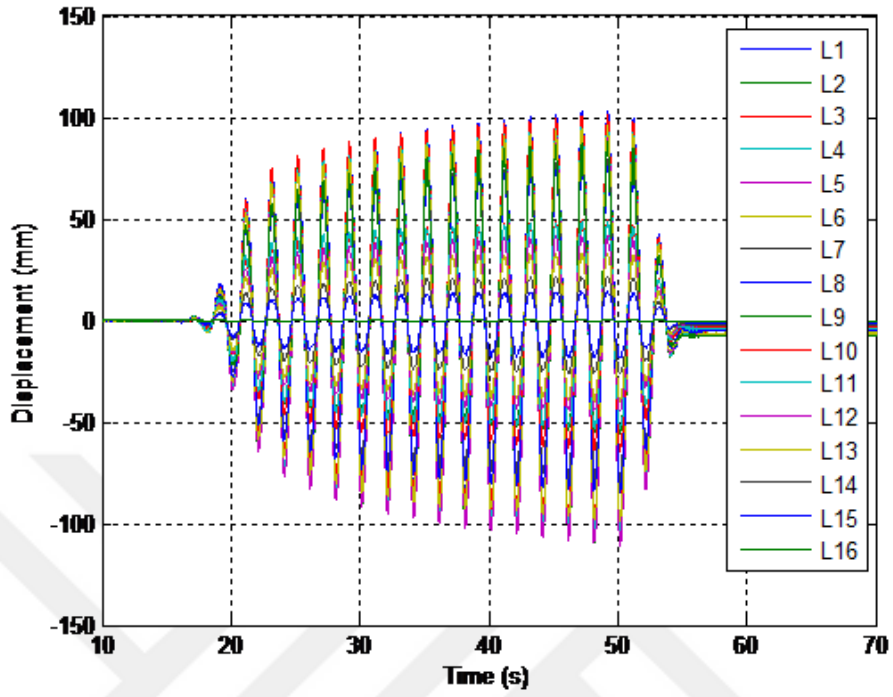

Figure 7.1. Displacement responses of the laminates under 0.5 Hz load case.

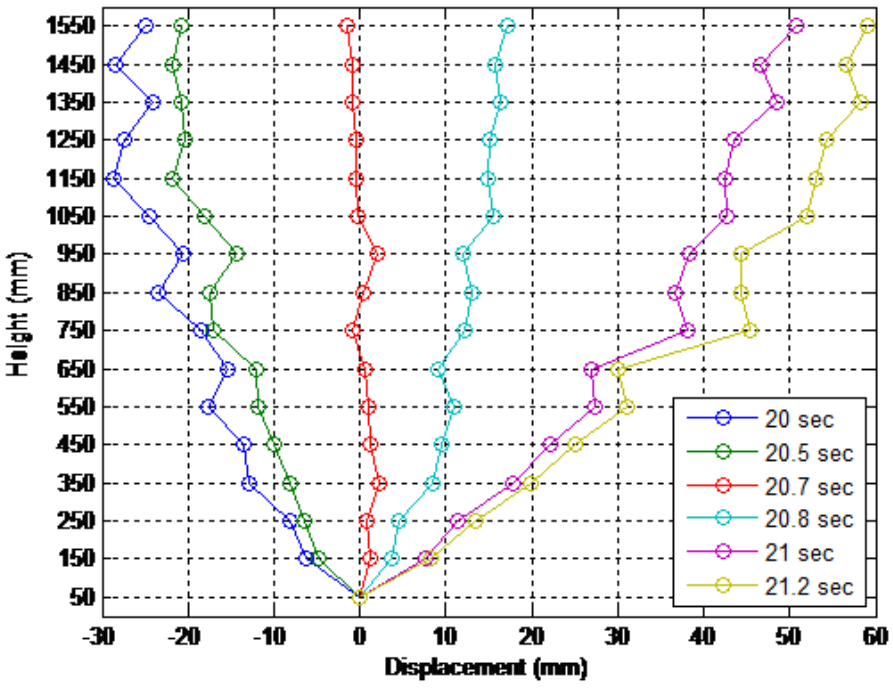

Figure 7.2. The positions of the laminates at the onset of 0.5 Hz load case.

In Figure 7.3, the maximum displacement of the soil profiles under the action of Sweep-1, 0.5 Hz and 1 Hz load case are illustrated. 0.5 Hz load case caused a remarkably high displacement of the soil profile for the untreated clay bed. The topmost laminate displacement for the untreated clay bed was about 100 mm. The OSC treated clay bed experienced less lateral movement as opposed to the untreated clay bed with a topmost laminate displacement of about 90 mm. The GEC treated clay beds experienced the least lateral movements with the maximum lateral movements at the top of the soil profile being less than the half of the displacements experienced by the untreated clay bed for both models. With increasing loading frequency, the difference in the maximum displacement plots of the untreated clay bed its column treated counterparts becomes less pronounced. Under the action of 1 Hz load case, the overall trend of maximum lateral displacement is the largest for the OSC treated clay bed followed by the untreated clay bed. GEC enhanced clay beds had a topmost maximum laminate displacement of 57 and 83 for reinforcement stiffnesses of 1000 and 400 kN/m, respectively. The OSC treated clay bed and benchmark clay bed had topmost laminate displacements of 94 and 91 mm. It is seen that GEC enhancement has significantly reduced the displacement of the soil profile under the action of the applied sinusoidal load cases with frequencies of 0.5 Hz and 1 Hz. The beneficial effects of GEC inclusions under the action of Sweep signal (Sweep-1 signal) however is not readily seen. The probable cause of this is the fact that the Sweep-1 signal has a varying frequency content. The signal has a frequency range of 1 to 15 Hz and in this frequency window covers the resonant frequency range of all of the tested soil profiles. It is thought that the signal caused resonance in all soil profiles tested and given the low amplitude of the signal, the maximum displacements of about 70-90 mm were observed for the top level of the soil profiles.

In Figure 7.4, the maximum displacement plots pertaining to 1.5, 2, and 3 Hz load cases are illustrated. Although GEC inclusion seems to limit the lateral deformations of the soil body to a certain extent, another benefit of GEC inclusions becomes evident from the maximum displacement traces presented. The untreated clay bed and the OSC treated clay bed exhibits almost no movement at the bottommost laminate level which is at a depth of 1550 mm in the results depicted in Figure 7.3, Figure 7.4, and

Figure 7.5.

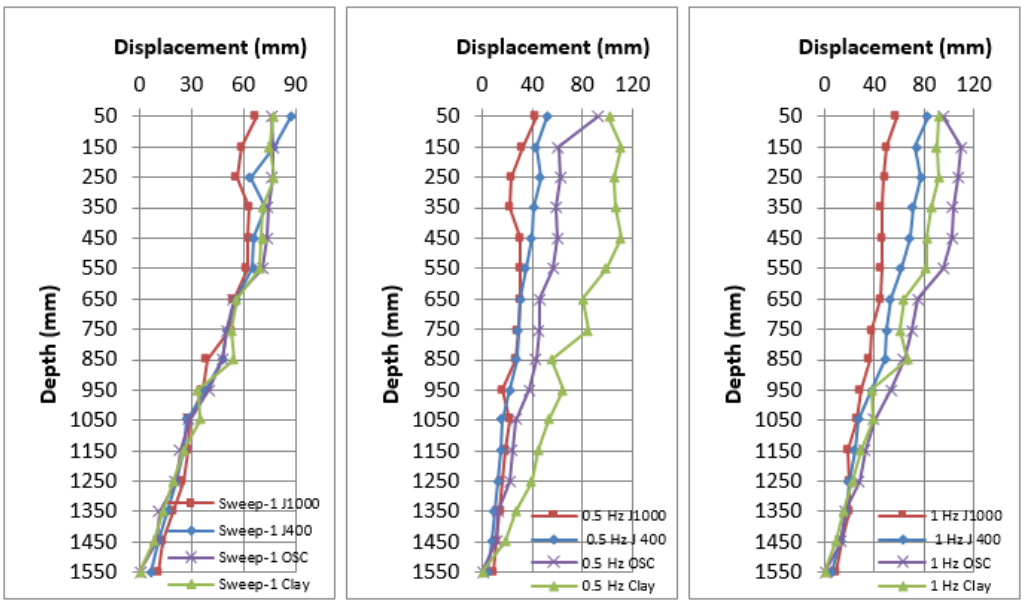

Figure 7.3. Maximum recorded displacements of the laminates for Sweep-1, 0.5 Hz, and 1 Hz load cases.

It is believed that the presence of GECs holds the soft soil it is embedded to as a coherent body and under the action of applied input excitations, the soft soil exhibits a block movement type displacement response. Since the bottom laminate moves alongside with the upper layers, the relative displacements of the soil layers and consequently the corresponding shear strains occurring within the soil body is significantly reduced. The maximum displacement responses depicted in Figure 73 also further reinforces the above specified hypothesis about the presence of GECs holding the soil as a coherent body. The bottommost layer displacement is designated as the base drift and this could be clearly seen in the plots of the maximum displacements in Figure 7.4 for 3 Hz load case and in Figure 7.5 for 5 Hz load case.

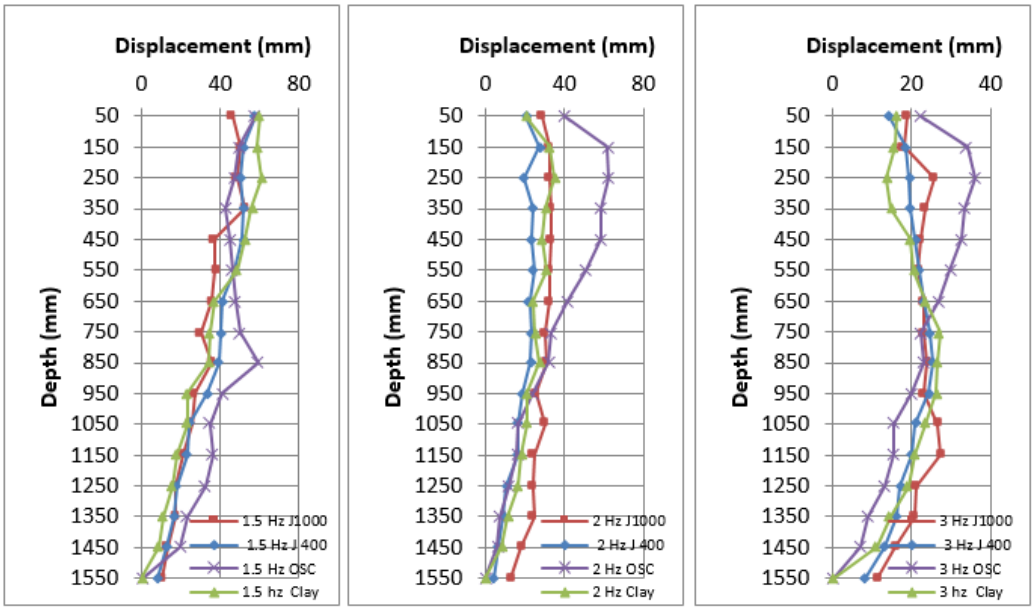

Figure 7.4. Maximum recorded displacements of the laminates for 1.5, 2, and 3 Hz load cases.

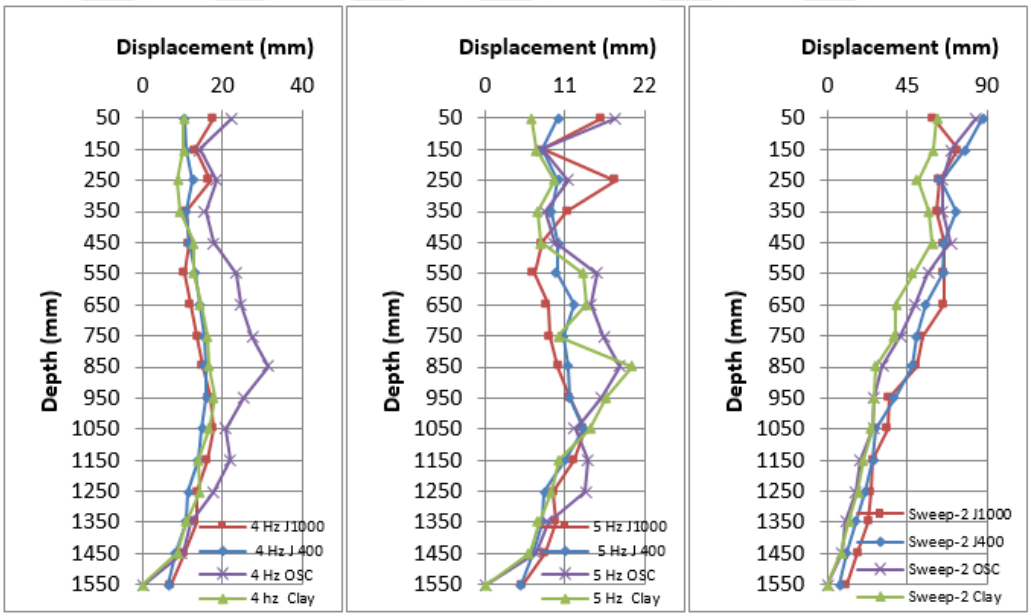

Figure 7.5. Maximum recorded displacements of the laminates for 4 Hz, 5 Hz, and Sweep-2 load cases.

In order to study the base drift occurring in the models that are subjected to Sinusoidal Excitation Scheme (as per Table 7.1), a plot of the base drift as a function of the loading frequency is given in Figure 7.6. It is seen that the GEC treated soft

clay beds experienced significant base drift displacements.

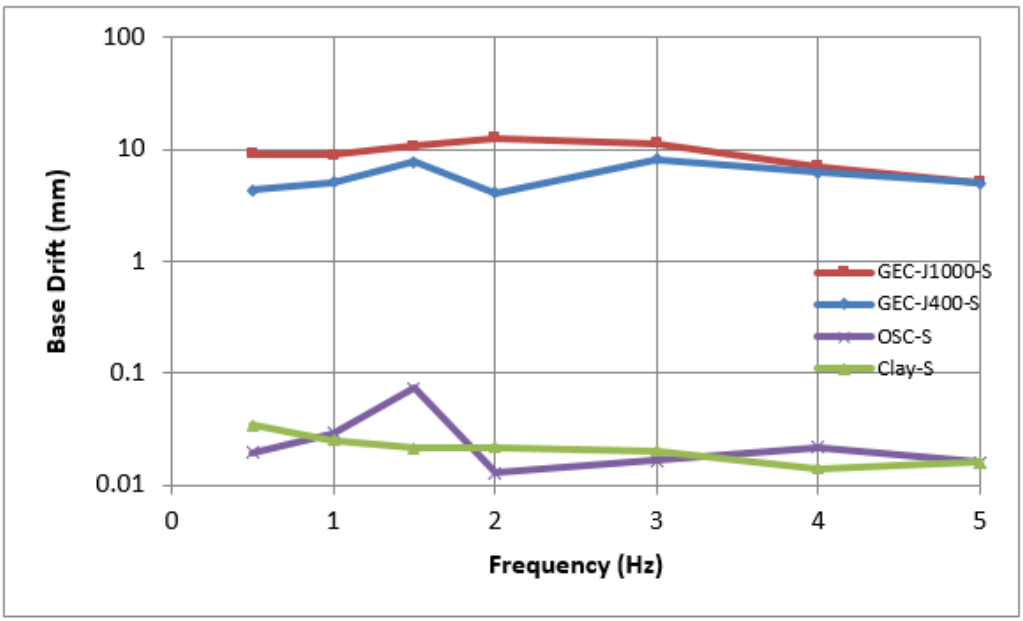

Figure 7.6. Base drift for the models as a function of the loading frequency.

The average and maximum displacement (calculated relative to laminate # 16) of the soil columns under various sinusoidal loading frequencies is illustrated in Figure 7.7a and Figure 7.7b, respectively. It is seen that ordinary stone column treated clay bed (OSC-S) has experienced a higher average lateral displacement that the rest of the test sections with the exception of the 0.5 Hz loading case. During 0.5 Hz load case, both the average and maximum displacement values were the highest for untreated clay bed (Clay-S). Test clay bed treated with four GECs with a reinforcement stiffness of 1000 kN/m (GEC-J1000-S) experienced the lowest average and maximum laminate displacements for almost all loading frequencies. It is seen that the general trend of average and maximum displacements for GEC-J400-S (clay bed treated with four GECs with a reinforcement stiffness of 400 kN/m) and GEC-J1000-S are very similar, with GEC-J400-S having larger displacement values for load cases with frequencies lower than 2 Hz. Under studied conditions, increase in GEC reinforcement stiffness from 400 kN/m to 1000 kN/m did not further limit the average and maximum lateral displacements of the laminates for loading frequencies greater than 2 Hz. It is also seen that the peak displacement values are achieved for all test sections with column

inclusions at 1 Hz load case.

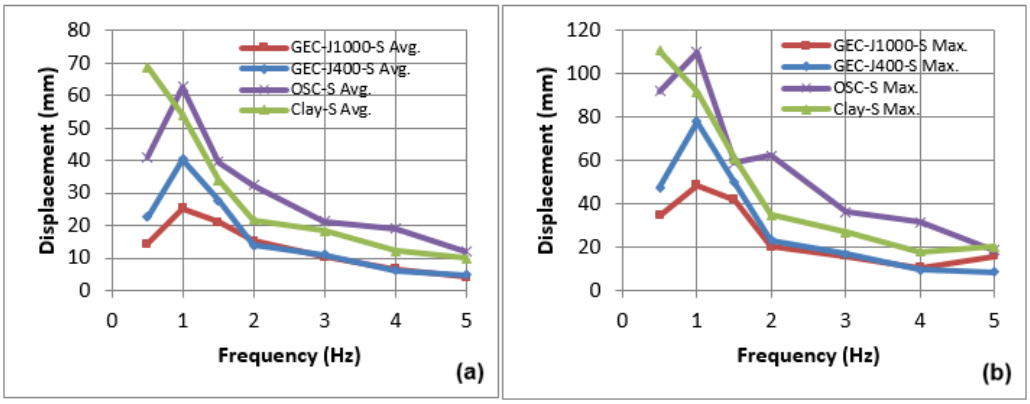

Figure 7.7. (a) The average and (b) maximum laminate displacements under the action of sinusoidal loads with varying frequencies.

Figure 7.8 shows the maximum laminate (soil) displacements for the models subjected to 25, 50, and 100% El-Centro load cases tested in Earthquake Excitation Scheme. In Figure 7.8(a) the maximum displacement values of the model soil profiles subjected to 25% El-Centro accelerogram are given. Under the applied loading the model soil profiles' maximum lateral deformation behavior is almost identical with the maximum lateral displacement value generally lower than 10 mm. Under 50% El-Centro loading (in Figure 7.8b), the encased column's beneficial effects in reducing lateral displacement of the soil profile becomes more evident. In Figure 7.8(c), under the action of 100% El-Centro load case, GEC enhanced soil models, GEC-J1000-EQ (model 8) and GEC-J400-EQ (model 7), have undergone maximum top laminate displacements of 55 and 62 mm, respectively. The OSC installed clay bed (OSC-EQ, model 6) and untreated clay bed (Clay-EQ, model 5) have undergone 60 and 74 mm maximum top laminate displacements. Figure 7.9 shows the maximum laminate displacements for the models subjected to 50 and 100% Kobe load cases tested in Earthquake Excitation Scheme. The maximum top laminate displacements under the action of 50% Kobe load case depicted in Figure 7.9(a) for GEC-J1000-EQ, GEC-J400-EQ, OSC-EQ, and Clay-EQ were 85, 110, 124, and 147 mm, respectively. The maximum top laminate displacements under the action of 100% Kobe load case depicted in Figure 7.9(b) for GEC-J1000-EQ, GEC-J400-EQ, OSC-EQ, and Clay-EQ were 110, 131, 165, and 196

mm, respectively. The topmost displacement values indicate that the GEC enhanced clay beds have undergone significantly lower top laminate displacements. Under the action of 100% Kobe load case, maximum lateral displacement for GEC-J1000-EQ is almost half the maximum displacement experienced by Clay-EQ.

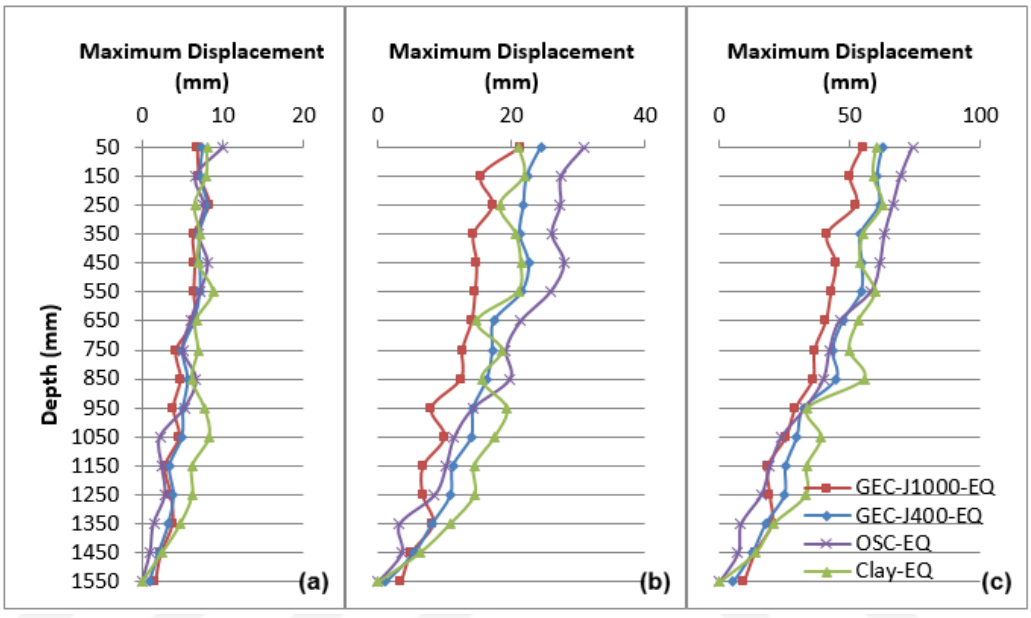

Figure 7.8. Peak displacement plots for (a) 25% , (b) 50% , and (c) 100% El-Centro load case.

Figure 7.10 depicts the top laminate displacements as a function of the peak ground acceleration (PGA) of the applied load cases. It is seen that the untreated clay bed exhibited the highest top level displacement values for almost all load cases. With granular column addition, the displacements were somewhat decreased and by installation of GECs the top level displacement was significantly reduced. It is seen that higher reinforcement stiffness yielded lower top level displacements, as well. In Figure 7.10, a sharp increase in the top displacement is explicitly observed in the transition from PGA values of 0.38 g to 0.41 g (100% amplitude El-Centro and 50% amplitude Kobe load cases). Although the PGA values of the two load cases are of similar magnitude, there is a dramatic increase in the displacement values. Therefore, while PGA is a relevant parameter in quantifying the destructiveness of an earthquake, it should not be relied upon as a sole indicator of the earthquake intensity. Parameters such as the frequency content, cumulative seismic input energy, and energy distribution

pattern of the earthquake should also be considered.

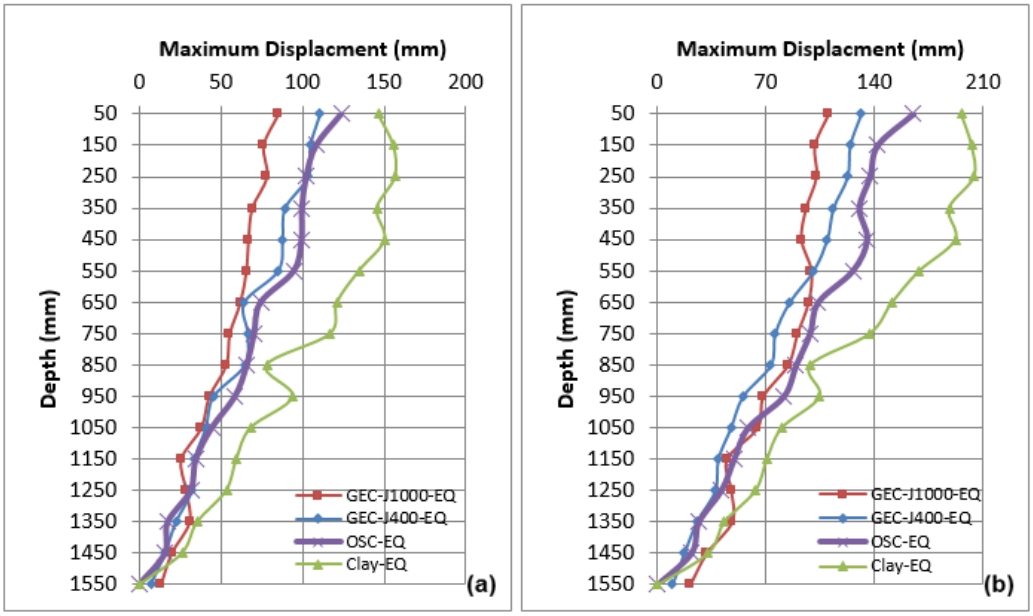

Figure 7.9. Peak displacement plots for (a) 50% and (b) 100% Kobe load case.

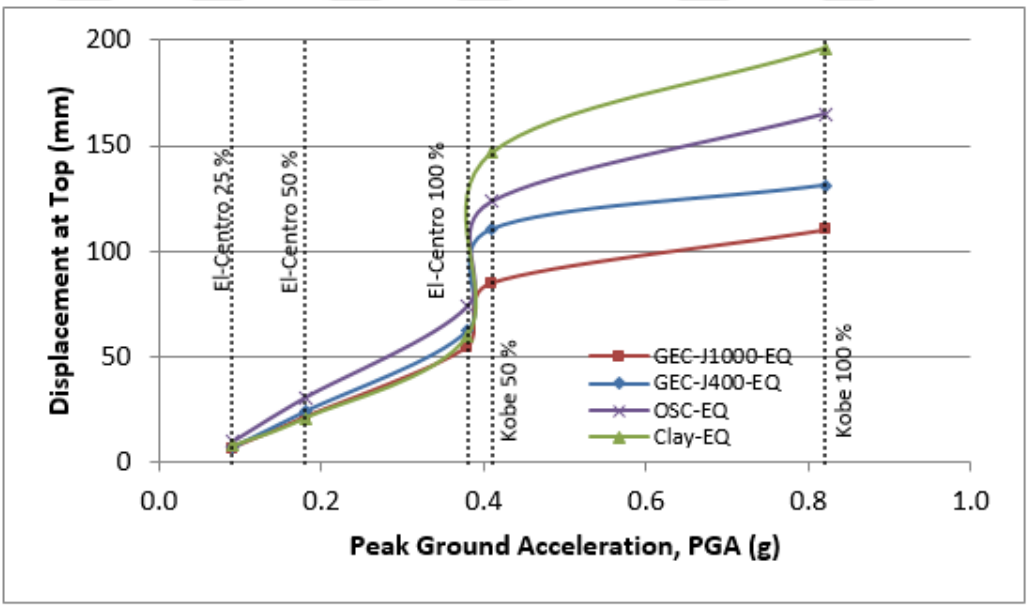

Figure 7.10. Top laminate displacement values for various PGAs recorded in Earthquake Excitation Scheme.

The behavior of GEC installed clay beds could be further studied by comparing the bottommost laminate's lateral movement, designated as base drift in Figure 7.11. In Figure 7.11, the maximum displacement values for the 16^{th} laminate (as per Figure

7.1) at the base of the laminar box as a function of the applied PGAs are given. It is seen that while the GEC enhanced model soils have undergone significant base drift, OSC installed and benchmark clay bed experienced almost no base drift. It could be speculated that the presence of GECs aided in holding the soft clay bed as a coherent body and some block movement of the GEC enhanced clay beds have occurred. Since the bottommost layer displaced with the soil block in GEC-J400-EQ and GEC-J1000-EQ, the relative displacements between the top and bottom of the soft soil is reduced. This in turn causes lower values of shear strains developing over the height of the soft clay bed. Consequently, it could be said that GEC installation reduced both the absolute displacements of the top of the soil profiles and as discussed later, the shear strains developing inside the clay bed. Similar base drift behavior was observed for experimental models enhanced with GECs tested in Sinusoidal Excitation Scheme.

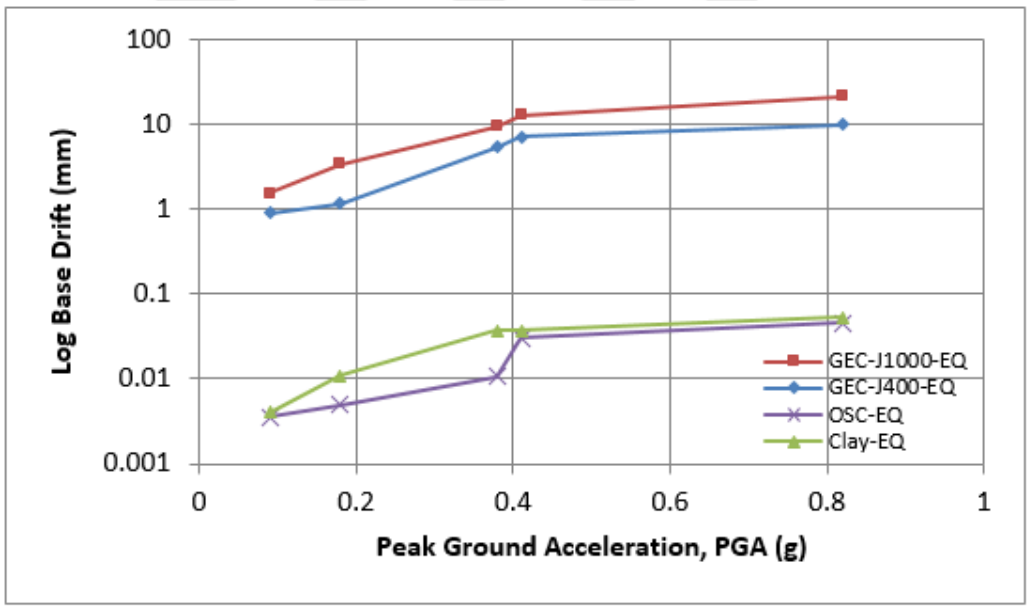

Figure 7.11. Maximum displacement (base drift) of the model soil profiles tested in Earthquake Excitation Scheme.

Top laminate displacement values recorded in Sinusoidal Excitation Scheme are given as a function of loading frequency and peak sinusoidal acceleration in Figure 7.12(a) and Figure 7.12(b), respectively. It is seen that the top laminate displacement of the tested models were most sensitive to a frequency range of 0.5 to 2 Hz. Although the amplitude of the sinusoidal acceleration was increased with increasing loading fre-

quency, higher loading frequencies such as 4 Hz with a peak sinusoidal acceleration of 0.76 g did not evoke high displacement responses in the models tested. The peak acceleration value for both 100% Kobe and 5 Hz sinusoidal load case were in the neighborhood of 0.8 g. The displacements that were brought about by these load cases were vastly different than each other with the maximum top level displacement for the untreated clay beds being close to 200 and 20 mm for 100% Kobe and 5 Hz load case, respectively.

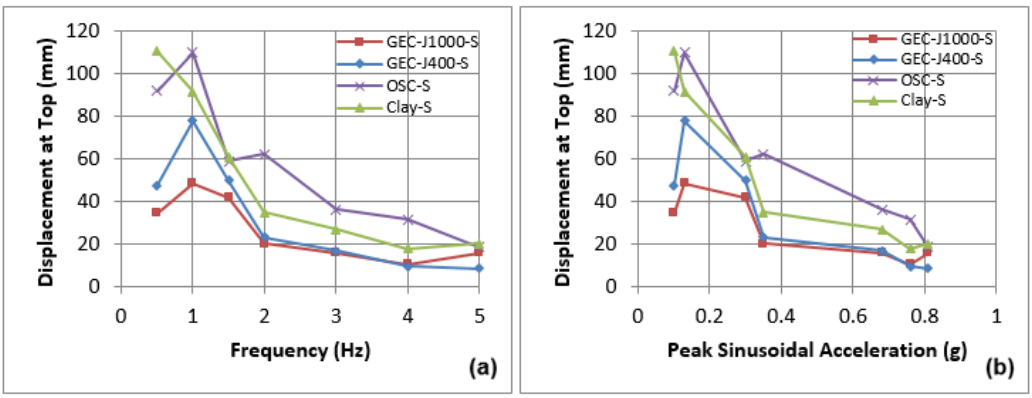

Figure 7.12. Top laminate displacement values for various PGAs recorded in Sinusoidal Excitation Scheme.

Shear strains develop within the soil retained inside the laminar box due to dynamic loading. With the assumption that the shear strain varies linearly in a given layer, the shear strain in the nth layer can be calculated as:

$$\gamma_n = \frac{d_{n+1} - d_n}{H_n} \tag{7.1}$$

where H_n is the thickness of the soil band and $d_{(n+1)}$ and d_n are the horizontal displacements of layers $N + 1$ and N, respectively (Araei and Towhata; 2014). The maximum shear strains caused by Earthquake Excitation Scheme are given in Figure 7.13. It is seen that soft clay bed enhanced with GECs experienced lower values of maximum shear strain. Under the action of 100% Kobe load case, the maximum shear strain in GEC-J1000-EQ and GEC-J400-EQ was about 10 and 12%, respectively. This indicates that increasing reinforcement stiffness decreases the maximum shear strain

amplitude. The magnitude of maximum shear strain in the soil profile enhanced with ordinary stone columns (OSC-EQ) was 14% which was slightly lower than 15% that was calculated for Clay-EQ.

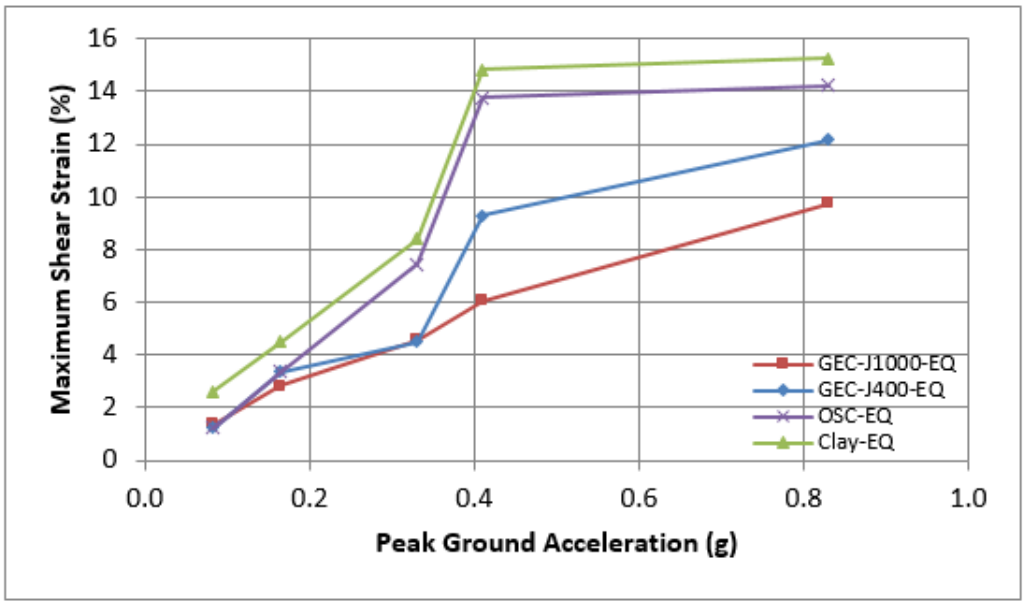

Figure 7.13. Maximum shear strain values for various PGAs.

7.2. Reinforcement Strains

The reinforcement strain responses of the GECs to sinusoidal and simulated earthquake excitations are quantified by strain rosettes. While the strain response to earthquake excitations shed light into the behavior and amplitude and distribution of strains on the GEC in the field conditions, the behavior of the columns under sinusoidal loads of varying frequency provides insight into the behavior of the column at specific dynamic load frequencies.

Geosynthetic material possesses tensile capacity only and hence resists the movements with the help of the tensile strength. However, measurements taken from strain gauges indicate that the nature of the strain relationship in a given instrumentation location is antagonistic and once the material is tensioned in one direction, complementary compressive strains develop in the direction orthogonal to the direction of tensile elongation. While the likely explanation to the occurrence of compressive strains is

Poisson effect, it is thought that since the reinforcement is circular, the compression on one end of the circular cross-section must be countered by tensile strains to satisfy overall force equilibrium in the horizontal (hoop) direction. Therefore, although the measured strains at the instrumentation point are of compressive nature, it could be assumed that tensile strains with equivalent magnitude (to that of the compressive strains) occur in the reinforcement.

Figure 7.14 illustrates the response of the geosynthetic reinforcement embedded in model 4 under the action of 4 Hz load case. The illustrated data pertain to the strain gauge that is placed 850 mm below the column head plane (fifth strain gauge from the top as per Figure 4.12) and the position of the strain gauge is vertically aligned within the zone of 13th laminate. Figure 7.14(a) shows the movement of the 13^{th} laminate under the induced accelerations. In Figure 7.14(b) the vertical and horizontal strain response of the geosynthetic reinforcement in time domain is given. It is clearly seen that the reinforcement responds to the movement of the soil mass. Figure 7.15(a) gives the vertical and horizontal strain loops and Figure 7.15(b) depicts the vertical and horizontal strain components plotted against each other. The strain response depicted in Figure 7.15(b) shows that the tensile vertical strains evoke compressive horizontal strains and vice versa. Similar interplay between vertical and horizontal strain components have been observed for all instrumentation points under earthquake and sinusoidal load cases. It is seen that the antagonistic behavior of the reinforcement is valid both for static and dynamic loading conditions.

The behavior of the reinforcement is also antagonistic under the action of simulated earthquake accelerograms. Figure 7.16 gives the strain behavior of the geotextile encasement at a depth of 100 mm from the column head plane under the action of 100% Kobe load case (GEC-J1000-EQ).

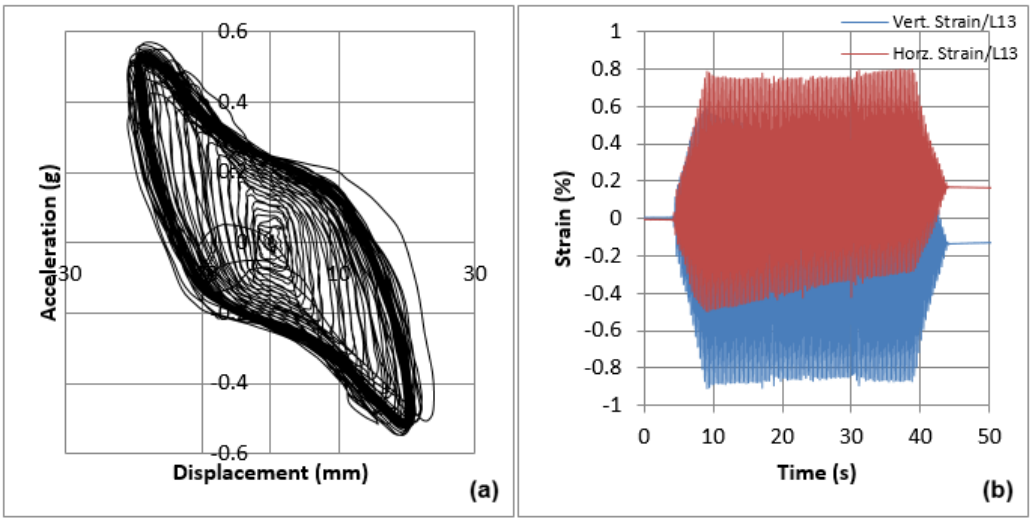

Figure 7.14. Strain response of the GEC embedded in model 4 during 4 Hz load case, at the elevation of 13th laminate (a) acceleration vs. displacement loops, (b) vertical and horizontal strain plots in time domain.

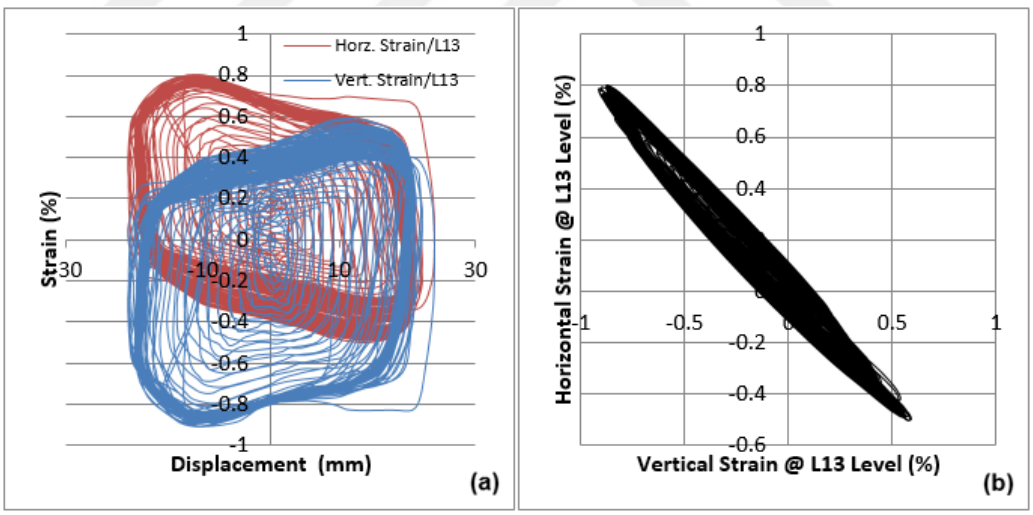

Figure 7.15. Strain response of the GEC embedded in model 4 during 4 Hz load case, at the elevation of 13th laminate (a) displacement vs. strain loops, (b) vertical and horizontal strain plotted against each other.

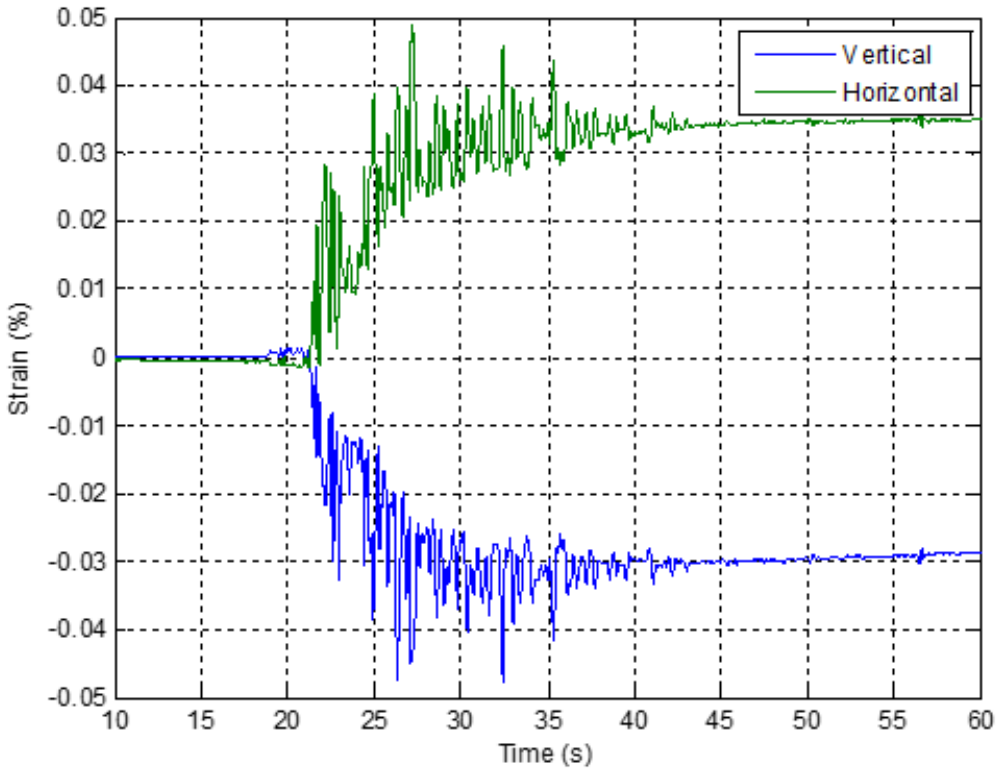

Figure 7.16. Strain response of the GEC-J1000-EQ under 100% El-Centro loading at a depth of 100 mm from column head plane.

The strain response of the reinforcement depicted in Figure 7.16 shows that the response of the reinforcement is antagonistic under the action of the induced seismic loads. The reinforcement response therefore is antagonistic both under static and dynamic loading (both sinusoidal and earthquake accelerograms) scenarios.

Figure 7.17 and Figure 7.18 depict the maximum vertical and horizontal reinforcement strains for the columns embedded in model 3 and model 4, respectively. It is seen that the strain demand brought about by dynamic loading on the reinforcement is distributed to the entire height of the GECs. Moreover, the distribution patterns of maximum strain over the height of the GECs are more or less same. It is seen that there is fewer variations on the maximum strain response of the GEC embedded in model 4 (GEC-J1000-S) with the curve pattern being mostly the same for all sinusoidal load cases. Model 3 is enhanced with GECs reinforced with GT1 whose reinforcement modulus (J) is 400 kN/m. It is seen that 1.5 Hz sinusoidal loading caused

the highest maximum reinforcement values. Under the action of 1.5 Hz loading GT1 has undergone a maximum vertical tensile strain of about 3% in three distinct zones of the column. These zones are at a depth of 1D, 6D, and 8.5D from the column head plane. Maximum horizontal tensile strain that occurs at a depth of 8D is about 1.5%. The location of the maximum horizontal tensile strain coincides with the maximum vertical compression strain whose value is about 3%. The reinforcement modulus in model 4 is 1000 kN/m and the maximum tensile vertical and horizontal strain is about 1.5% and 1%, respectively.

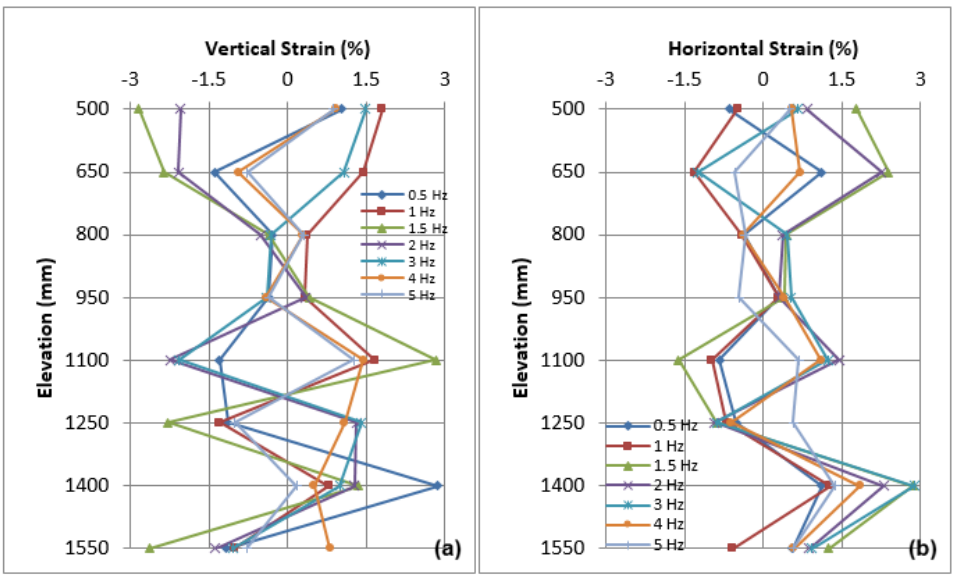

Figure 7.17. Maximum reinforcement strains in model 3 (a) vertical strains, (b) horizontal strains.

Figure 7.19(a) and Figure 7.19(b) depicts the maximum and average strains occurring on the reinforcement sleeve under sinusoidal excitation scheme. In Figure 7.19, only the tensile components of the horizontal strains are illustrated. In Figure 7.19(a), it is seen that the loading frequencies between 1 to 2 Hz cause highest tensile strains.

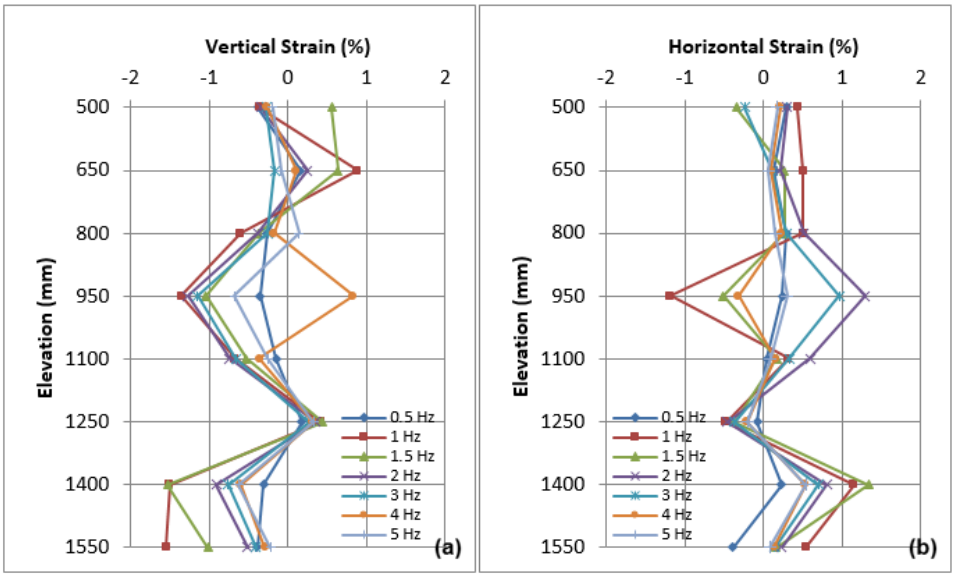

Figure 7.18. Maximum reinforcement strains in model 4 (a) vertical strains, (b) horizontal strains.

During the course of the Sinusoidal Excitation Scheme, to achieve compatible shear strains in the soft soil and to mobilize the shear strength of the GECs, the loading amplitude was consistently increased. Although the amplitude of loading was increased with increasing loading frequency, the tensile strain values were significantly lower for load cases with loading frequencies higher than 3 Hz. It could be deducted that the tensile strains are more sensitive to the frequency of the loading rather than the amplitude for both of the reinforcement materials used.

Figure 7.20 and Figure 7.21 gives the maximum vertical and horizontal strain values recorded for various input motions during Earthquake Excitation Scheme for model 7 and 8, respectively. Similar to the GECs excited with sinusoidal loads, the locations of maximum strains over the height of the column is more or less the same for each load case. The dominant frequency contents for the applied El-Centro and Kobe accelerograms are 2 and 1.5 Hz, respectively. These frequency values are within the frequency range where higher strain amplitudes are observed in the Sinusoidal Excitation Scheme experiments. Therefore combined effects of the frequency content of the loading and the increasing dynamic load amplitude caused an increase in the overall deformation of GECs.

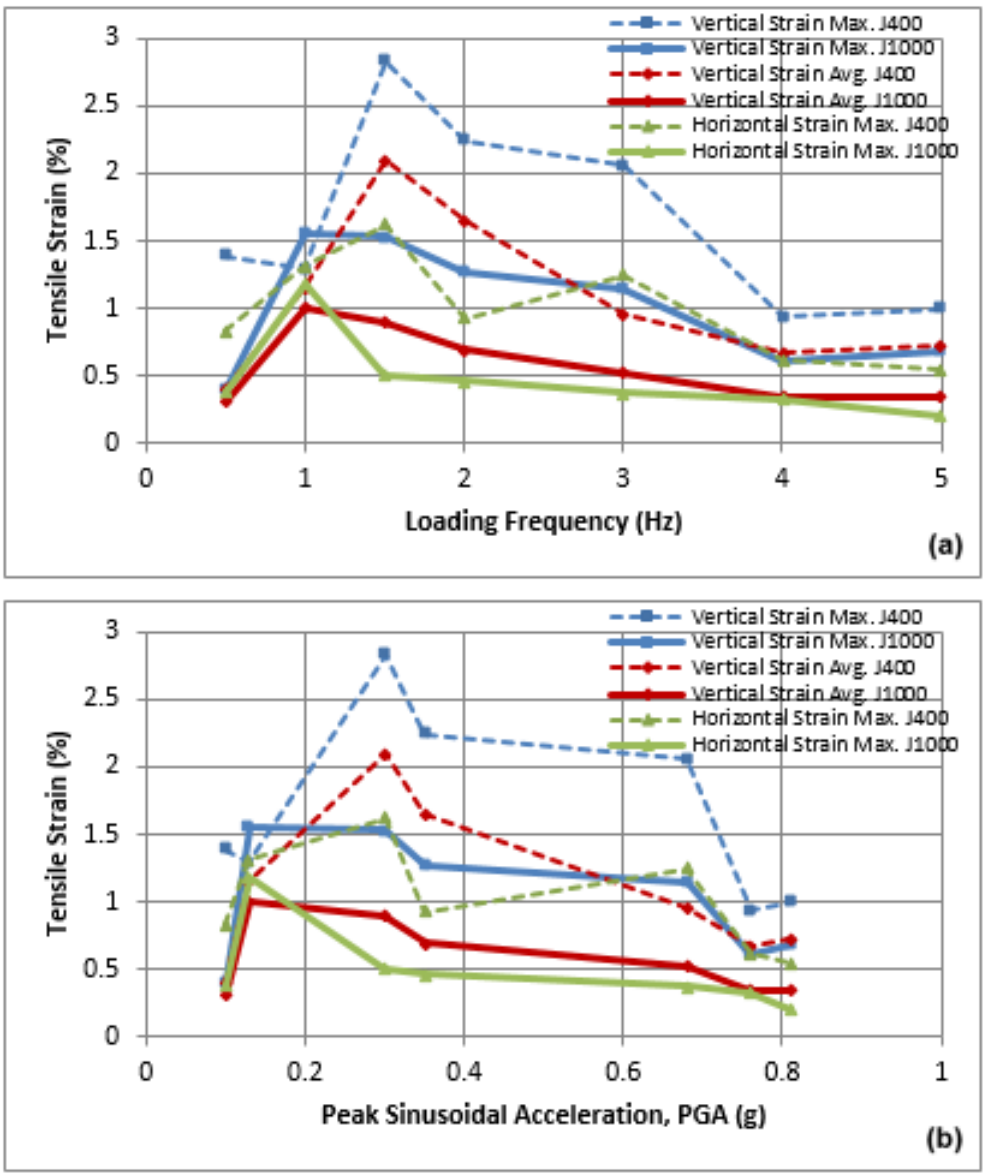

Figure 7.19. Maximum and average tensile strains on reinforcements as a function of (a) load frequency, (b) amplitude.

It is also seen that unlike the columns in models 3 and 4, increasing input accelerations caused higher strain values. While the highest vertical and horizontal tensile strain values for GT1 recorded during 100% Kobe loading were 2.3 and 0.6%, the same values for GT2 were 1.6 and 0.5%. Except for the bottommost instrumentation level, which is at a depth of 1550 mm from the top of the laminar box, the strains in the column reinforced with GT2 in model 8 remained below 1% for all load cases.

In Figure 7.20, the maximum vertical and horizontal strains occurring on GEC-J400-EQ during Earthquake Excitation Scheme is given. Under induced earthquake accelerations, the maximum reinforcement strain pattern occurring on the GEC is different than that of the vertical loading case where the column bulges in the top portion. The response of GEC-J400-EQ exhibits two critical maximum reinforcement strain locations over the height of the column and these locations lie approximately at 4 and 7 column diameters (4D and 7D) below the column head plane. At a depth of 4D, 100% Kobe loading causes a maximum vertical tensile strain is about 1.7% and the corresponding horizontal strain is about 1%. It is seen that for 100% El-Centro loading with a peak ground acceleration of 0.38 g, the reinforcement strains in general are less than 1%.

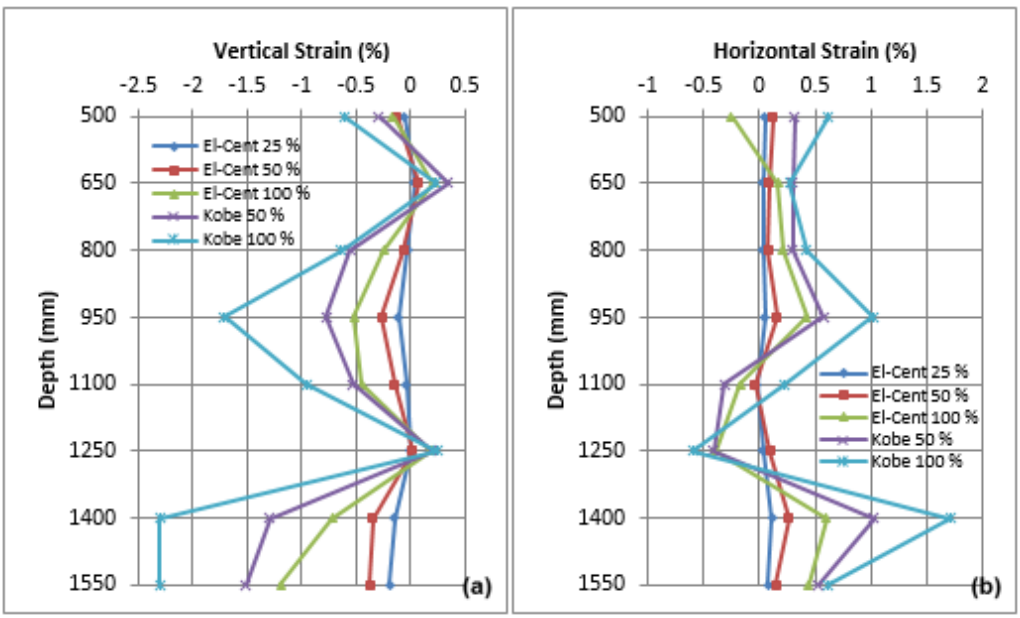

Figure 7.20. Maximum reinforcement strains in model 7 (a) vertical strains, (b) horizontal strains.

Partial reinforcement of GECs in order to mitigate the bulging failure that typically affects granular columns under the action of static vertical loads is suggested in the literature (Gniel and Bouazza, 2009; Yoo and Lee, 2012; Gu *et al.*, 2016). The partial reinforcement length is typically a few column diameters.

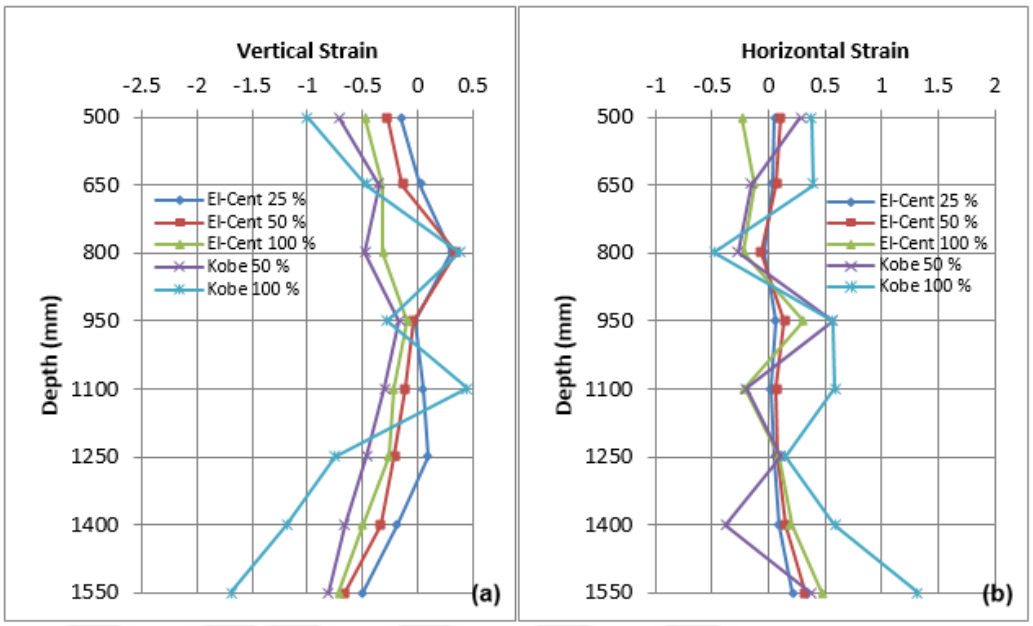

Figure 7.21. Maximum reinforcement strains in model 8 (a) vertical strains, (b) horizontal strains.

The plots in Figure 7.18, Figure 7.19, Figure 7.20, and Figure 7.21 suggest that there is a high strain demand brought about by the dynamic loading on all portions of the GECs including the bottom portions. Therefore partial reinforcement of granular columns should be avoided in seismically active areas.

Figure 7.22 illustrates only the tensile strains occurring both in vertical and horizontal (hoop) directions occurring during Earthquake Excitation Scheme. It is seen that increasing peak ground acceleration (PGA) values cause higher strain amplitudes in the reinforcements confining the granular material. These strain values are much higher than the ones that are given by Cengiz and Güler (2018) where the tests were run in a rigid box using the same geotextile materials as reinforcement with similar area replacement ratio for the columns. While the strain amplitudes given in Cengiz and Güler (2018) is representative of GECs surrounded by rigid earth retaining inclusions such as bridge abutments, retaining walls or sheet piles, the strain values illustrated in Figure 7.22 are representative of GECs' reinforcement response where the GECs are installed in a sufficiently large soft soil deposit unbounded by rigid inclusions. It is readily seen that the use of stiffer geotextile significantly reduces maximum and av-

erage tensile strains in the vertical direction. The maximum horizontal tensile strain response both of the columns encased with GT1 and GT2 remains more or less the same where the strain value increases for increasing input motion amplitude. Although the amplitudes of 100% El-Centro and 50% Kobe earthquakes are similar with both being in the neighborhood of 0.4 g, there is a significant jolt in the strain amplitudes between these two abscissa points in Figure 7.22. This may be caused by the difference in the frequency content of the two load cases. Such an increase in the strain response of the material is indicative of the frequency dependency of the geotextile strains under seismic loading.

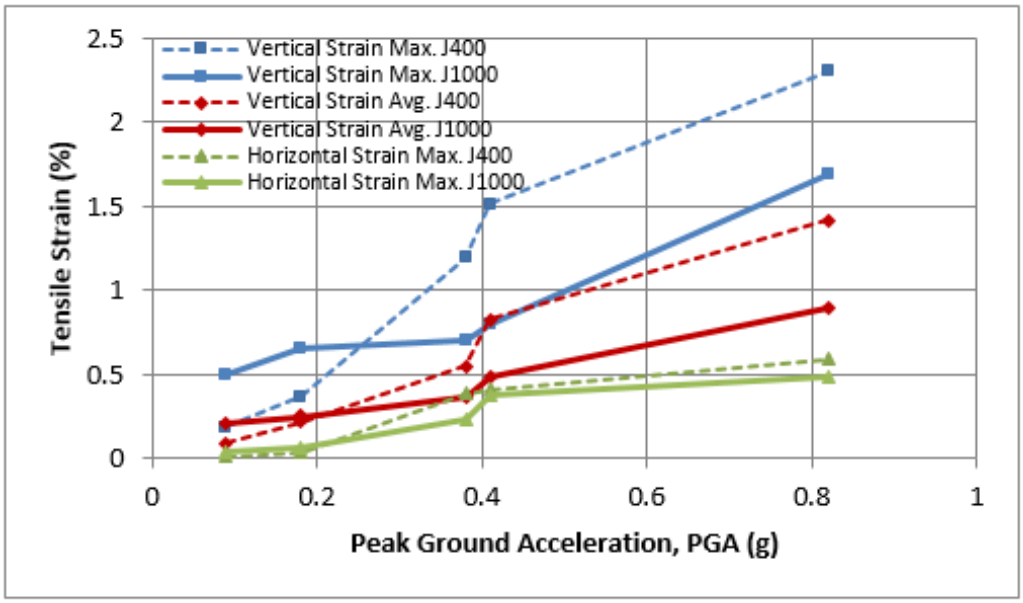

Figure 7.22. Maximum and average tensile strains as a function of PGA.

7.3. Soil Amplification

The soil amplification values 0.5 and 1 Hz loading case are given in Figure 7.23(a) and Figure 7.23(b), respectively. While the soil amplification curves' pattern is very similar for all granular column installed models in Figure 7.23(a), a significant difference in amplification values of Clay-S is seen. The onset of difference in the soil amplification response starts at a depth of 950 mm and the amplification value is almost consistently higher than that of other model soils.

Under 1 Hz sinusoidal load case however, the Clay-S responds to sinusoidal base input by a much lower amplification response. As discussed later, the untreated clay bed has consistently exhibited a lower amplification response to the load cases both in Sinusoidal and Earthquake Excitation Scheme. The likely reason for both untreated clay beds (Clay-S and Clay-EQ) to have a lower amplification response lies in the stiffness and resonant frequencies of the clay beds.

Since the benchmark models with untreated clay beds are devoid of column inclusions, their overall stiffness is relatively lower than those of granular column installed clay beds. Consequently, their resonant frequencies were lower hence Clay-S exhibited a rather high amplification response under the action of 0.5 Hz load case. Conversely, as depicted in Figure 7.26 and Figure 7.27(b), under the action of 100% El-Centro and Kobe load cases the amplification response of Clay-EQ was significantly lower amplification response than that of its counterparts. The dominant frequency content of El-Centro and Kobe accelerograms used in this study were 2 and 1.5 Hz, respectively.

In Figure 7.8(c) and Figure 7.9(b), Clay-EQ exhibited a higher maximum displacement response than most of the tested models. It could be said that Clay-EQ dissipated the dynamic input energy by displacing laterally. The stiffer models with GEC inclusions however exhibited significantly lower maximum displacement behavior in comparison to Clay-EQ. Models with GEC inclusions have also deformed like a coherent block by undergoing significant base drift. These two factors have caused larger soil amplification to occur in most of the models with OSCs and GECs.

In Figure 7.24, the amplification response of the models tested in Sinusoidal Excitation Scheme under the action of 1.5 and 2 Hz are given.

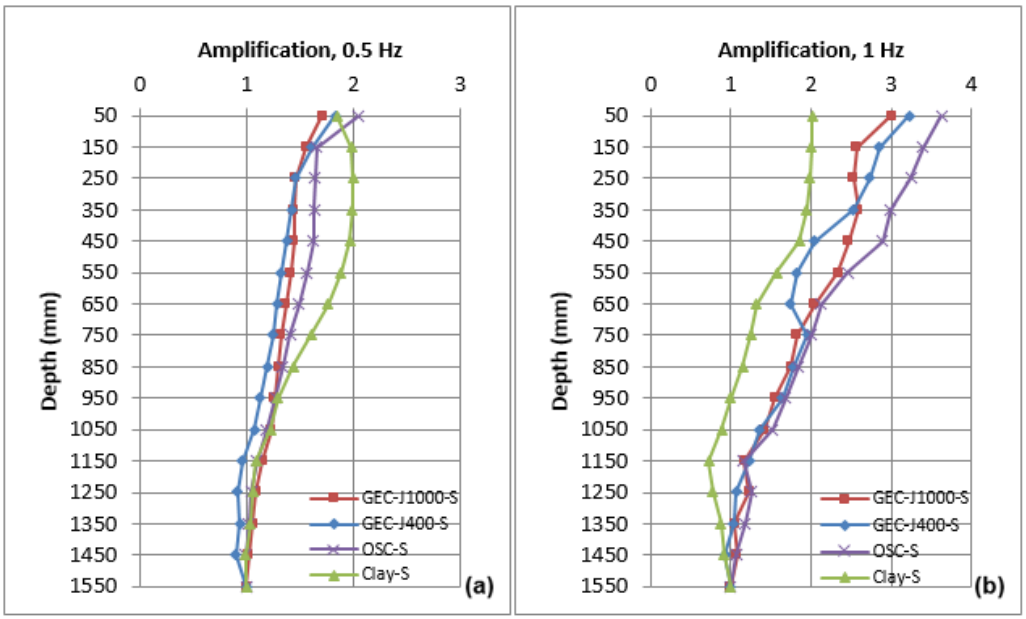

Figure 7.23. Plots of amplification values for Sinusoidal Excitation Scheme for 0.5 and 1 Hz.

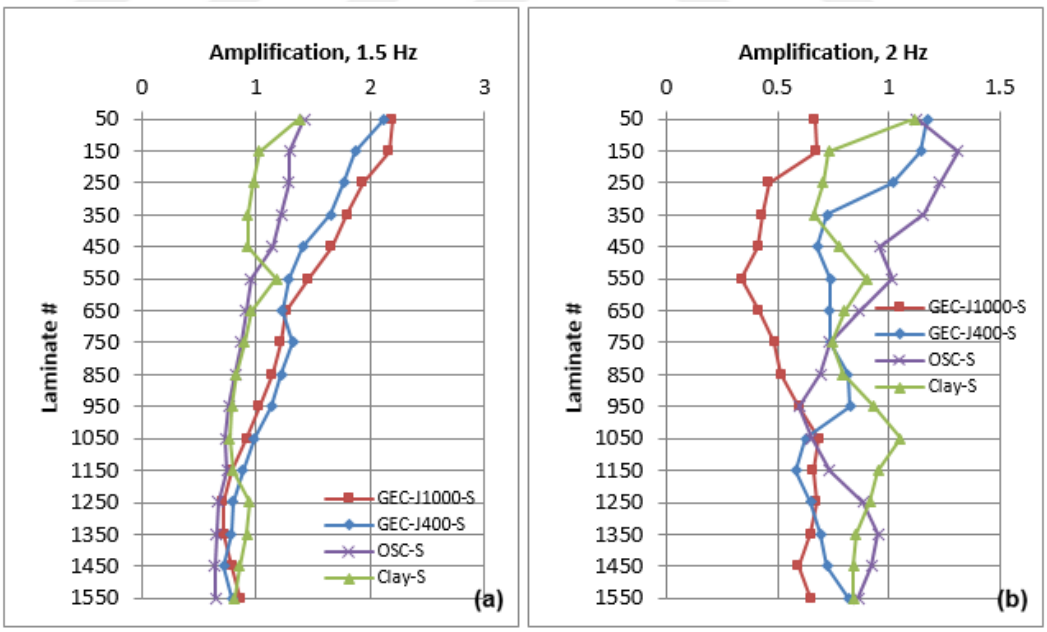

Figure 7.24. Plots of amplification values for Sinusoidal Excitation Scheme for 1.5 and 2 Hz.

In Figure 7.25, the amplification response of the models tested in Sinusoidal Excitation Scheme under the action of 3 and 4 Hz are given.

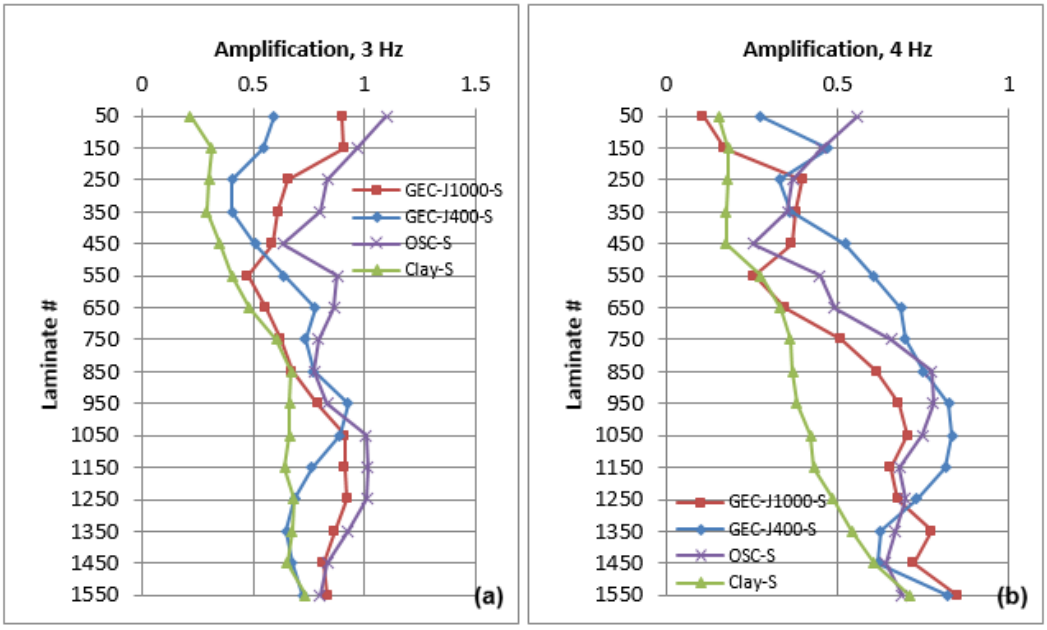

Figure 7.25. Plots of amplification values for Sinusoidal Excitation Scheme for 3 and 4 Hz.

In Figure 7.26, the amplification response of the models tested in Sinusoidal Excitation Scheme under the action of 3 and 4 Hz are given.

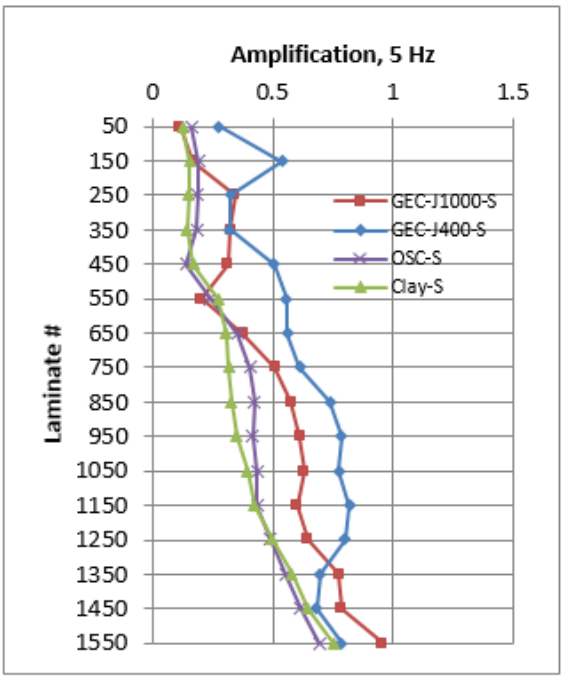

Figure 7.26. Plots of amplification values for Sinusoidal Excitation Scheme for 5 Hz load case.

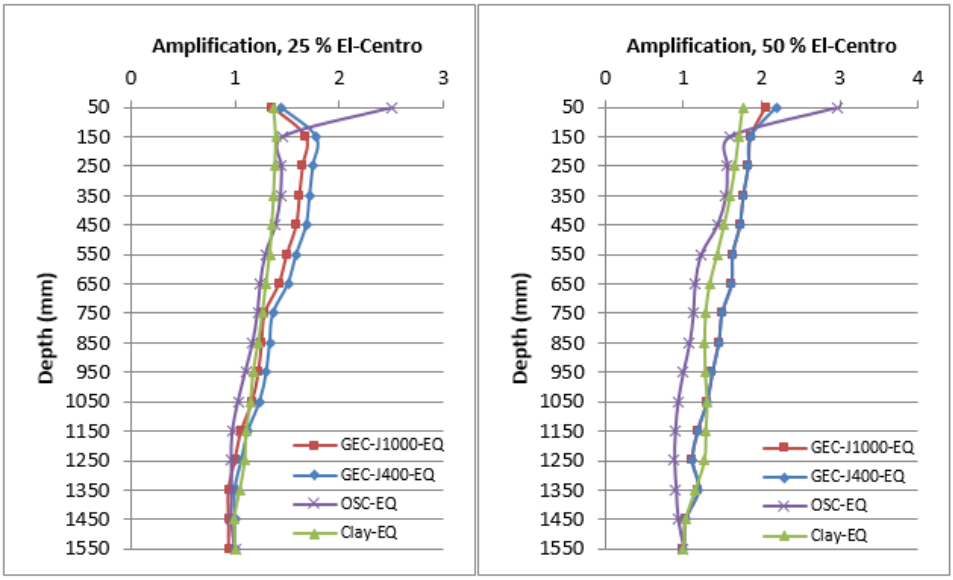

Figure 7.27. Plots of amplification values for Earthquake Excitation Scheme for 25 and 50% El-Centro load case.

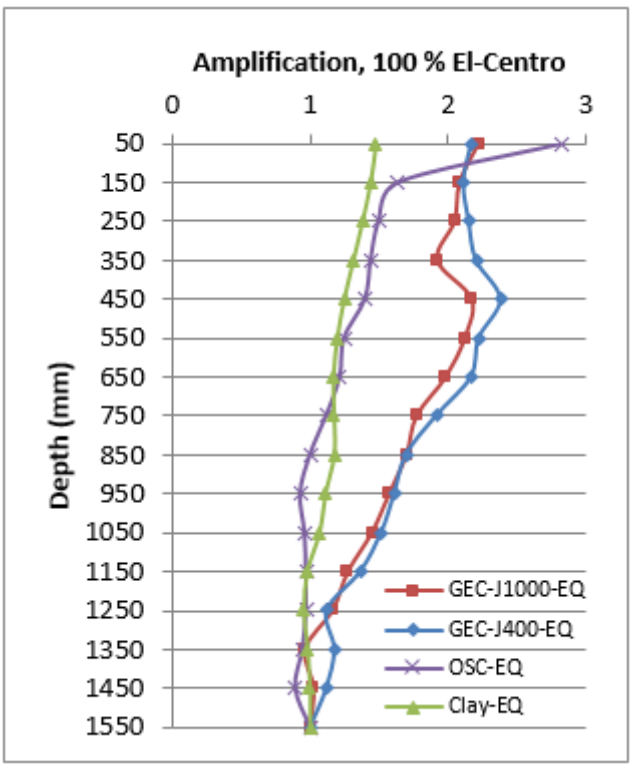

Figure 7.28. Plots of amplification values for Earthquake Excitation Scheme for 100% El-Centro load case.

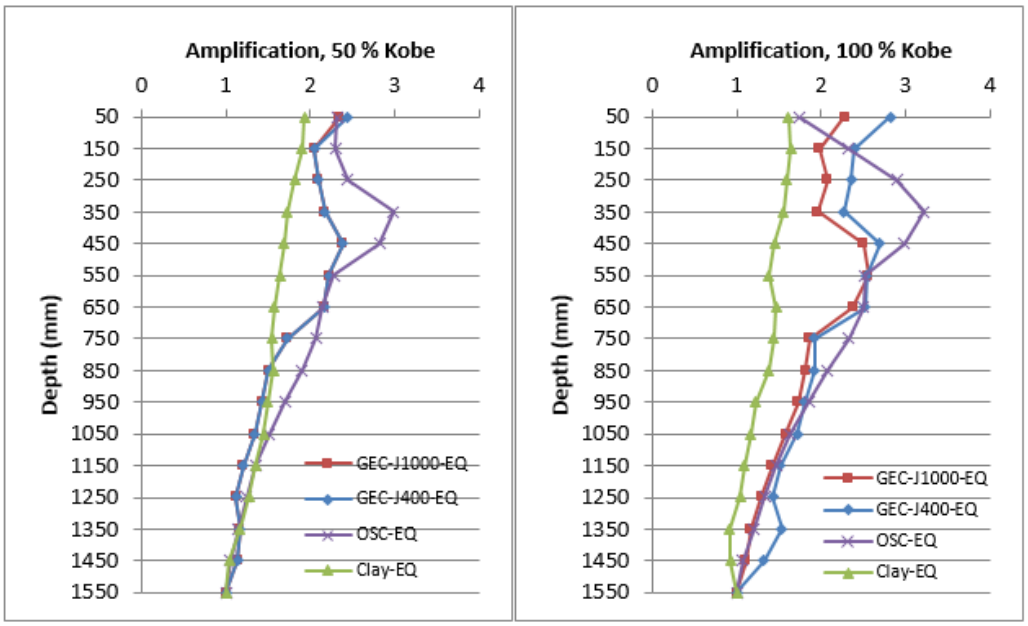

Figure 7.29. Plots of amplification values for Earthquake Excitation Scheme for 50 and 100% Kobe load case.

The abrupt change of the amplification values in the curves depicted for OSC-EQ in Figure 7.29(b) in towards the top portion of the laminar box was a rarity in the gathered experimental data. Moreover, the top level soil response is more relevant for the superstructure that is to be built on the embankment. For the rest of the data set, the top level soil amplification could be used to infer the general trend of the amplification response of the entire soil body. In Figure 7.30, soil amplification values for the top laminate level are given in frequency and PGA domain for Sinusoidal and Earthquake Excitation Scheme, respectively. The top laminate level amplification responses of the models with column inclusions tested in Sinusoidal Excitation Scheme were significantly higher for 1 and 1.5 Hz load cases.

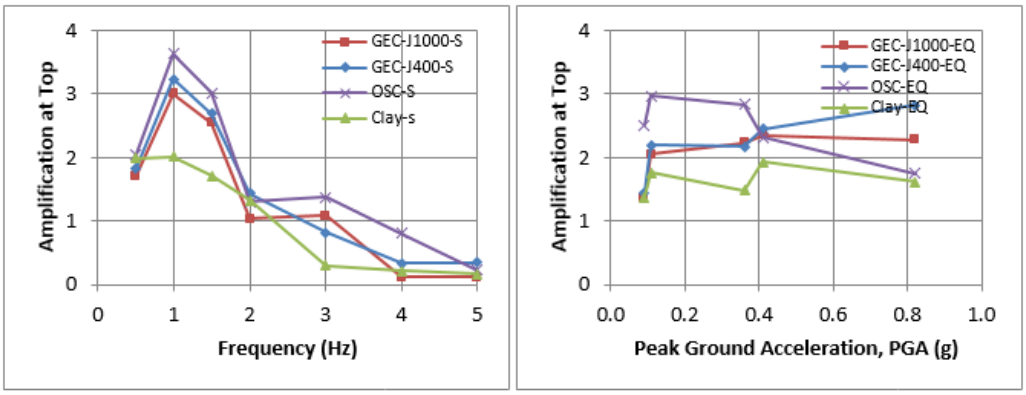

Figure 7.30. Soil amplification values for the top laminate level (a) Sinusoidal (b) Earthquake Excitation Scheme.

7.4. Shear Modulus and Damping Ratio of the Models

In the laminar box setup, the acceleration from the input excitation creates shear waves which propagate upwards in the model. The resulting acceleration responses in individual laminate levels are at various amplitudes and phases depending on the dynamic soil properties of a given level. Considering the inertia force in a layer to be resisted by shear stress, τ_d, at the top and bottom of a layer, total shear stress in nth layer can be expressed as

$$\tau_{d(n)} = \tau_{(n-1)} + \rho \ddot{u}_n H_n \tag{7.2}$$

where H_n is the thickness and ρ is the mass density of the soil mass in layer N, $\ddot{u}$ is the horizontal acceleration in layer N, and $\tau_{(n-1)}$ is the shear stress at the base of layer N-1. Since each laminate is instrumented with accelerometers, the wave propagation speed of shear waves generated by base excitations can be calculated by making use of the delay in wave arrival time between consecutive instrumentation levels. The vertical distance between each accelerometer is 100 mm in this study. Once the delays in the wave arrival time between instrumentation points are known, the shear wave velocity (V_s) between the instrumentation levels can be calculated. Within the scope of this study, pulse loading was employed to come up with the small strain shear modulus of the models. Pulse loading was selected as the first load case of the Sinusoidal Excitation

Scheme in an attempt to measure the shear wave velocity before the occurrence of large shear strains and shear modulus degradation that would result from the following load cases. Since the virgin soil beds were tested with pulse loading, a understanding of overall small strain shear modulus of the models was tried to be developed. A similar approach to predict the resonant frequency and the small strain shear modulus of the soil contained in a laminar box is reported by Dihoru *et al.* (2016).

Figure 7.31(a) and Figure 7.31(b) illustrate the responses of the accelerometers under pulse loading for OSC-s and GEC-J1000-S, respectively. Since the response of the soft clay beds enhanced with columns is of interest, the responses of accelerometers placed at the elevation of clay portion only were considered. In Figure 7.31(a) and Figure 7.31(b), it is seen that the input acceleration from the table reaches to a peak value and the onset of peak value for all laminate levels is delayed. While the amplitude of measured acceleration is higher than that of the input acceleration at laminate level 16 for the response of model 2 illustrated in Figure 7.31(a), in laminate levels 13, 14, and 15 the input signal is deamplified. In the remainder of the laminate levels, as the wave travels upwards, the amplitude of the measured acceleration is continuously higher indicating soil amplification. GEC-J1000-S, illustrated in Figure 7.31(b), deamplified the input acceleration in laminate level 15 but in this case the deamplified acceleration amplitude is not lower than that of the input acceleration. While the recorded accelerations are persistently higher than the input amplitude, the maximum soil amplification in GEC-J1000-S was less than that of the OSC-S. The calculated shear wave velocities for models 1 to 4 are 8.4, 12.6, 19.1, and 24.5 m/s, respectively.

The small strain (G_{max}) shear modulus of the soft soil composite inside the laminar box could be calculated by making use of the following equation.

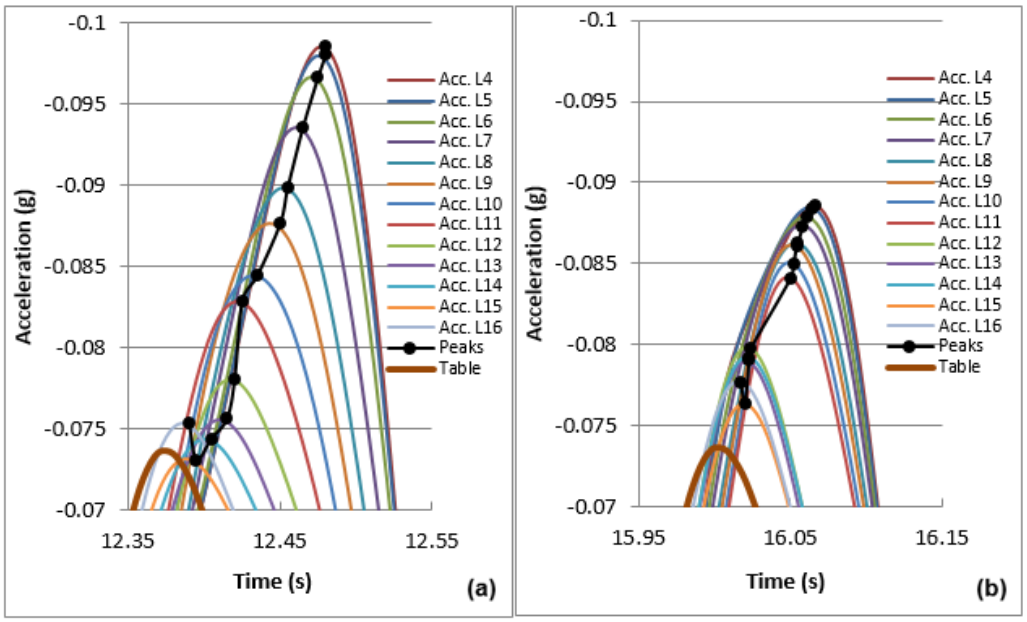

Figure 7.31. Acceleration response to pulse loading for (a) OSC-S and (b) GEC-J1000-S.

$$G_{max} = \rho V_s^2 \tag{7.3}$$

where ρ is the mass density of soil. Using an average bulk mass density of 1630 kg/m^3 for all models tested, the small strain shear modulus for models 1 to 4 were calculated to be 115, 259, 595, and 978 kPa, respectively and given in Table 7.1. These results indicate that inclusion of high modulus GECs at an area replacement ratio of 7% increased the small-stiffness shear modulus of soft clay bed by almost and order of magnitude.

While the shear modulus of the models under small strain conditions is calculated by making use of the shear wave velocity, the shear modulus for dynamic sinusoidal loads is calculated from the hysteresis loops. The difficulties associated with obtaining hysteresis loops that resemble the curves originating from small scale laboratory tests is explained in Brennan *et al.* (2005). In large scale experimental work under dynamic loading conditions, clear-cut hysteresis loops do not typically occur. In large scale

testing with a laminar box type apparatus, calculation of shear strain at a particular laminate level involves computing the difference in displacement values of neighboring laminates in time domain (as per Equation 7.1).

As the soil is sheared, the material properties of the soil, loads and displacements imposed on a given level of the laminar box changes. Moreover these changes are of highly nonlinear nature and the rate of change for different levels in the laminar box such as the degradation rate of shear modulus may not be identical. A shift in the phases of laminates during course of dynamic loading could also be encountered. There can be other soil-laminar box response conditions such as decoupling of the soil from the confining laminar box or occurrence of negative hysteresis loops with more than one closed area, as reported by Araei and Towhata (2014).

The shear stress-strain calculations were conducted in accordance with ASTM 3999 and the maximum stress and strain point method was adopted for the 10th cycle in the leveled part of the shear strain curves created in time domain. Figure 100 depicts the 10th cycle of the OSC-S and GEC-J1000-S at laminate level 8 under the action of 0.5 Hz loading. In Figure 4.3(a) and Figure 4.3(b), 0.5 Hz load case is illustrated both for the raw strain values and for fitted values.

Since the movement of the laminate as observed from the position of the laser displacement sensor is essentially smooth, use of the displacement data for plotting strain-stress response will create smooth and legible hysteresis curves. The measurement of displacement alone will not provide enough data as to the relative movement of the laminate to the neighboring level and therefore calculation of strain is not possible. This problem is handled by fitting the displacement data on top of the calculated strain response such that the extents of the maximum strain values are covered. Thusly the fitted hysteresis loops are plotted in Figure 4.3.

Table 7.1. Shear modulus in kPa.

Model	Pulse*	0.5 Hz	1 Hz	1.5 Hz	2 Hz	3 Hz	4 Hz	5 Hz
1	115	14.5	5.7	6.1	6.6	12.7	25.2	31.1
2	259	21.1	9.7	12.7	19.5	25.7	35.0	51.0
3	595	39.6	23.1	26.6	27.3	50.6	63.9	151.3
4	978	90.6	68.9	64.3	63.5	96.6	194.8	211.1
*Small strain shear modulus calculated from pulse loading								

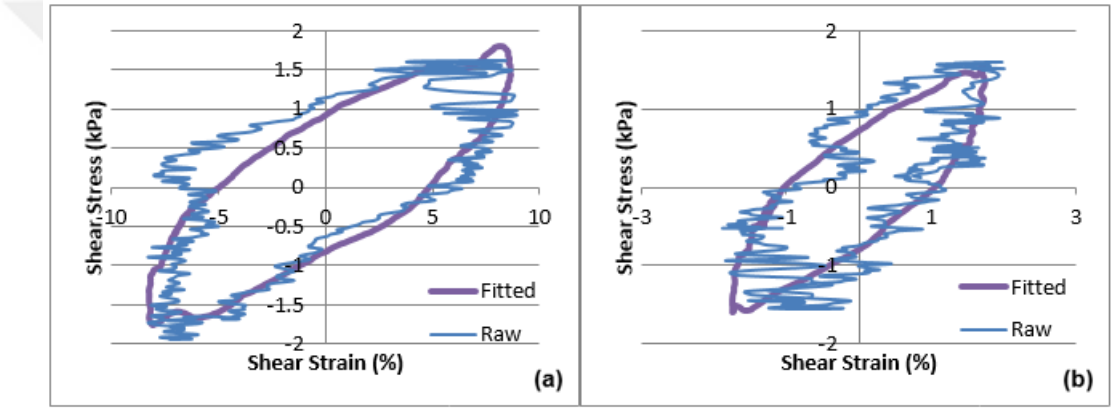

Figure 7.32. Fitted and rough hysteresis loops for the 8^{th} laminate level for (a) OSC-S and (b) GEC-J1000-s during 0.5 Hz load case.

By making use of the above mentioned hysteresis loop fitting process the hysteresis loops pertaining to all four models for 0.5 Hz load case is illustrated in Figure 7.33. In Figure 7.33, it is seen that the increasing GEC reinforcement stiffness yielded higher secant shear modulus values. It is also seen that the OSC installed model namely, OSC-S, had a higher secant modulus value than the untreated clay bed.

While it is possible to create hysteresis loops for low frequency loading cases by employing the fitting procedure mentioned above, for higher frequency load cases the hysteresis loops are more complicated.

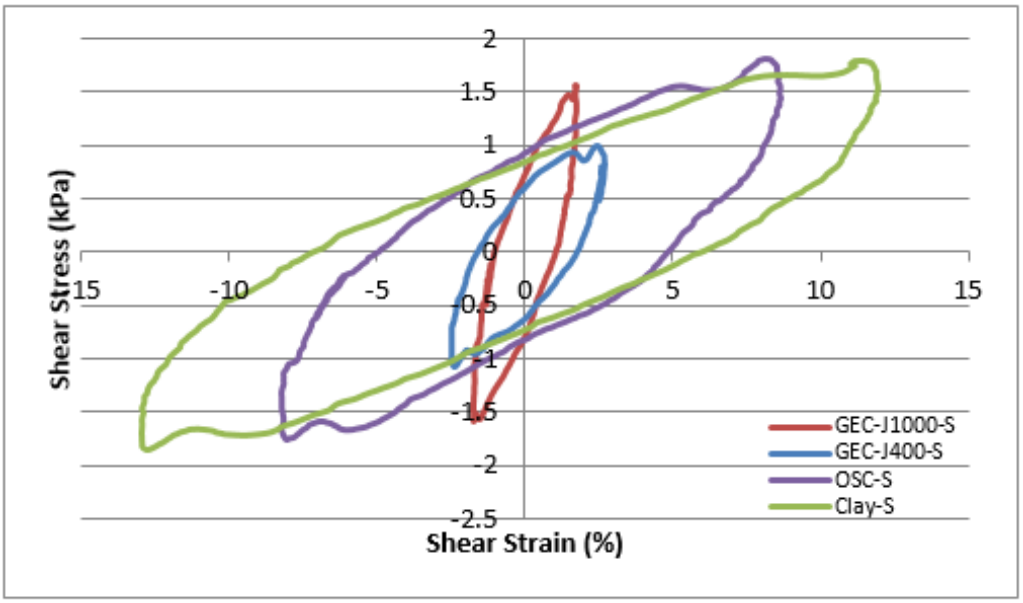

Figure 7.33. 10^{th} cycle hysteresis loops for models 1, 2, 3, and 4.

The hysteresis loops depicted in Figure 7.34 illustrate the nature of hysteresis loops pertaining to GEC-J1000-S under the action of 3 and 4 Hz load cases. Similarly Figure 7.35 illustrate the nature of hysteresis loops pertaining to OSC-S under the action of 4 and 5 Hz load cases. The responses depicted in these figures are for laminate level 8.

When the analysis of laminar box experiments yields such hysteresis loops the shear modulus of the soil could be calculated by relying on the slope of the shear stress-strain curve. The calculation of damping however necessitates a slightly different approach than the damping calculations that are typically done for a conventional hysteresis response loop that has only one closed area. When there are more than one closed areas in the hysteresis loops, the transition zones where the lower bound curve is above the upper bound curve, the calculated work decreases as these zones create a net negative work area. There could be cases where the calculated damping coefficient could have a net negative value. In such cases an equivalent damping ratio could be calculated as reported by Brennan *et al.* (2005). Within the scope of this work, the damping values are only calculated for 0.5 and 1 Hz load cases.

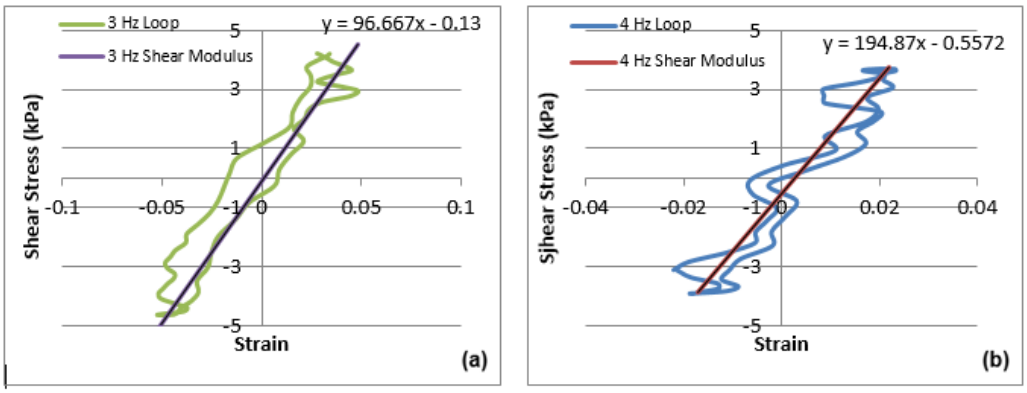

Figure 7.34. Hysteresis loops for laminate level 8 for test section 4 (a) at 3 Hz load case, (b) 4 Hz load case.

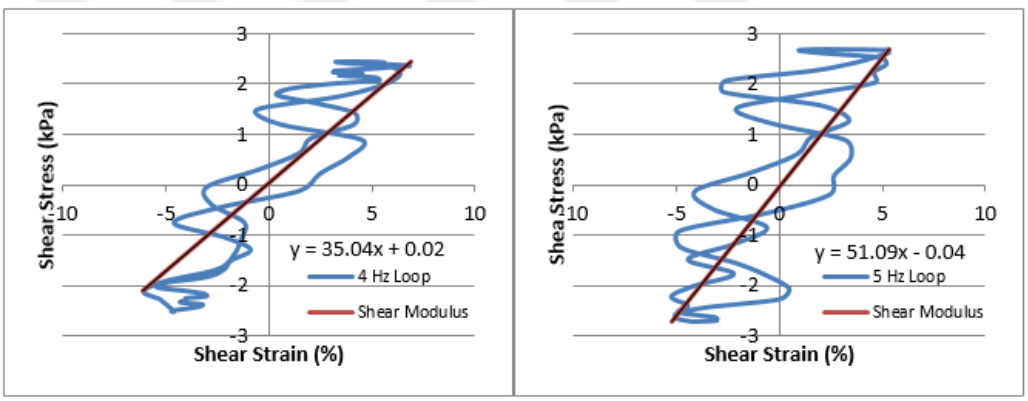

Figure 7.35. Hysteresis loops for OSC-S for (a) 4 and (b) 5 Hz.

Table 7.1 gives the calculated small strain and secant shear modulus of the models. For all models tested, the decrease of shear modulus from small strain measurements to secant modulus calculations is 10 folds which is consistent with available literature. In Table 18, it is seen that the calculated secant shear modulus for soils increase with increasing loading frequency. This could be due to increased shear rate and viscous effects. The damping ratios calculated for 0.5 and 1 Hz loading are given in Table 7.2. The damping ratio for all models are in the order of 25% for 0.5 Hz loading. For 1 Hz load case, the damping ratio of model 4 is 32% and this value is slightly higher than that of the rest of the tested models.

Table 7.2. Damping ratio calculated from hysteresis loops in%.

		Damping Ratio (%)	
Model	Designation	0.5 Hz	1 Hz
1	Clay-S	23.5	25.8
2	OSC-S	25.7	24.6
3	GEC-J400-S	26.7	27.4
4	GEC-J1000-S	24.4	32

7.5. Vertical Load Capacities of Columns

The load-settlement behaviors of GECs and OSCs subjected to Earthquake Excitation Scheme and their intact counterparts were determined by a series of stress-controlled vertical load tests. The load-settlement behaviors of the intact and seismically tested columns are presented in Figure 7.36.

Comparison of the vertical load-settlement behaviors of intact and seismically loaded GECs reveal that the vertical load capacities of the GECs are not significantly impaired by the seismic loading. The load settlement behaviors of the OSC samples however, are significantly different with the seismically loaded OSC settling significantly more than its intact counterpart. At an applied vertical pressure of about 165 kPa, seismically loaded (tested) OSC settles 55% more than the intact OSC. In seismically active zones, significant loss of vertical load capacity of the OSC should be expected and accounted for in the design of foundation systems. The findings indicate that use of geotextile reinforcement aids in mitigating the vertical load capacity loss upon seismic loading.

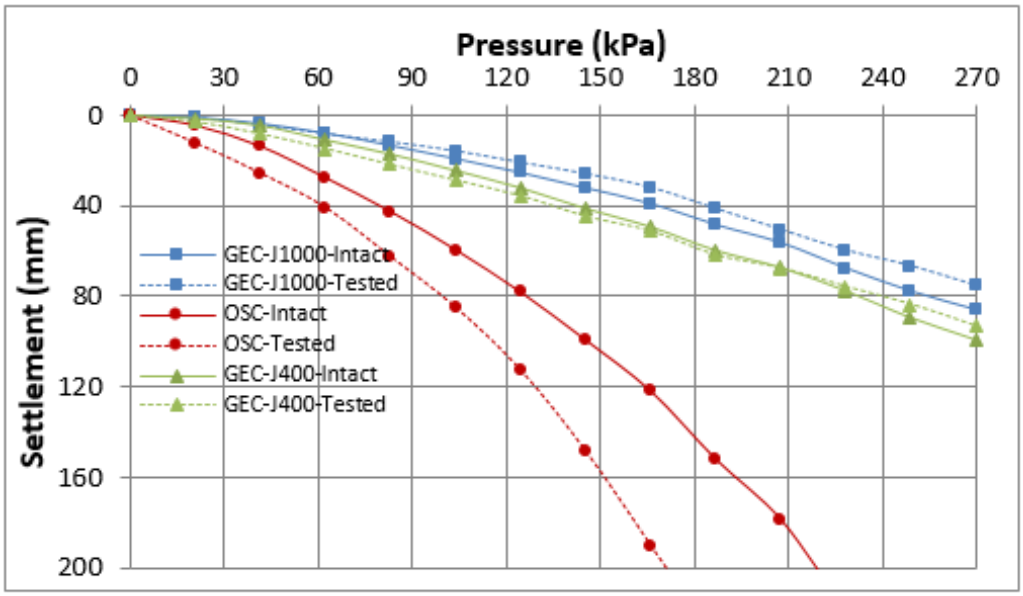

Figure 7.36. Load-settlement curves for intact and seismically tested columns.

7.6. Conclusions

1-G shaking table tests are performed with a laminar box type apparatus to study the behavior of OSC and GEC enhanced soft soil beds' response under the action of sinusoidal loads of varying frequency. The following conclusions are drawn from the analysis of the experimental data:

- The response of the GECs is dependent on both the loading frequency and the amplitude of the dynamic base excitation. The highest reinforcement strains were observed for a frequency range of 1 to 2 Hz. In the testing program, the amplitude of the sinusoidal input was increased for increasing loading frequency to induce sufficient levels of shear strain in the soil to mobilize the shear resistance of GECs and OSCs. Even under increased sinusoidal loading amplitude, the reinforcement strains were significantly lower for loading frequencies greater than 3 Hz. At a sinusoidal loading frequency of 1.5 Hz with a peak sinusoidal acceleration of 0.3 g, the maximum reinforcement strain in GEC GTX1 (J = 400 kN/m) and GEC GTX2 (J = 1000 kN/m) was 2.8 and 1.5%, respectively. Under the action of 4 Hz (0.76 g) sinusoidal load case these values became 0.9 and 0.6%.

- Under simulated earthquake accelerograms, higher reinforcement stiffness (J) led to lower reinforcement strains. The highest vertical and horizontal tensile strain values for GTX1 recorded during 100% Kobe loading were 2.3 and 0.6%, the same values for GTX2 were 1.6 and 0.5%. The frequency contents of both El-Centro and Kobe accelerograms were with the 1 to 2 Hz frequency window where GECs are more sensitive to dynamic loading effects which led to increased reinforcement strain values for increasing PGA values.
- The strain demands brought about by the dynamic loads are distributed to the entire height of the column. Reinforcement strains as high as 3% is observed at a depth of about 8D from column head plane. Partial reinforcement of the GECs should be avoided in seismically active areas. In partially reinforced columns, in the absence of a reinforcement material to confine the column constituents at lower portions of the column, bulging failure due to seismic loads below the reinforced zone could occur.
- While there is no marked effect of dynamic loading on the vertical load carrying capacity of the GECs, there is significant decrease in the vertical load capacity of dynamically loaded OSC as opposed to their intact counterparts. The vertical load carrying capacity losses as high as 55% is observed in the columns tested. Significant reduction of OSC vertical load capacity should be anticipated in seismically active zones.
- Inclusion of geosynthetic encased columns vastly reduced the lateral displacements under the action of sinusoidal loads. The reduction in displacement was more pronounced for lower frequency load cases. Inclusion of four GECs with a reinforcement stiffness of 1000 kN/m reduced the top layer displacements by 57% when compared to benchmark tests conducted with untreated clay bed.
- There is a fundamental difference in the deformation mode of the GEC enhanced and OSC treated clay bed. While there is significant base lamina drift for GEC enhanced clay beds, OSC treated and benchmark (untreated) clay bed undergo minimal movement at base layer. This may be due to GECs' ability to hold the clay bed together as a coherent body. The ability of GEC to hold the soft clay bed together aids in reducing the top laminate level displacements to a minimum

as well. The OSC treated and soft clay test sections have exhibited higher top laminate level displacements.

- Across all induced frequency ranges, inclusion of stiffer columns lead to higher soil amplification. Untreated clay bed exhibited a smaller soil amplification response in general.
- The propagation of sinusoidal loads causes tensile strains in the vertical direction of the reinforcement. Therefore under dynamic base excitation also the vertical tensile strength of the geosynthetic encapsulation should be considered. The vertically oriented tensile strain on the encasement can be as high as 3%.
- Such tensile elongation is countered with hoop (horizontal) contraction of the reinforcement which yields compressive strains. However during the dynamic motion also additional horizontal tensile (hoop) strains are developed. So an increased demand of horizontal tensile strength must be considered in design. It was observed that the maximum amplitude of horizontally oriented tensile strain was around 1.5%.
- It is also seen that there is a high strain demand at lower elevations of the GEC. This may mean that partial reinforcement of GECs in seismically active zones should be cautiously practiced and if possible avoided.
- It is seen that the presence of GEC inclusions decrease the shear strains occurring in soft clay beds. Increasing column stiffness and reinforcement stiffness aids in decreasing the shear strains that the soft soil undergoes.
- The small strain shear modulus of soil with the stiffer GEC was almost 10 folds larger than that of untreated clay bed. The small strain shear modulus of untreated soft clay was 115 kPa. With ordinary stone columns it increased to 259 kPa and with GECs to 595 and 978 kPa respectively for different stiffnesses of encapsulation.
- Secant shears modulus of the test sections were almost 10 folds lower than that of the small strain shear modulus. Secant shear modulus for all test sections increased with increasing loading frequency. It is again observed that with the inclusion of high stiffness encapsulation, the secant modulus values increases significantly compared to the soft clay.

- While the damping ratio of test sections were more or less of similar value for 0.5 Hz loading, for the case of 1 Hz loading, the inclusion of GEC with a stiffness of 1000 kN/m increased the damping value significantly. For 1 Hz load case the damping values of soft clay bed, OSC installed clay bed, GEC enhanced clay beds of reinforcement stiffnesses of 400 and 1000 kN/m were 25.75, 24.55, 27.38, and 32.01%, respectively.

8. CONCLUSIONS AND RECOMMENDATIONS FOR FUTURE STUDIES

In this study, the response of individual ordinary stone columns and geosynthetic encased stone columns and the response of column enhanced soft soil were investigated through a series of shaking table experiments. Two large scale experimental setups were designed and built for the purposes of shaking table experiments. The first setup is a rigid box is utilized to study the response of the individual columns and the soil body that are laterally constrained. Typical elements that laterally confine or constraint the columns are retaining structures, sheet piles, bridge abutments, and at times channel sections.

The results pertaining to rigid box tests are elaborated at the end of Chapter 6 of this dissertation. The key points of interest for the rigid box results are: (i) stiffer geotextile reinforcements have a markedly high settlement reduction capability under the action of simulated earthquake accelerograms, (ii) The strain demand on the geotextile reinforcement is spread throughout the height of the column, therefore partial reinforcement of the columns should be avoided in seismically active sites, (iii) there is a correlation between the seismic input energy expressed in terms of Arias Intensity (IA). This relationship may be utilized to assess the seismically induced damage on existing geosynthetically reinforced soil masses and/or may be used as a means to determine the additional seismic strain demand on the reinforcement for the design of geosynthetic reinforced structures.

For future study purposes, the correlation between the IA and the reinforcement strain should be explained by a constitutive material model where the response of the soil mass and the geosynthetic is coupled. The wave propagation thorough the reinforced soil composite may explain the amplitude of strain accumulation in certain parts of the model and/or the prototype. Essential conclusions drawn from the laminar box tests are: (i) the small-strain shear modulus of GEC enhanced soil is significantly

higher than that of untreated soft clay bed. Similarly under the action of sinusoidal base excitations, the shear stress-strain (hysteresis) response of the GEC enhanced clay is markedly superior to that of the benchmark clay bed, (ii) while the vertical load carrying capacity of the GECs are not significantly impaired by the application of dynamic excitations, the vertical load carrying capacities of ordinary stone columns dropped as much as 55% once they were subjected to dynamic loads, (iii) in the currently available literature, the reinforcement in GECs is only considered to be a countermeasure against bulging failure. Consequently, the vertical strength of the material and occurrence of vertical strains are not investigated in the literature. This study has experimentally shown that there is a high vertically oriented reinforcement strain demand which is at times higher in amplitude than that of the horizontal (hoop) strain demand. A probable mode of failure GECs that are subjected to dynamic loads therefore is thusly defines as the rupture of the vertically aligned fibers of the GECs. Under the action of the vertical embankment loads, with the effects of load eccentricity and moments this mode of failure may be the dominant mode of failure for prototype columns.

An issue for future study is to study the response of the columns when they are vertically loaded with embankment loads of sufficient magnitude. Combined effects of eccentricity and moments acting on the column should be thoroughly studied. The effectiveness of GEC inclusion should be tested against some other design parameters such as the layout pattern of columns (triangular, square grid, etc.) and the effects of using various reinforcement materials should obviously be studied.

REFERENCES

Adalier, K., A.W. Elgamal, "Seismic Response of Adjacent Saturated Dense and Loose Sand Columns", *Soil Dynamics Earthquake Engineering*, Vol. 22, No. 2, pp. 115-127, 2002.

Alexiew, D., D. Brokemper, S. Lothspeich, "Geotextile Encased Columns Load Capacity", *United States*, Vol. 1, pp. 497-510, 2005.

Ambily, A.P., S.R. Gandhi, "Behavior of Stone Columns Based on Experimental and FEM Analysis, Journal Geotech Geoenviron Engineering", American Socienty of Civil Engineering, Vol. 133, No. 4, pp. 405-415, 2007.

Andreou, P., W. Frikha, R. Frank, J. Canou, V. Papadopoulos, J.C. Dupla, "Experimental Study on sand and Gravel Coluns in clay", *Ground Improv*, Vol. 161, No. 4, pp. 189-198, 2008.

Araei, A.A., I. Towhata, "Impact and Cyclic Shaking on Loose Sand Properties in Laminar Box Using Gap Sensors", *Soil Dynamics and Earthquake Engineering*, Vol. 66, pp. 401-414, 2014.

Arias, A., A Measure of Earthquake Intensity, "Seismic Design for Nuclear Power Plants", *Massachusetts Instate of Engineering Press*, Vol. 1, pp. 438-483, 1970 .

Ayadat T, A.M. Hanna, "Encapsulated Stone Columns as a Soil Improvement Technique for Collapsible Soil", *Ground Improv*, Vol. 9, No. 4, pp. 137-147, 2005.

Bachus, R.C., R.D. Barksdale, "Vertical and Lateral Behavior of Model Stone Columns", *Proceedings of the International Conference on in Situ Soil and Rock Reinforcement*, Vol. 1, pp. 99-104, 1984.

Barksdale, R.D., R.C. Bachus, "Design and Construction of Stone Columns", *Federal*

Highway Administration, Vol. 1, pp. 194, 1983.

Bauman, V., G.E. Bauer, "The Performance of Foundations on Various Soils Stabilized by the Vibrio-Compaction Method", *Can Geotech Journal*, Vol. 11, No. 4, pp. 509-530, 1974.

Bergado, D.T., F.L. Lam, "Full Scale Load Test of Granular Piles with Different Densities and Different Proportions of Gravel and sand in the Soft Bangkok Clay", *Soils Found Journal*, Vol. 27, No. 1, pp. 86-93, 1987.

Bethapudi, R., *Liquefaction-Induced Lateral Spreading in 1g Full-Scale Shake Testing*, M.S. Thesis, New York at Buffalo, 2008.

Bhattacharya, S., D. Lombardi, L. Dihoru, M.S. Dietz, A.J. Crewe and C.A. Taylor, "Model Container Design for Soil-Structure Interaction Studies Role of Seismic Testing Facilities in Performance", *Based Earthquake Engineering*, Vol 5, pp. 135-158, 2012.

Black, J., V. Sivakumar, M.R. Madhav, B. McCabe, "An Improved Experimental Set-Up to Study the Performance of Granular Columns", *Geotech Test Journal*, Vol. 29, No. 3, pp. 193-199, 2006.

Black, J., V. Sivakumar, J.D. McKinley, "Performance of Clay Samples Reinforced with Vertical Granular Columns", *Can Geotech Journal*, Vol. 44, pp. 89-95, 2007.

Black, J.V., V. Sivakumar, A. Bell, "The Settlement Performance of Stone Column Foundations", *Geotechnique*, Vol. 61, No. 11, pp. 909-922, 2011.

Brauns, J., "Initial Bearing Capacity of Stone Columns and Sand Piles. Soil Reinforcing and Stabilizing Techniques in Engineering Practice", *Sydney I*, Vol. 1, pp. 497-512, 1978.

Briaud, J.L., "The Pressuremeter Some Special Applications. Proceedings of the

Geotechnical Engineering Congress", *American Society Of Civil Engineering Geotechnical Special Publication*, Vol. 1, No. 27, pp. 26-37, 1991.

Carvalho A.T., J. Bile Serra, F. Oliveira, P. Morais, A.R. Ribeiro, C. Santos Pereira, "Design of Experimental Setup for 1 g Seismic Load Tests on Anchored Retaining Walls Physical Modelling in Geotechnics", *Taylor and Francis Group*, London, 2010,

Castro, J., C. Sagaseta, "Deformation and Consolidation Around Encased Stone Columns", Geotext Geomembr Vol. 29, pp. 268-276, 2011.

Charles, J.A., K.A., "Watts Compressibility of Soft Clay Reinforced with Granular Columns", *In Proceedings of the 8th European Conference on Soil Mechanics and Foundation Engineering*, Helsinki, 1983.

Chen, J.F., J. Han, S. Oztoprak, X.M. Yang, "Behavior of Single Rammed Aggregate Piers Considering Installation Effects", *Comput Geotech*, Vol. 36, pp. 1191-1199, 2009.

Chen, J.F., L.Y. Li, J.F. Xue, S.Z. Feng, S.-Z., "Failure Mechanism of Geosynthetic-Encased Stone Columns in Soft Soils under Embankment", *Geotextiles and Geomembranes*, Vol. 43, pp. 424-431, 2015.

Cimentada, A., A. Da Costa, J. Canizal, C. Sagaseta, "Laboratory Study on Radial Consolidation and Deformation in Clay Reinforced with Stone Columns", *Can Geotech Journal*, Vol. 48, pp. 36-52, 2011.

Crewe, A,J, M.L. Lings, C.A. Taylor, A.K. Yeung, R. Andrighetto, *Development of A Large Flexible Shear Stack for Testing Dry Sand and Simple Direct Foundations on A Shaking Table, European Seismic Design Practice*, Balkema, Rotterdam, 1995.

Dar, A.R., *Development of Flexible Shear-Stack for Shaking Table of Geotechnical Problems*, Ph.D. Thesis, University of Bristol, 1993.

Dash, S.R. *Lateral Pile-Liquefied Soil Interaction during Earthquakes.* Ph.D. Thesis, University of Oxford, Oxford, 2010.

Dihoru, L., S. Bhattacharya, F. Moccia, A.L. Simonelli, C.A. Taylor, G. Mylonakis, "Dynamic Testing of Free Field Response in Stratified Granular Deposits", *Soil Dynamics and Earthquake Engineering*, Vol. 84, pp. 157-168 2016.

Elshazly, H.A., D.H. Elhafez, M.E. Mossaad, "Reliability of Conventional Settlement Evaluation for Circular Foundations on Stone Columns", *Geotech Geol Engineering Journal*, Vol. 26, pp. 323-334, 2008a.

Elshazly, H.A., M. Elkasabjy, A. Elleboudy, "Effect of Inter Column Spacing on Soil Stresses Due to Vibro-Installed Stone Columns Interesting Findings", *Geotech Geol Engineering Journal*, Vol. 26, pp. 225-236, 2008b.

Fattah, M.Y., K.T. Shlash, M.J.M. Al-Waily, "Stress Concentration Ratio of Model Stone Columns in Soft Clays", *Geotech Test Journal*, Vol. 34, No. 1, pp. 1-11, 2011.

Fishman, K.L., J.B. Mander, R. Richards, "Laboratory Study of Seismic Free-Fi Eld Response of Sand", *Soil Dynamic Earthquake Engineering*, Vol. 14, pp. 33-43, 1995.

Frikha, W., M. Bouassida, J. Canou, "Observed Behaviour of Laterally Expanded Stone Column in Soft Soil", *Geotechnical and Geological Engineering*, Vol. 31, pp. 739-752, 2013.

Ghazavi, M., J. Nazari Afshar, "Bearing Capacity of Geosynthetic Encased Stone Columns", *Geotextiles and Geomembranes*, Vol. 38, pp. 26-36, 2013.

Gniel, J., A. Bouazza, "Improvement of Soft Soils Using Geogrid Encased Stone Columns", *Geotext Geomembr*, Vol. 27, No. 3, pp. 167-175, 2009.

Greenwood, D.A., "Mechanical Improvement of Soils below Ground Surface", *Ground Engineering*, Vol. 1, pp 11-22, 1970.

Greenwood, D.A., "Vibroflotation Rationale for Design and Practice, Methods of Treatment of Unstable Ground", *Newness-Buttersworth*, Vol. 1, pp 189-209, 1975.

Gu, M., M. Zhao, L. Zhang, J. Han, "Effects of Geogrid Encasement on Lateral and Vertical Deformations of Stone Columns in Model Tests", *Geosynthetics International*, Vol. 23, pp. 100-112, 2016.

Guoxing, C., C. Su, Z. Xi, D. Xiuli, Q.I. Chengzhi, W. Zhihua, "Shaking-Table Tests and Numerical Simulations on a Subway Structure in Soft Soil", *Soil Dynamics and Earthquake Engineering*, Vol. 76, pp. 13-28, 2015.

Han, J., S. Ye, "Field Tests of Soft Clay Stabilized by Stone Columns in Coastal Areas of China, 4th International Deep Foundations Institute Conference", *The Netherlands 1*, Vol. 1, pp. 243-248, 1991.

Hong, Y.-S., C.-S. Wu, Y.-S., Yu, "Model Tests on Geotextile-Encased Granular Columns Under 1-g and Undrained Conditions", *Geotextiles and Geomembranes*, Vol. 44, pp. 13-27, 2016.

Hughes, J.M.O., N.J. Withers, "Reinforcing of Soft Cohesive Soils with Stone Columns", *Ground Engineering*, Vol. 7, No. 3, pp. 42-49, 1974.

Hughes, J.M.O., N.J. Withers, D.A. Greenwood, "A Field Trial of the Reinforcing Effect of a Stone Column in Soil", *Geotechnique*, Vol. 25, No. 1, pp. 31-44, 1975.

Hushmand, B., R.F. Scott, C.B. Crouse, "Centrifuge Liquefaction Tests in a Laminar Box", *Geotechnique*, Vol. 38, pp. 253-262, 1988.

Juran, I., A. Guermazi, "Settlement Response of Soft Soils Reinforced by Compacted Sand Columns", *American Society Of Civil Engineering*, Vol. 114, No. 8, pp.

930-943, 1988.

Kilic, I.E., *Seismic Behavior of Geosynthetic Reinforced Retaining Structures with Cohesive Backfills*, Ph.D. Thesis, Bogazici University, Turkey, 2014.

Kim, B.I., S.H. Lee, "Comparison of Bearing Capacity Characteristics of Sand and Gravel Compaction Pile Treated Ground", *Journal Civil Engineering*, Vol. 9, No. 3, 197-203, 2005.

Latha, G.M., P. Santhanakumar, "Seismic Response of Reduced-Scale Modular Block and Rigid Faced Reinforced Walls through Shaking Table Tests", *Geotextiles and Geomembranes*, Vol. 43, pp. 307-316, 2015.

Lo, S.R., R. Zhang, J. Mak, "Geosynthetic-Encased Stone Columns in Soft Clay A Numerical Study", *Geotext Geomember*, Vol. 28, pp. 292-302, 2010.

Lombardi, D., S. Bhattacharya, F. Scarpa, M. Bianchi, "Dynamic Response of a Geotechnical Rigid Model Container with Absorbing Boundaries", *Soil Dynamics and Earthquake Engineering*, Vol. 69, pp. 46-56, 2015.

Lillis, C., A.J. Lutenegger, M. Adams, "Compression and Uplift of Rammed Aggregate Piers in Clay", *American Society of Civil Engineering*, Vol. 1, 124, 2004.

Ling, H., D. Leshchinsky, Y. Mohri, J.-P Wang, "Earthquake Response of Reinforced Segmental Retaining Walls Backfilled with Substantial Percentage of Fines", *Journal of Geotechnical and Geoenvironmental Engineering*, Vol. 138, pp. 934-944, 2012.

Madabhushi, S.P.G., G. Butler, A.N, Schofield, "Design of an Equivalent Shear Beam Container for use on the US Army", *Centrifuge*, Balkema, Rotterdam, 1998.

Malarvizhi S.N., K. Ilamparuthi, "Load Versus Settlement of Clay Bed Stabilized with Stone and Reinforced Stone Columns", *Proceedings of Geo-Asia*, Vol. 1, pp. 322-

329, 2004.

Malarvizhi, S.N., K. Ilamparuthi, "Comparative Study on the Behavior of Encased Stone Column and Conventional Stone Column", *Soil and Foundations*, Vol. 47, pp. 873-885, 2007.

McKelvey, D., *Performance of Vibro Stone Columnreinforced Foundations in Deep Soft Ground*, Ph.D. Thesis, Queen's, University of Belfast, 2002.

McKelvey, D., V. Sivakumar, A. Bell, J. Graham, "Modeling Vibrated Stone Columns in Soft Clay, *Proceedings of the Institute of Civil Engineers Geotechnical Engineering*, Vol. 157, No. 3, pp. 137-149, 2004.

Miranda, M., A. Da Costa, J. Castro, C. Sagaseta, "Influence of Geotextile Encasement on the Behaviour of Stone Columns Laboratory Study", *Geotextiles and Geomembranes*, Vol. 45, pp. 14-22, 2017.

Mitchell, J.K., "Soil Improvement-State-of-the-Art Report. In: Proceedings of the Tenth International Conference on Soil Mechanics and Foundation Engineering, Stockholm", *Geotextiles and Geomembranes*, Vol. 44, pp. 497-512, 1981.

Muir Wood, D., W. Hu, D.F.T. Nash, "Group Effects in Stone Column Foundations Model Tests", *Geotechnique*, Vol. 50, No. 6, pp. 689-698, 2000.

Murugesan, S., K. Rajagopal, "Model Tests on Geosynthetic-Encased Stone Columns", *Geosynthetics International*, Vol. 14, pp. 346-354, 2007.

Murugesan, S., K. Rajagopal, "Performance of Encased Stone Columns and Design Guidelines for Construction on Soft Clay Soils", In *Proceedings of the 4th Asian Regional Conference on Geosynthetics*, Vol. 1, pp. 729-734, 2008.

Murugesan, S., K. Rajagopal, "Shear Load Tests on Stone Columns With and Without Geosynthetic Encasement", *Geotechnical Testing Journal*, Vol. 32, pp. 76-85,

2009.

Murugesan, S., K. Rajagopal, "Studies on the Behavior of Single and Group of Geosynthetic Encased Stone Columns", *Journal Geotech Geoenviron Engineering American Society of Civil Engineering*, Vol. 136, No. 1, pp. 129-139, 2010.

Najjar, S.S., S. Sadek, T. Maakaroun, "Effect of Sand Columns on the Undrained Load Response of Soft Clays", *Journal Geotech Geoenviron Engineering American Society of Civil Engineering*, Vol. 136, No. 9, pp. 1263-1277, 2010.

Najjar, S.S., "A State-of-the-Art Review of Stone/Sand-Column Reinforced Clay Systems", *Geotechnical and Geological Engineering*, Vol. 31, pp. 355-386, 2013.

Narasimha Rao, S., Y.N.S. Prasad, V. Hanumanta Rao, "Use of Stone Columns in Soft Marine Clays", *in Proceedings of the 45th Canadian Geotechnical Conference*, Vol. 1, pp. 1-9, 1992.

Ng, C.W.W., X.S. Li, P.A. Van Laak, D.Y.J. Hou, "And Centrifuge Modelling of Loose Fill Embankment Subjected to Unit-Axial And Bi-Axial Earthquakes", *Soil Dynamic Earthquake Engineering*, Vol. 24, pp 305-318, 2004.

Norton, H., *Investigation into Pile Foundations in Seismically Liquefiable Soils*, M.S. Thesis, University of Oxford, 2008.

Panah, K.A., M. Yazdi, A. Ghalandarzadeh, "Shaking Table Tests on Soil Retaining Walls Reinforced By Polymeric Strips", *Geotextiles and Geomembranes*, Vol. 43, pp. 148-161, 2015.

Priebe, H.J., "The Design of Vibro Replacement", *Ground Engineering*, Vol. 28, No. 10, pp. 31-37, 1995.

Pulko, B., B. Majes, J. Logar, "Geosynthetic-Encased Stone Columns Analytical Calculation Model", *Geotext Geomembr*, Vol. 29, pp. 29-39, 2011.

Raithel, M., H.G. Kempfert, "Calculation Models for Dam Foundations with Geotextile Coated Sand Columns", *In Proceedings of the International Conference on Geotechnical and Geological Engineering*, Geoengg 2000.

Rajagopal, K., N.R. Krishnaswamy, G. Madhavi Latha, "Behavior of Sand Confined With Single and Multiple Geocells", *Geotext Geomembr*, Vol. 17, pp. 171-184, 1999.

Shahu, J.T., Y.R. Reddy, "Clayey Soil Reinforced with Stone Column Group: Model Tests and Analyses", *Journal Geotech Geoenviron Engineering American Society of Civil Engineering*, Vol. 137, No. 12, pp. 1265-1274, 2011.

Sivakumar, V., D. McKelvey, J. Graham, D. Hughes, "Triaxial Tests on Model Sand Columns in Clay", *Can Geotech Journal*, Vol. 41, pp. 299-312, 2004.

Sivakumar, V., D.K.N.M. Jeludine, A. Bell, D.T. Glyn, P. Mackinnon, "The Pressure Distribution Along Stone Columns in Soft Clay Under Consolidation and Foundation Loading", *Geotechnique*, Vol. 61, No. 7, pp. 613-620, 2011.

Stuedlein, A.W., R.D. Holtz, "Analysis of Footing Load Tests of Aggregate Piers in Clay", *Journal Geotech Geoenviron Engineering American Society of Civil Engineering*, 2012.

Talesnick, M., "Measuring Soil Pressure within A Soil Mass", *Canadian Geotechnical Journal*, Vol. 50, pp. 716-722, 2013.

Travasarou, T., J.D. Bray, and N.A. Abrahamson, "Empirical Attenuation Relationship for Arias Intensity", *Submitted to Earthquake Engineering and Structural Dynamics*, April, 2002.

Ueng, T.S., "Shaking Table Tests for Studies of Liquefaction and Soil-Pile Interaction", *Geotechnical Engineering Journal of the SEAGS*, Vol. 41, No. 1, pp. 1-10, 2010.

Wang, L., G. Chen, S. Chen, "Experimental Study on Seismic Response of Geogrid Reinforced Rigid Retaining Walls with Saturated Backfill Sand", *Geotextiles and Geomembranes*, Vol. 43, pp. 35-45, 2015.

Wang, J., G. Yang, H. Liu, S. Shrawan Nimbalkar, X. Tang, Y. Xiao, "Seismic Response of Concrete-Rockfill Combination Dam Using Large-Scale Shaking Table Tests", *Soil Dynamics and Earthquake Engineering*, Vol. 99, pp. 9-19, 2017.

Watts, K.S., D. Johnson, L.A. Wood, A. Saadi, "Instrumental Trial of Vibrio Ground Treatment Supporting Strip Foundations in a Variable Fill", *Geotechnique*, Vol. 50, No. 6, pp. 699-709, 2000.

White, D.J., H.T. Pham, K.K. Hoevelkamp, "Support Mechanisms of Rammed Aggregate Piers. I-Experimental Results", *Journal Geotech Geoenviron Engineering*, Vol. 133, No. 12, pp. 1503-1511, 2007.

Whitman, R.V., P.C. Lambe, "Effect of Boundary Conditions upon Centrifuge Experiments Using Ground Motion Simulation", *Geotech Test Journal*, Vol. 9, No. 2, pp. 61-71, 1986.

Wu, C.S., Y.S. Hong, "Laboratory Tests on Geosyntheticencapsulated Sand Columns", *Geotext Geomembr*, Vol. 27, pp. 107-120, 2009.

Zeng, X., A.N. Schofield, "Design and Performance of an Equivalent-Shear-Beam Container for Earthquake Centrifuge Modelling", *Geotechnique*, Vol. 46, No. 1, pp 83-102, 1996.

Zhang, L., S.H. Goh, J. Yi, "Centrifuge Study of the Seismic Response of Pile?Raft Systems Embedded in Soft Clay", *Geotechnique*, Vol. 67, pp. 479-490, 2016.